UNIVERSITA' DEGLI STUDI DI BARI

DIPARTIMENTO INTERATENEO DI FISICA

Tesi di Dottorato in Fisica

Measurements of Neutron Capture Cross-sections at the n_TOF facility at CERN

Stefano Marrone

Anno Accademico 2001/2002
XV Ciclo

Index

Introduction

The knowledge of neutron cross-sections has always been, since the discovery of the neutron in 1930, of extreme interest for many fields of fundamental and applied Nuclear Physics. In basic Nuclear Physics, the measurement and evaluation of neutron cross-sections allow to investigate important properties concerning the structure of nuclei such as nuclear levels, spin, parity, decay scheme and branching ratios. Neutron-induced reactions are also useful for studying the main characteristics of the fundamental interactions (weak, strong, electromagnetic) and provide accurate information on their coupling constants, range, potential, etc.

Together with basic Nuclear Physics, other fields of fundamental Physics rely on the knowledge of neutron-induced processes. For instance, capture cross-sections are of extreme importance in Nuclear Astrophysics, in particular for the comprehension of Stellar Nucleosynthesis of heavy elements (that is above Fe), which proceeds essentially through a series of neutron capture reactions followed by beta decay. Theoretical models used for understanding the observed abundance of heavy elements in the Universe rely on the capture cross-sections for detailed calculations of capture reaction rates inside the stars, in different conditions of temperature and neutron density. While the main features of Stellar Nucleosynthesis are well understood, thanks to the efforts in that field during the past 40 years, some aspects related mainly to radioactive species with long half life are still unexplored due to the lack of experimental data. This is true, in particular, for the *branching isotopes* (discussed in chapter one), which would allow to extract important information on the process of neutron production in red giant, and at the same time, provide information on the temperature and density of those stars.

While neutron cross-sections data are important in many fields of basic Science, they play an even more essential role in several applications. As an example, the development of the nuclear technology for energy production would not have been possible without the knowledge of capture and fission-induced reaction cross-sections and any new developments in the field requires a previous detailed investigation of the involved neutron processes. Currently, neutron cross-section data have become fundamental in many other activities, from Nuclear Medicine to Material Science. In Radioprotection, Monte Carlo

codes based on existing databases are used, for example, to design appropriate shielding for accelerators built for Nuclear Research or for Medical and Industrial applications. In Nuclear Medicine, the investigation of new methods for diagnostic and therapy, based on neutrons or charged particle beams (Adrotherapy), requires extensive simulations of the neutron interaction in tissues, as well as in the materials surrounding the patient. Finally, the use of neutron beams is becoming more and more widespread in Material Science or for applications of nuclear techniques to a variety of goals, such as mines and drugs detection, Forensic studies and so on.

A large experimental and theoretical activity has been carried out over the years on the measurement and evaluation of the neutron cross-sections. The efforts have led to a number of databases that contain a compilation of the neutron cross-section for a large fraction of the isotopes of the Periodic Table of elements. Among the different databases, the most commonly used are ENDF/B-VI (Evaluated Nuclear Data File) sponsored by DOE (Department of Energy, USA), the European database JEFF maintained by the Nuclear Energy Agency and Organization for Economic Cooperation and Development (NEA/OECD), the Japanese database JENDL, the Russian BRONDE, etc. Although several discrepancies exist between the different databases for some isotopes, the available information were considered up to few years ago adequate for different applications.

In recent years, however, clear limitations of the existing databases have renewed the interest in neutron cross-sections data. The main reason for additional and accurate data on neutron cross-sections resides in new development in the field of Emerging Nuclear Technologies that have recently been proposed. In particular, the design of innovative systems for energy production and nuclear waste incineration, such as Accelerator Driven Systems (ADS), requires cross-section data on many isotopes most of which radioactive. At present, a large fraction of needed data is completely missing or largely incomplete. Even when data exist, in many cases large experimental uncertainties make the evaluated cross-sections unreliable. This is demonstrated by the large discrepancy in the tabulated cross-sections between different databases that can be observed for some of the isotopes involved in the new developments. The need for nuclear data is demonstrated by the “High priority nuclear data request list”, from the NEA/OECD, which contains up to 200 requests of data relevant to Fission, Fusion, Dosimetry, etc.

Following the needs for new and accurate nuclear data, many research programs have been recently promoted in Europe, in USA and in Japan. The goal of these programs is to stimulate experimental and theoretical works on nuclear data, taking advantage also of the

recent development of innovative facilities, new detectors and analysis techniques, new dissemination tools, as well as other improvements necessary for producing and making available new data for basic and applied science. In Europe, the Fifth Framework Program of the European Commission has sponsored several projects in Nuclear Physic, devoted to new developments in emerging nuclear technologies.

One of the most interesting and innovative projects currently under way, is n_TOF (neutron Time-of-Flight facility). Recently started at CERN, under the support of the Commission of European Communities within the V Framework Program for Research, the n_TOF project is devoted to the measurement and evaluation of neutron cross-section, in a wide energy range and with high energy resolution, related to ADS and Astrophysics. The project is made possible by the new neutron facility, recently set-in-operation at CERN, Geneva, in which a neutron beam with high instantaneous flux in a wide energy range, high resolution and low background is produced by spallation of 20 GeV/c protons from the ProtoSyncrotron accelerator. The innovative features of the facility allow to collect high quality data on a variety of isotopes, for which data are highly needed.

The facility was completed in April 2001. Immediately after completion, a series of measurements have allowed to characterize the neutron beam, in term of flux, resolution, background, etc… The first measurement campaign has then started with the measurement of some capture cross-sections.

The present thesis regards the first measurements of neutron cross-sections performed at the n_TOF facility at CERN. In Chapter I, the scientific motivation for the experimental program at n_TOF is presented in some detail. The production of neutron beams and the innovative features of the facility, as compared to existing neutron beams, are discussed in Chapter II. Chapter III is devoted to the description of the experimental apparatus and analysis technique used for the determination of the neutron cross-sections, in particular for capture reactions. The apparatus consists mainly in a Low-mass Flux Monitoring system, based on Silicon detectors, developed in order to determine and monitor the neutron flux with minimal perturbation of the beam and minimal induced background. For capture reactions, deuterated-benzene liquid scintillator detectors with low sensitivity to neutrons (C_6D_6) are used for γ-ray detection. Chapter III contains also a detailed description of the Pulse Height Weighting function technique, necessary to correct the measured data for the detector efficiency, in a way independent on the detailed de-excitation cascade. A brief description of the Data Acquisition System, based on Flash ADC with high sampling rate

will be given, together with the procedure used for extracting the main information from the signals.

In Chapter IV, the experimental results on the neutron beam characterization are presented; these results are extracted by the analysis of the Silicon Flux Monitor and of the C_6D_6 data. The first measurements evidenced a background about two orders of magnitude larger than tolerable, making it impossible to pursue the foreseen experimental program. The extensive campaign of measurements undertaken in order to solve the background problem is briefly described. Finally in Chapter V, the first, preliminary results on the capture cross-section for ^{151}Sm, an isotope of interest both for the ADS and for Astrophysics, are shown and discussed. In particular the extracted cross-sections in the resolved and unresolved resonance region are presented. The resonance parameters have been determined with the code SAMMY. A description of this code, which is one of the most commonly used programs for fitting the experimental data, is given in Appendix II.

Chapter I

1.1 Overview

The study of neutrons and of neutron-induced reactions has always been of great importance in many fields, from Elementary Particle Physics, to Nuclear Physics, to quantum mechanics and, more recently, for the development of Nuclear Technologies.

In fundamental Nuclear Physics, the absence of the Coulomb force makes neutrons a powerful tool for investigating the properties of the strong interaction, since it simplifies in many cases the theoretical description and the data analysis of scattering experiments. The study of neutron emission from compound nuclei formed in light and heavy ion reactions provides valuable information on the de-excitation processes of excited nuclear matter. Some aspects of the weak interaction can be addressed by studying the neutron β-decay, while the electromagnetic interaction via the anomalous magnetic moment is of great importance for the use of the scattering technique with thermal and cold neutrons in condensed matter physics. Neutron cross-sections are sensitive to the charge distributions of the neutrons, thus electromagnetic structure constants of such particles, i.e. charge radius and electric polarizability, can be determined by studying neutron reactions.

Neutron studies play an important role also in other fields of Physics. In Nuclear Astrophysics, neutron capture processes are responsible for the production of elements heavier than Fe. Since the theory was first proposed by BBFH (Burbridge, Burbridge, Fowler and Hoyle) [1], the main features of Stellar Nucleosynthesis have been understood, thanks to the study of capture process in laboratories. By combining the knowledge of elemental abundance in the universe, typically obtained through spectroscopic analysis and studies of meteorites, with experimental data and theoretical models on neutron capture reactions, a wealth of information on the evolution of stars and galaxies has been obtained.

Finally, neutron reactions have always been, since the beginning, fundamental for the development of nuclear applications. In recent years, nuclear technologies have received more attentions, with many ideas on different problems, from the development of safer systems for energy production, to finding a solution for the final disposal of radioactive nuclear waste, to new means of diagnosis in medicine, to weapons and drug control.

The renewed interest in the study of neutron reactions has recently prompted the construction of an innovative neutron facility at CERN: n_TOF. Based on an idea of C. Rubbia [2], the new facility was proposed by a large international collaboration, made of 150 scientists with interests and competences in many different fields. The scientific program that has been proposed, taking advantage of the characteristics of the neutron beam, can be summarized in three main lines of research:

- Study of neutron cross-sections relevant to Nuclear Astrophysics;
- Study of neutron cross-sections relevant to energy production and to Nuclear Waste Transmutation (Accelerator Driven System);
- Study of neutrons reactions, as a probe for fundamental Nuclear Physics.

The present chapter intends to present an overview of the three main topics and their state of art, which have inspired the start of an experimental program at the innovative n_TOF facility.

1.2 Nuclear reactions for Astrophysics

The evolution of the Universe, according to the actual Standard Model of Big Bang cosmology, can be divided into few main stages: Big Bang, primordial nucleosynthesis and atomic formation, galactic condensation, stellar and explosive nucleosynthesis. This Model includes an overall framework based on the General theory of Relativity and on nuclear and particle properties [3]. The nucleosynthesis chain began with the formation of the deuterium (the deuterium binding energy is 10^9 K), when the temperature of the Universe had decreased about 200 seconds after the Big Bang. In this condition, nuclear reactions lead to the production of light elements as ^{2}H, ^{3}H, ^{4}He and ^{7}Li. Any stellar model must reproduce, as a first step, the abundance of element in agreement with observations, the primary ones being the relative amounts of these light isotopes produced during the earliest epoch of element formation. The observed abundances impose severe constraints on the fundamental process that occurred during the formation epoch.

The hot mix of H, He and Li continued expanding and cooling. After about 3×10^5 years the atomic nuclei could combine with free electrons to form atoms but only after 30 million of years, at a temperature of 100 K, the force of the gravity began to take over and led to the formation of galaxies and stars. Most of the light elements up to Fe that we observe in nature were produced in massive stars (10 time the mass of the sun) and in the supernova explosions. Understanding the relative abundance of these elements and isotopes

has been a challenge over the last 60 years, with a continuous request to Nuclear Physics to provide the necessary nuclear data.

Understanding the formation of heavy elements in fusion reactions or following neutron captures in stellar interiors is a difficult task. Apart from the complicated nuclear processes involved, the thermodynamics and other aspects of the mechanism of Stellar Nucleosynthesis are not yet completely understood. The experimental evidence consists of astronomical observations with ground-based telescope or with γ-rays, *X*-rays, satellite-based particle spectrometers and microanalysis studies of meteorites. The synthesis of most heavy elements with $A>60$ has been attributed primarily to neutron-capture processes, which occur in different stellar sites. Promising candidates range from the interior of red-giant stars to the low density, high entropy bubble, just inside of an expanding core-collapse supernova shock wave. Any improvement in the understanding of these processes and of the astrophysical sites where they occur requires advances in laboratory measurements of neutron cross-sections [4]. It is important to notice here that the goal of the models of Stellar Nucleosynthesis is to understand not only the detailed way in which heavy elements are synthesized but also to obtain information on the conditions of the astrophysical sites where the synthesis occur.

Neutron reactions are responsible for the formation of all elements heavier than iron. In astrophysical scenarios, heavy elements can only be produced by neutron capture reactions and subsequent β-decays. Fusion of charged particles no longer contributes in this range since the Coulomb barriers are becoming too high and binding energies per nucleon are decreasing beyond $A \approx 60$. In order to explain the observed abundance of isotopes between iron and the actinides, essentially three processes must be invoked: s-process, r-process and p-process. A schematic view of the different processes is shown in Figure 1.1. In the slow neutron capture process (s-process), neutron captures occur at a much slower rate than the β-decay of the isotopes produced (the time-scale for capture ranging from several months to 10^5 years). As a consequence, the isotopes involved in the processes stay close to the line of β-stability.

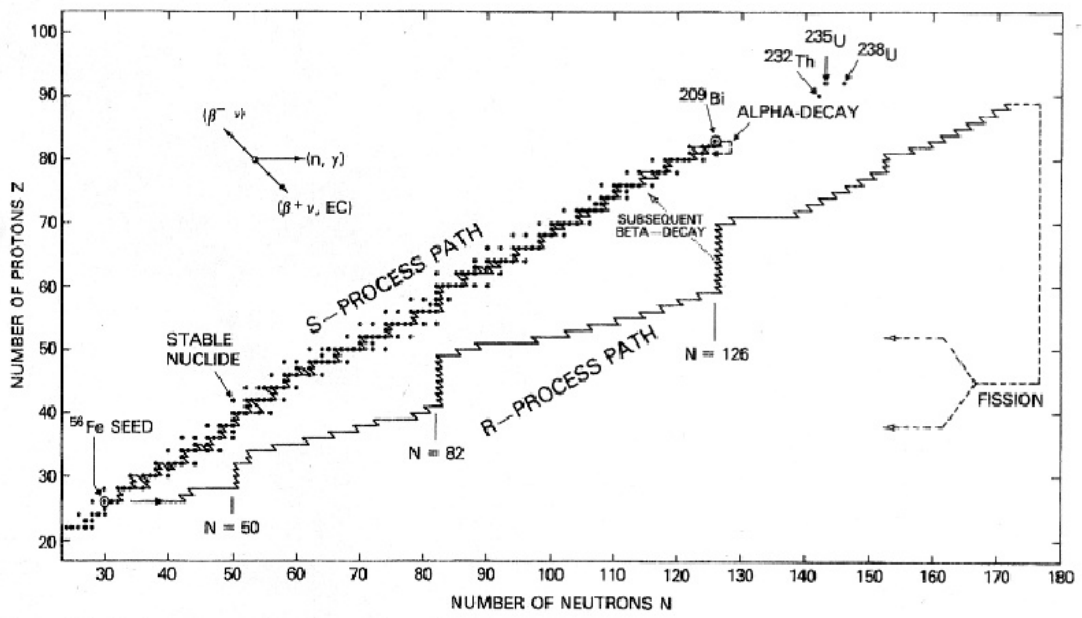

Figure 1.1: Neutron capture paths, for s- and r-process in the *N-Z* plane.

Under explosive conditions in neutron-rich environments, neutron capture can become much faster relative to the β-decay of the involved isotopes, with a time scale of 0.01-10 sec. In this case to so called r-process (for rapid capture) occurs. Since many successive captures may occur before a β-decay, isotopes far away from the stability line are produced. Clearly, a different abundance pattern results in this case. The r-process is usually attributed to nucleosynthesis in the high entropy bubble behind the shock front in type II supernova explosions.

Recently, laboratory studies have concentrated on the s-process, which operates in or near the valley of the β-stability. This process, associated with stellar helium burning, is characterized by relatively low neutron densities. This implies neutron capture times much longer than typical β-decay half-lives. Therefore the s-process reaction path follows the stability valley as indicated by the solid line in the *N-Z* plane of Figure 1.1. The abundance of isotopes produced in s-process, also indicated as s-abundance, is essentially determined by the relative capture or (n,γ) cross-section, averaged over the stellar neutron spectrum according to the relation:

$$\langle\sigma\rangle_{kT} = \frac{2}{\sqrt{\pi}} \frac{\int_0^\infty \sigma(E_n)\cdot E_n \cdot \exp(-E_n/kT)dE_n}{\int_0^\infty E_n \cdot \exp(-E_n/kT)dE_n}.$$

As an example, isotopes with small cross-sections are built up to large abundances. This holds in particular for nuclei with closed neutron shells (N=50, 82 and 126) giving rise to the sharp s-process maxima in the abundance distribution around A=88, 140 and 208, see Figure 1.2.

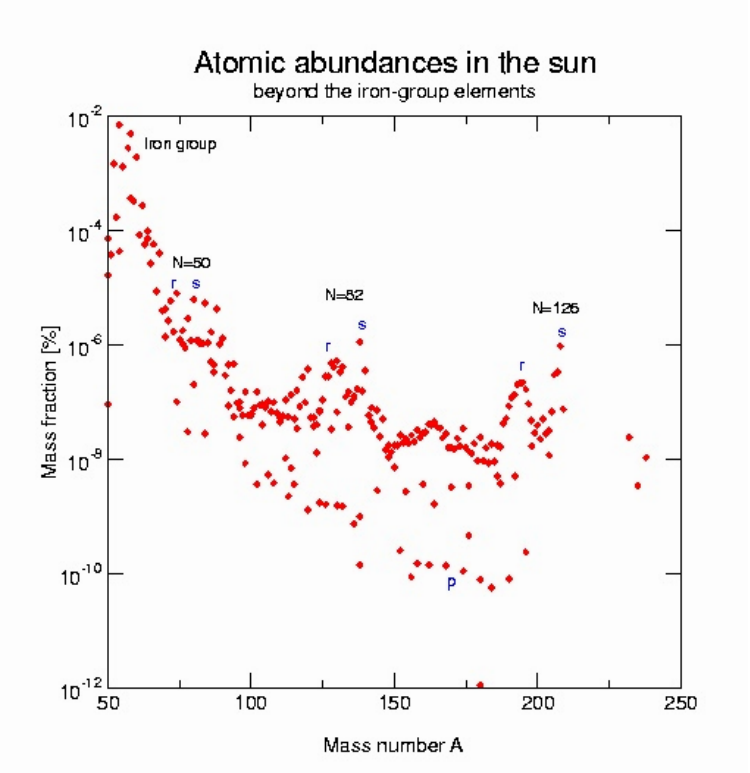

Figure 1.2: Atomic abundances in the sun.

The s-process accounts for the production of approximately half of the elemental abundance distribution between Fe and Bi (Figure 1.3), with the abundance essentially determined by an almost linear relation to the stellar (n,γ) cross-sections. Clearly, the accuracy of (n,γ) cross sections data for the s-process has an immediate impact on the predicted abundance. The quantitative interpretation of the s-abundance represents important and sensitive tests for the model of stellar He-burning.

1.2.1 Need of capture cross-sections related to s-process

In order to understand the Stellar Nucleosynthesis of heavy elements, differential capture cross-sections $\sigma(E_n)$ are needed. In this way, the stellar average cross-sections can be calculated and the reaction rates estimated. Since many years, measurements of capture cross-sections for Astrophysics have been carried out in different laboratories around the world. Nevertheless, new and more reliable data are still needed.

Among the different classes of isotopes, the Nuclear Astrophysics community has concentrated its interest on those produced only in the s-process (the so called “s-only

isotopes"), because they are used to precisely normalize the s-process contributions to all elements, and because the ratios of this isotopic abundance can be compared to extremely precise measurements from meteorites [5]. However, in some cases experimental data on such isotopes are still completely missing, i.e. for isotopes of Ge, Se, Xe and Pt. The availability of new, high precision abundance measurements, primarily in meteorites, is a strong motivation for new, precise measurements of neutron capture cross-sections.

Another class of interesting nuclei is represented by the so-called "branch point isotopes", characterized by comparable lifetime for neutron capture and β-decay. The s-process reaction rate, in this case, depends strongly on the astrophysical stellar properties, mainly the temperature and neutron density. Therefore, branch-point isotopes can be used as a very sensitive tool for probing the environmental conditions in some stars [6].

Given the range of temperatures from 100 to 300×10^6 K, which are characteristics for He-burning scenarios, differential neutron data are needed between 0.3 and 300 keV, mostly for stable nuclei but also for a significant number of radioactive isotopes with half-lives comparable to the typical neutron capture times of few months. The s-process branching isotopes include the unstable ^{85}Kr, $^{134,\ 135}$Cs, ^{147}Nd, $^{147,\ 148}$Pm and ^{151}Sm. These cases are important, because the competition between neutron capture and β-decay causes the reaction path to split, resulting in very particular abundance patterns which are reflecting the stellar neutron density and temperature. Therefore, they represent sensitive tests of the yet uncertain stellar models for the He-burning stages of evolution. A satisfactory database for the s-process studies should, therefore, contain experimental information over a sufficiently wide energy range and with uncertainties of about 5%.

At present, this condition is far from being accomplished. In fact, the experimental determination of capture cross-sections for radioactive nuclei is made difficult by the large background associated with the natural radioactivity of the isotope. In typical detection systems, in fact, γ-rays produced by radioactive decay of the sample cannot be easily distinguished from the γ-rays emitted in a capture reaction, thus resulting in large uncertainties affecting the measured capture cross-sections. A substantial improvement of the signal-to-background ratio can only be achieved by using a neutron beam with much higher flux than available up to now. As will be shown in a later chapter, the n_TOF facility at CERN is characterized by a very high instantaneous neutron flux, up to three orders of magnitude larger than in other existing facilities. For this reason, it results of extreme interest in the measurements of Astrophysics-related capture cross-sections.

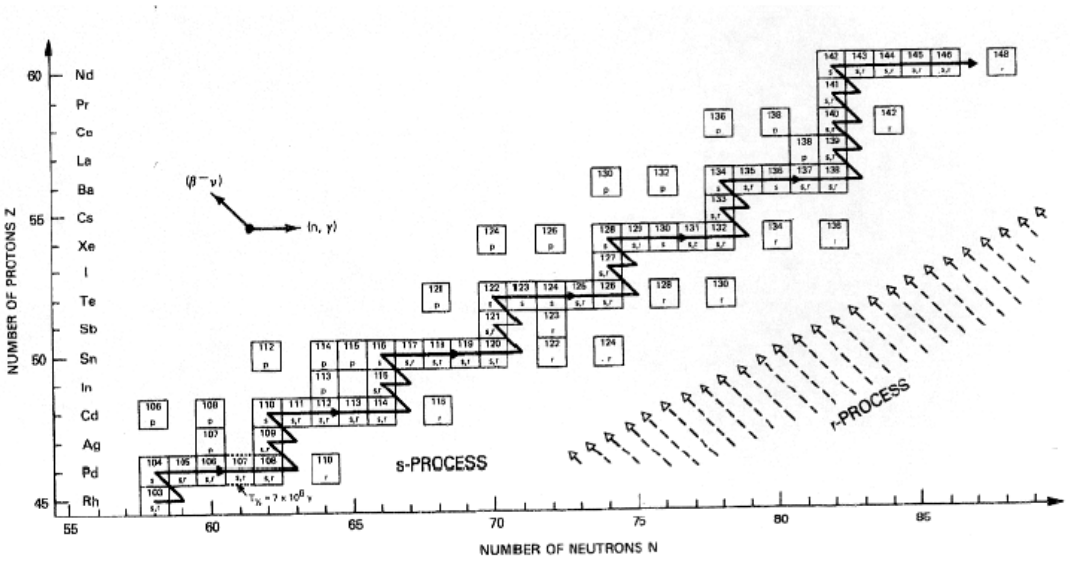

Figure 1.3: A section of the chart of nuclides and the s-process path through the elements in this mass region.

1.2.2 r-process

Neutron capture data are also important for explosive r- and p-process scenarios, particularly during the freeze-out phase, where they lead to significant modifications of the primary reaction yields. These scenarios, occurring far from the stability, imply reactions on rather short-lived isotopes, which are much more difficult to study experimentally [7]. Therefore, the modeling of r-process nucleosynthesis relies on nuclear models for the estimate of neutron binding energies and β-decay lifetimes for thousands of nuclei. However, when predicting nuclear properties away from the stability valley, nuclear models are pushed to their limits and may give unreliable results. In fact, recent systematic analysis of r-process abundance has pointed out to some inconsistencies in nuclear models. It should also be pointed out that r-process abundance is estimated by subtracting the calculated s-process abundance from the measured one and, for this reason, is often referred to as “residual abundance”. Therefore it relies on an accurate knowledge of the s-process abundance, which as explained before relies in turn on the accurate determination of capture cross-sections.

Also fission enters into the r-process path in several ways. It can terminate the r-process path at Z=92, it can alter the resulting abundances of the long-lived heavy isotopes ^{232}Th, $^{235\text{-}238}$U and ^{244}Pu, used to determine the duration of nucleosynthesis in our galaxy and the galactic age as well as the age of the Universe. Finally, in environments with a long

duration of neutron exposure, fission cycling can determine the total abundance of heavy nuclei.

The only available experimental tests for theoretical predictions of β-delayed fission come from the analysis of abundance in the products of nuclear explosions. Therefore, the prediction of fission barrier properties (height and curvature) is essential for the astrophysical applications. Neutron-induced fission can support calculations by providing test cases for theoretical barrier models and resulting predicted cross-sections.

At present, very scarce data exist on radioactive nuclei that would be valuable for studies of r-process. As for the s-process case, the subject would greatly benefit from the n_TOF neutron beam, recently become operational at CERN.

1.2.3 p-process

The requests for neutron capture data for the p-process are based on arguments similar to those made before with respect to the r-process [8]. Experimental time-of-flight data would in fact clearly improve the description of freeze-out effects in the p-process where neutrons are liberated by (γ,n) reactions during the explosive burning of the Ne/O shell. Furthermore (n,γ) cross-sections of proton rich nuclei would be most useful in determining the inverse rates by detailed balance. Feasible cases at spallation neutron sources include ^{53}Mn, ^{55}Fe, ^{57}Co, ^{59}Ni, ^{97}Tc, ^{109}Cd, ^{143}Pm, ^{145}Sm, ^{146}Sm, ^{148}Gd, ^{150}Gd, ^{195}Au and ^{202}Pb. Data are needed on many stable targets, which can also improve the databases for p-process studies. This group consists of the rare stable nuclei, where only small samples of isotopically enriched materials are available. Data on as many nuclei as possible, between ^{74}Se and ^{196}Hg, most of which have not yet been studied at astrophysical relevant energies, would be very valuable.

1.3 ADS and waste transmutation

The safe and sustainable energy production is one of the most important problems that the humanity is facing since a few decades. In recent years, the problem of energy supply has become more pressing, due to a number of consequences of the present energy politics. Growing concerns about the environmental impact of fossil fuel burning, in particular the greenhouse effect, together with the limited availability of the fossil fuel, lead to an increasing consideration of alternative means of energy production. Renewable sources, such as eolic and solar energy, can still account for only a small fraction of the energy needs. On the other hand, nuclear fusion is still at the research stage and realistically few

decades may still be necessary to arrive to an industrial development of fusion reactors. Therefore, at present the only valid alternative to fossil fuel burning for large-scale energy production is still represented by nuclear fission [9]. However, the exploitation of nuclear energy poses severe problems. Among them, the most important ones are the safety issues associated with the operation of nuclear power plants and the problem of the disposal of radioactive nuclear waste.

The need to solve the safety issues have led in recent years to the consideration of a variety of advanced, alternative strategies for the nuclear fuel cycle and for waste disposal. Different possibilities are currently being considered for a more efficient use of the nuclear energy: the extensions of the life span, and the upgrade of presently operating reactors, the increase of the fuel burn-up, the plutonium recycling, etc… The most promising solution, however, is the development of the so-called Accelerator Driven Systems (ADS) for energy production and nuclear waste incineration through the transmutation of long-lived radioactive isotopes into stable or short-lived species, typically by means of neutron-induced reactions.

ADS is a sub-critical reactor in which extra neutrons, necessary to sustain the fission chain and/or to incinerate the nuclear waste are supplied by means of an accelerator. In most designs, the needed neutrons are generated by spallation of high-energy protons on Pb, often used also as coolant. The inherent safety of such a system is apparent. The chain reaction, in fact, cannot go out of control and in case of accident, turning off the accelerator ensures the stop of the chain reaction. For nuclear waste incineration, the external source based on accelerator supplies neutrons necessary for the transmutation process. Long-lived fission fragments are transformed into stable or short-lived isotopes mainly through neutron capture reactions, while minor actinides can be incinerated via capture and neutron-induced fission. In ADS for energy production, only a fraction of the energy produced in the reactor is needed to operate the accelerator. In same cases, hybrid systems can at the same time ensure energy production and nuclear waste incineration.

Several designs of ADS are currently being investigating. For energy production, a convenient solution is the idea of the Energy Amplifier (EA), proposed by C. Rubbia [2] and based on the Th-fuel cycle. In this case, neutron produced by spallation of GeV protons would be used to sustain the following reaction: $^{232}\mathrm{Th}(n,\gamma)\,^{233}\mathrm{Pa} \rightarrow\ ^{233}\mathrm{U}+\beta$. Here, ^{232}Th represents the fertilizing isotope, while the main reaction is fission of ^{233}U. Due to the lower number of neutrons released in the fission process (compared to the standard fuel based on ^{235}U and ^{239}Pu), the reaction does not sustain itself and neutrons have to be

supplied from outside. The EA presents several advantages as the improvement of the safety, the reduction of the radiotoxicity, sustainability for long term etc.

Table 1.1: Higher Actinides Transmutation candidates, heavily produced in a PWR. The cross sections are from Mughabghab [11] comments refer to ENDF/B-VI.

Nuclide	Half-life	Thermal $\sigma_{n,\gamma}(b)$	Thermal $\sigma_{n,f}(b)$	ENDF/B-VI Quality
^{237}Np	2.1×10^{6} y	176 ± 3	$(21.5 \pm 2.4) \times10^{-6}$	Good
^{238}Np	2.1 d	300	2088 ± 30	Very weak
^{238}Pu	87.7 y	605	17.1±0.4	Very weak
^{242}Pu	3.7×10^{5} y	18.7± 0.7	-	Weak
^{244}Pu	8.1×10^{7} y	1.6± 0.3	-	Very weak
^{241}Am	433 y	620 ± 13	3.2 ± 0.1	Reasonable
^{242m}Am	141 y	2000	6328 ± 320	Very weak
^{243}Am	7370 y	75.1 ± 1.8	0.198 ± 0.004	Needs update
^{242}Cm	163 d	16 ± 5	< 5	Very weak
^{243}Cm	29.1 y	137.4± 9.6	633.3 ± 26.9	Very weak
^{244}Cm	18 y	15.2 ± 1.2	1.04 ± 0.20	Reasonable
^{245}Cm	8500 y	340 ± 20	2143± 58	Weak
^{246}Cm	470 y	1.22 ± 0.16	0.14 ± 0.05	Needs update
^{247}Cm	1.6×10^{7} y	57 ± 10	81.9 ± 4.4	Weak
^{248}Cm	3.5×10^{5} y	2.63 ± 0.26	0.37 ± 0.05	Needs update
^{232}Pa	1.3 d	700 ± 100	464 ± 95	None

Together with the EA, other projects are being developed in the field of ADS [10]. In all cases, detailed studies and safety assessments of ADS require the accurate knowledge of nuclear reaction data. Data are needed on the neutron production by the spallation process, on the neutron interaction with the spallation target, the coolant and structural material of the reactor core and, finally, on neutron-induced reactions for all isotopes involved in the fuel cycle. For the design of ADS for nuclear waste incineration, neutron capture cross-sections are needed for the main long-lived fission fragments, while capture and fission data are required for minor actinides. In general, neutron data are available in several data libraries (ENDF, JENDL, JEFF, BRONDE, etc…), containing a compilation of evaluated cross-sections for a large number of isotopes. Evaluations are based on different measurements and rely on theoretical models to complement the experimental results where data are lacking or inconsistent. Nevertheless, for many ADS-related isotopes, evaluated data are lacking or show substantial differences among them due, mainly, to the lack of reliable experimental data. In particular, while Thorium and Uranium-related cross sections are relatively well known, large discrepancies between databases exist for minor actinides such as: ^{232,233}Pa, ^{237,238}Np, ^{241,242,243}Am and ^{242,248}Cm. A list of evaluated data in

the ENDF/B-VI file for Pu and other important actinides is given in Table 1.1; it is possible to note as there is no evaluation for ^{232}Pa and the data concerning the ^{238}Np, ^{242}Am and ^{247}Cm are regarded as weak.

Table 1.2: Requested neutron capture cross-sections for stable and radioactive Fission Fragments (FF), Structural (SM) and Absorber (AM) Materials according to Ref. [12].

NEA Req. ID	*(Z,A)*	$\tau_{1/2}$ or Abundance%	Mass [mg]	*(n,γ)* events/d	Req. country & Priority	Use
4.A.8	Cr-50	4.3%			D	SM
4.A.10	Cr-52	83.8%			D	SM
4.A.12-16	Ni-nat				F1,Ja,U	SM
4.D.12	Se-79	6.5×10^5y	250	1.4×10^7	F2	FF
4.D.13	Zr-93	1.5×10^6 y	1000	7.3×10^6	F2/D	FF/SM
4.D.14	Mo-95	15.9%			F1,UK1	FF
4.D.1/15	Tc-99	2.1×10^6 y	31	4.3×10^6	F,UK	FF
4.D.2/16	Rh-103	100%			UK1,F2	FF
4.D.17	Pd-107	6.5×10^6 y	1000	4.6×10^7	F2	FF
4.C.2	Cd-nat				F1,UK2	AM
4.C.18	Sn-120	32.6%			WPEC	SM
4.C.19	Sn-122	4.6%			WPEC	SM
4.C.22	Sn-124				WPEC	Fusion
4.D.19	Sn-126	10^5 y	20	2.1×10^3	F2	FF
4.D.20	I-129	1.57×10^7 y	1000(IF)	1.6×10^7	F2	FF
4.D.3	Xe-131	21.2%			Ja	FF
4.D.4/21	Cs-133	100%			F1,UK1,Ru	FF
4.D.5/22	Cs-135	2.3×10^6 y	0.37	8.1×10^7	F2,Ja,Ru	FF
4.D.23	Nd-143	12.2%			F1,UK1	FF
4.D.24	Nd-145	8.3%			F2,UK1	FF
4.D.25	Sm-147	15%			F2,UK1	FF
4.D.26	Sm-149	13.8%			F1,UK1,Ja	FF
4.D.27	Sm-150	7.4%			F2	FF
4.D.28	Sm-151	90 y			F1,UK1,Ja	FF
4.D.29	Sm-152	26.7%			F1,UK1	FF
4.D.29	Eu-153	52.2%			F1,UK1	FF
4.C.5	Gd-nat				F1,UK1	AM
4.D.29	Gd-155	14.8%			F2,UK1	FF
4.C.6	Dy-nat	-			F2,UK1	AM

The design of ADS for nuclear waste incineration requires neutron data on several fission fragments as well. For most isotopes, the present information is insufficient or completely missing, while in many important cases, such as ^{90}Sr, ^{129}I and ^{135}Cs, order of magnitude discrepancies exist in the experimental data, especially in the thermal and epithermal regions. A list of the most important fission products considered as transmutation candidates is given in Table 1.2, together with a selected summary of the requests by the Nuclear Energy Agency and Organization for Economic Cooperation and Development (NEA/OECD). The current poor situation of the data and evaluated cross-sections is mostly due to the difficulties associated with the measurements of radioactive

samples. In this case, large uncertainties in the experimentally determined cross-sections are the direct consequence of the small signal-to-background ratio in data collected at older facilities and related to the natural radioactivity of the isotopes being investigated. This problem can be in large part overcome at the n_TOF facility, since the much higher instantaneous neutron flux at CERN results in a much better signal-to-background ratio for many of the required isotopes.

In addition to the fission fragments, interest is focused on the target, coolant and structural materials in ADS systems. All these materials are exposed to both the direct proton beams and the secondary neutrons. The target materials currently considered are Pb and Pb-Bi; while structural materials include C, Al, Si, P, Cr and liquid metal coolant Pb and Bi.

The cross-section data required in this case are for neutron total, elastic and inelastic scattering, double differential *(n,xn)* and *(n,xp)* reactions, capture or *(n,γ)* reactions, neutron induced fission *(n,f)* and *(n,xγ)* reactions. Double differential cross sections with heavy products, such as α-particles, would be also very useful for nuclear reaction modeling, while cross-sections on *(n,xp)* at 600-1000 MeV even with a moderate resolution are very interesting since data are scarce in this energy region.

1.4 Medical Applications

Nuclear data are not only needed for energy production and nuclear waste incineration, but also for a variety of other applications. A detailed list of data required for fission, fusion, dosimetry, radioprotection, Medicine and other industrial applications, is reported in the "The NEA High Priority Nuclear Data Request List", edited by the working Party on International Evaluation Co-operation of the OECD-NEA Nuclear Science Committee [12].

Accurate cross-section evaluations for neutron-induced reactions, including charged particle and γ-ray emission following the reaction, are required for radiation transport calculations related to radioprotection and radiotherapy. The type, accuracy and specificity of the needed information vary with the application. Similarly, the γ-rays produced by neutron interactions as well as energy and angular distributions for secondary neutrons are a major concern, for instance, as source of background in experimental nuclear physics.

Nuclear data are fundamental for improving the knowledge of the dose in radiological protection and radiation therapy when energetic neutrons are used. Dosimetry for fast neutrons (up to 14 MeV) is underdeveloped compared to the γ-ray one. There is an urgent

need for data on fast neutron interaction with different material (including human tissues) in order to comply with more strict regulations.

Neutron therapy and neutron transport calculations for radioprotection demand detailed microscopic charged particle production data for prediction of the absorbed dose by the patient. The same need exists for advanced proton therapy facilities where secondary neutrons are produced with energies as high as 250 MeV. Since data above few MeV are scarce, only nuclear model calculations can be used at present. Measurements of neutron interaction cross sections for different elements in a wide energy range would allow to perform more accurate simulations, needed for many applications.

Table 1.3 shows the principal needs for dosimetry and transport [13]. For C, N and O there is a scarcity of microscopic cross section information. Detailed data are needed for Si, Ca and N to support applications in medical electronics and for transport calculations due to their relevant presence in air and concrete. Since bones are almost always present in the radiated field in Neutron Radiotherapy, Ca data are also essential for this application.

Table 1.3: Required neutron cross-section information for dosimetry and radiotherapy. The level of accuracy of the data is indicated with 1 (the best accuracy), 2 (good accuracy) and 3 (approximate data are required).

Dosimetry					*TRANSPORT*		*IMPORTANCE*
Element	*P*	*α*	*d*	*recoil*	*Element*	*n,γ*	
H	*3*				*H*	*3*	*1*
C	*3*	*3*	*3*	*3*	*C*	*3*	*1*
O	*3*	*3*	*3*	*3*	*O*	*3*	*1*
Si	*3*	*3*	*3*	*3*	*Fe*	*3*	*2*
Ca	*3*	*3*	*(3)*	*3*	*W*	*3*	*2*
P	*3*	*3*			*Si*	*3*	*3*
K	*3*	*3*			*Ca*	*3*	*3*
N	*3*	*3*			*Pb*	*3*	*3*
					N	*3*	*3*

1.5 Basic Nuclear Physics

As mentioned in previous paragraphs, the innovative characteristics of the n_TOF facility may allow to collect valuable data for fundamental Nuclear Physics, in particular in neutron-nucleon, neutron-nucleus and neutron-electron interaction.

1.5.1 Neutron-Nucleon scattering

Some of the open questions in the field of neutron-nucleon interactions are: charge symmetry in nucleon-nucleon interaction, neutron-proton bremsstrahlung and meson production in neutron-proton scattering.

The charge asymmetry in nucleon-nucleon interaction is explained as a consequence of the differences in the masses and in the electric charge of *d* and *u* quarks [14]. This mass difference manifests itself in the difference of the neutron-neutron and proton-proton scattering lengths a_{nn} and a_{pp} in s-wave. The determination of a_{pp} is obtained in proton-proton experiments with all problems arising in the analysis due to the Coulomb force. The determination of a_{nn} instead requires more attention, because neutron-neutron scattering experiments are not feasible. One of the most practical way to solve this problem is a new consistent measurement of the neutron induced deuteron break-up over a wide energy range [15].

Great interest has drawn in the past the study of the nucleon-nucleon bremsstrahlung process especially concerning the off-shell behavior of the *NN* interaction. Today, the main interest is the observation of energetic photons produced in intermediate-energy heavy ion collisions in particular for disentangling dynamical effects and medium radiative corrections in photon yields. In general there is a lack of the $NN\gamma$ data and therefore the calculations must rely on theoretical models.

The inelastic nucleon-nucleon scattering provides also a powerful tool to investigate the nucleon-nucleon interaction and baryonic resonances. Recently high precision measurements of the reactions have been performed at 320 MeV for the quasi-free reaction $np \rightarrow pp\,\pi^-$. The considerable flux of high-energy neutrons at n_TOF (above 800 MeV) should allow the study of free *np* scattering and the understanding of the production mechanism of different species of mesons [16].

1.5.2 Neutron-Nucleus scattering

The main interest in the study of neutron-nucleus scattering concerns the optical potential. The importance of this parameter is well known, in particular in several reaction calculations [17]. The extraction of optical potential from elastic scattering data is somewhat ambiguous because cross-section and polarization data at a single energy do not determine the S-matrix uniquely. The neutron-nucleus scattering instead shows noticeable advantages: the absence of the Coulomb interaction, which avoids complications or corrections; the possibility of a direct comparison with the proton-neutron scattering; the availability of a polarization option, which would be interest of for many nuclear physics questions.

Inelastic scattering can provide important information on the nuclear structure and particularly the excitation of the nuclei. Specifically it is possible in such experiments to study neutron level densities, collective states and giant resonances.

Another fundamental research is the study of the nuclear fission induced by low energy neutrons in the energy range from 0.01 eV to 5 MeV. The experiments include the measurements of fission fragments and total kinetic energy distribution as a function of the incident neutron energy. From these data it is possible to obtain information on the nuclear viscosity, which plays an important role in the path from the saddle point of the fission barrier to fragment separation [18].

1.5.3 Neutron-electron scattering

An important quantity in the study of the hadronic structure is the mean square radius of the charge distribution $\left\langle r_n^2 \right\rangle$ which is proportional to the slope of the form factor $G_E(q)$ at q=0 and can be deduced from low energy neutron-atom scattering [19]. The corresponding experiments are based on the coherent interference between neutrons scattered by the nucleus and the electron cloud of the atoms.

The low repetition rate and the 200 meters of flight path of the n_TOF facility provide ideal conditions for a re-measurement of the angular distributions of neutron scattering on the noble gases, specifically on Xe. The use of gaseous sample avoids uncertainties due to the solid-state correction. The modern electronics and new method of analysis should allow to achieve the required accuracy [20].

Another important constant of the neutron structure is its electric polarisability α_n, which represents the response of the neutron to external electric fields. Because of the tight binding of the constituents of a neutron, strong electric fields are required to obtain a measurable effect. The simplest way to determine α_n is the measurement of the energy dependence of the total cross-section [21]. Such measurements have been performed in the past but require further refinements and higher accuracy, such as the one that could be obtained at the n_TOF facility at CERN.

Chapter II

2.1 Introduction

The requests for new and accurate data discussed in Chapter 1 can only be satisfied with an innovative facility capable of delivering a neutron beam with high intensity, white spectrum in a wide energy range, high resolution and low background. The n_TOF (neutron Time-of-Flight) facility, recently set-in-operation at CERN, was built to fulfill all these requirements. This chapter contains a description of the facility and of the main characteristics of the neutron beam, i.e. the flux, beam profile, energy resolution and background in the experimental area, which make the CERN facility a unique tool for measuring long-needed cross-section data for applications and Astrophysics.

The knowledge of the characteristics of the facility and of the neutron beam is a fundamental pre-requisite for an accurate estimate of the cross-sections. In this chapter, the main features of the n_TOF neutron beam will be presented. The flux and profile, the energy resolution and the background in the experimental area will be discussed. Some technical aspects of the facility, regarding the proton beam, the cooling system and the water moderator will be mentioned for completion, remanding to the references for further details.

2.2 Neutron production

Neutrons at n_TOF are produced by spallation of a high-energy proton beam from the PS accelerator on a Pb target. The process consists in a series of nuclear reactions in which the energy of incident particles is sufficiently high that several particles are ejected from the target nucleus changing atomic mass and number of all participants, see Figure 2.1. The spallation mechanism involves many nuclear processes, which can be distinguished on the time scale as: Intra-Nuclear Cascade (nucleon-nucleon collisions), Pre-Compound stage (pre-equilibrium, Multi-Fragmentation, Fermi Break-up), Compound Nuclei (evaporation,

high-energy Fissions), Inter-Nuclear Cascade (nuclei collisions) and finally at low energy inelastic and elastic reactions. A short list with all characteristics of those reactions is tabulated in Table 2.1.

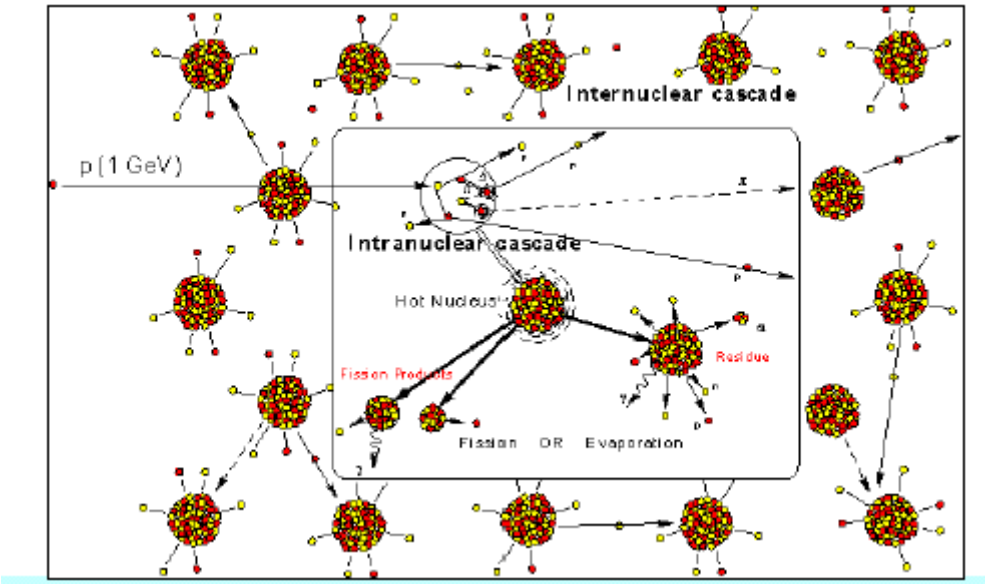

Figure 2.1: The various processes of the Spallation Mechanism are pictorially illustrated.

Table 2.1: Characteristic properties of the most common nuclear reactions.

Nuclear Reactions	Incident particles & Energies	Beam Currents (part/sec)	Neutron Yields (n/inc. part)	Target Power (MW)	Deposited Energy/Neutron (MeV)	Neutrons emitted (n/s)
(e^-,γ) & (γ,n)	e^-(60 MeV)	5×10^{15}	0.04	0.045	1500	2×10^{14}
^{3}H $(t,n)^4$He	^{3}H (0.3 MeV)	6×10^{19}	5×10^{15}	0.3	10^4	10^{15}
Fission			≈1	57	200	2×10^{18}
Spallation (non-fissile target)	P (800 MeV)	10^{15}	14	0.09	30	2×10^{16}
Spallation (fissionable target)			30	0.4	55	4×10^{16}

The characteristics of neutron beams produced in the spallation process are known and mainly depend on the primary beam and on the material composing the spallation target. The two most important characteristics of the spallation mechanism are illustrated in Figure 2.2 [23]. The number of neutrons produced per proton as a function of the beam

energy saturates at high energies (2 GeV for proton beams). For increasing energy of the primary beam, in fact, it is no longer correct to consider the nuclear reactions as proceeding through the formation of a compound nucleus with the consequent emission of nucleons and leptons; in this energy region the reactions between partons prevail with the consequent production of exotic particles containing strange, charm or beauty quarks. The material composing the spallation target has also a strong influence: the heavier the material, the greater the number of neutrons emitted per proton, as shown in Figure 2.2.

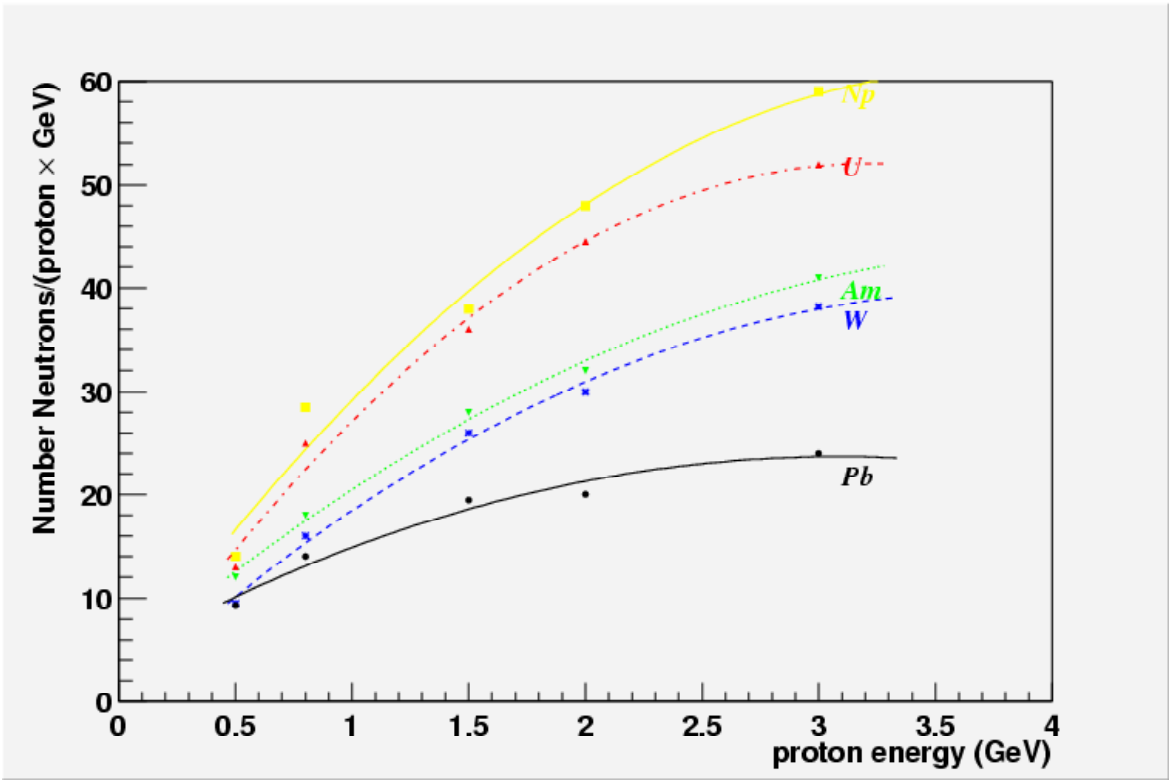

Figure 2.2: Number of emitted neutrons varies as a function of the target nuclei and energy of the incident particle (proton in this case) [61].

The most important spallation neutron sources in the world use different arrangements of target-beam. At the Los Alamos neutron facility (WNR) protons at 800 MeV impinge on a liquid Tungsten target [24]. At the Oak Ridge electron linear accelerator (ORELA), neutrons are produced by (γ,n) reaction from electron beams on Tantalum [25], while the Gelina facility in Geel is based on an electron beam on an Uranium target [26]. A short comparison between those facilities is indicated in Table 2.2. The chosen arrangement is mainly linked to the characteristics of the neutron beam and to the type of experiments planned. Some facilities in fact are designed to have high flux and low repetition cycle in a specific energy range useful for capture measurements; other facilities have lower flux but

higher duty cycle and can measure typically transmission (total cross section) or fission cross-sections. In all cases, it is fundamental to know the characteristics and properties of the facilities since they affect the experimental program.

The n_TOF neutron beam is produced by spallation of 20 GeV/c protons from the ProtoSyncrotron accelerator on a block of natural Pb 80×80×60 cm^3. A large number of secondary particles are produced by the proton beam on the Pb target (muons, protons, pions, etc…), emitted preferentially along the direction of the proton beam. To minimize the contamination of these secondary particles in the neutron beam, the proton beam line is impinging on the Pb target with an angle of 10 degrees relative to the neutron time-of-flight tunnel.

Table 2.2: Comparison between different neutron facilities.

Neutron Facility	Flux (n/sec)	Pulse Width (ns)	Repetition Rate (Hz)	Energy Range	Projectile Rate	Energy (GeV)	Target
WNR (Los Alamos)	10^{14}	0.18	800/100	>100 keV	2.4×10^{13} *p*/s	0.8	W
ORELA (Oak Ridge)	10^{14}	4-30	1000	<few MeV	3×10^{15} e^-/s	0.18	Ta
GELINA (Geel)	3×10^{13}	0.6	800	<few MeV	4.7×10^{14} e^-/s	0.1	U
n_TOF (CERN)	10^{16}	6	0.4→1.2	0.5-3×10^9 eV	1.3×10^{13} *p*/s	20	Pb

Neutrons emerging from the spallation target, in the forward direction, propagate in a vacuum tube positioned in the TT2A tunnel, approximately 7 meters below the ISR tunnel. An experimental area is located 200 m downstream from the spallation target in the existing TT2A tunnel. To direct the proton beam onto the Pb target, a new transfer line has been connected to the FT12 transfer line, as shown in Figure 2.3. The characteristics of PS machine, that is the high energy of the proton beam, the high current and the low repetition rate, result extremely convenient for an innovative neutron facility. The combination of these properties, in fact, allows to produce a unique high intensity pulsed neutron beam with energy spectrum extending up to several hundred MeV. Small modifications were necessary to adapt the PS proton beam for neutron production. A single proton bunch from the PS consists in 5×10^{12} protons, with momentum of 24 GeV/c and time resolution of 14

nsec. For the TOF facility, in the final phase before the extraction the bunch is compressed to 7×10^{12} protons, 20 GeV/c momentum and 6 ns time resolution. This compression allows to get higher neutron flux and better time resolution of the neutron beam, while the lower energy of proton beam do not significantly affect the total flux (at these energies of the primary beam the neutron/proton ratio saturates as shown in previous paragraph).

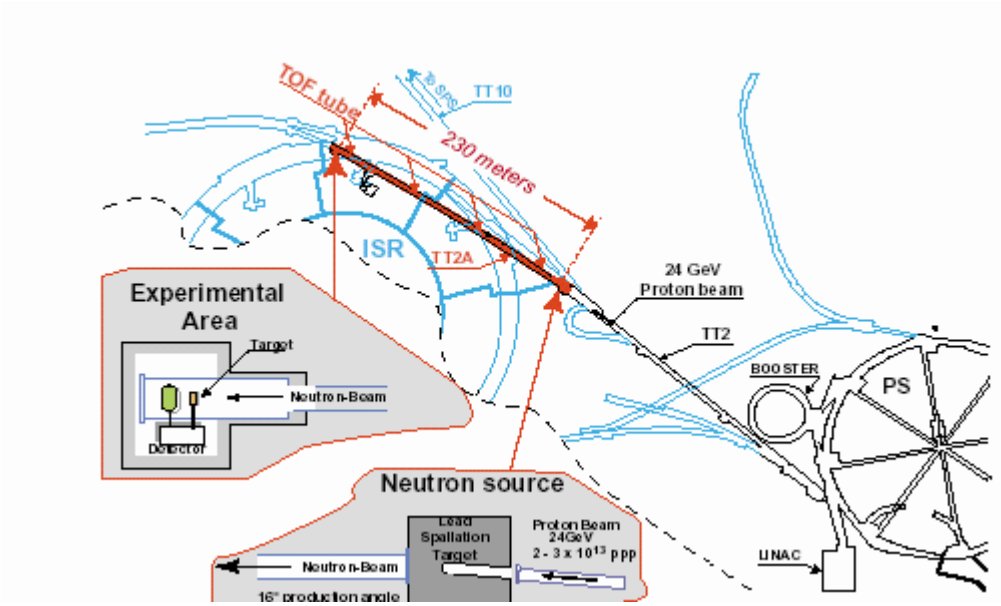

Figure 2.3: General layout of the n_TOF experiment. The proton beam via the TT2 transfer line hits the Pb target. At the end of the TOF tunnel neutrons the experimental area is situated.

Normally, two modes of operations are typically provided for the n_TOF beam: a dedicated mode and a parasitic one. In the dedicated mode, the bunch has the characteristics already described; in the parasitic one the number of protons delivered is only 4×10^{12}. The repetition rate of the proton beam is connected to the characteristics of the proton beam. The PS is typically operated so that several bunches, in dedicated or parasitic mode, and separated by a minimum of 1.2 seconds, can be accelerated and extracted for different users in within a given time interval, called "supercyle" (the duration of the supercycle may vary from year to year; currently it is around 16 s). In principle, several bunches during the PS supercycle could be delivered to n_TOF. In this case, proton bunches spaced by 1.2 seconds would be obtained, corresponding to a repetition rate of 0.8 Hz. In reality, however, the sharing of the PS with other experiments, and some technical limitation (in particular the temperature of the Pb target etc), are such that at most 4 proton bunches can be delivered to n_TOF in a supercycle, corresponding to a repetition rate below 0.25 Hz.

Figure 2.4: The Pb spallation target. It is possible to note on the left the TOF tube and on the right the cooling system.

The spallation target consists in a Pb block of dimensions 80(h)×80(R)×60(W) cm^3; those dimensions represent the compromise between the neutron flux and the resolution path $d\lambda$. The choice of the Pb presents many advantages and some disadvantages. The natural Pb, in fact, has high atomic number and high density; it is cheap and easy to machine. In Pb, one 20 GeV proton may produce several hundred neutrons. Finally Pb has high transparency to neutrons of energy less than 1 MeV. Other materials, such as Tungsten, have better neutron/proton ratio, but present problems in manufacturing and are quite expensive.

The target is surrounded by water acting both as coolant and as moderator. The large power dissipated by the incident beam in the Pb block, in fact, gives rise to a sensible increase of its temperature and makes necessary an efficient cooling. In the extreme conditions of four bunches per supercycle, the average beam current is 0.31 μA and the beam energy reaches the value of 85.6 kJ. According to simulations made with Fluka [29], the power deposited by the proton beam in the target is approximatelly 51% of the beam power, corresponding to 3 kW. Consequently, the maximum theoretical temperature increase during one bunch is 34.5 °C while the maximum asymptotic temperature in the center of the block is 135 °C. Cooling of the Pb block is therefore necessary. This is made by circulating 3 cm thick layer of demineralized water around the block, except for the TOF front face where the layer is 5 cm thick for the moderation purposes. The water is enclosed in an aluminum container, with an open window for the neutron beam pipe. The

interface between this window and the vacuum of the TOF tube is made by a single thin foil of aluminum 1.6 mm thick and 800 mm in diameter.

The water used for cooling acts also as a moderator, to shape the neutron spectrum to an optimal distribution. The moderation process in the 5 cm layer, in fact, allows to produce a neutron beam with isolethargic distribution (a flat distribution in the logarithm of the energy), over several orders of magnitude, as will be shown later on in the chapter.

2.2.1 The vacuum tube and collimators

Neutrons emerging from the Pb target are propagated in a vacuum tube inside the 200 meters TT2A tunnel. The TOF tube is made by four different sectors connected by flanges and delimited by concrete walls used for shielding, as shown schematically in Figure 2.5.

A complete list of the characteristics of four sectors is given in Table 2.3.

The first part of the vacuum tube, closest to the target, is made by aluminum alloy whereas the others are made of stainless steel. Immediately following the Pb target, the neutron beam pipe has a diameter of 80 cm, but several reductions along the path, mainly in the proximity of collimators, Pb to a beam tube of 10 cm diameter in the experimental area.

Table 2.3: Mechanical dimensions of the various sectors of the vacuum chamber.

Sector number	Length [m]	Ext. diam. [mm]	Thickness [mm]
1	10	812.8	8.0
2	40	609.6	6.0
3	150	408.0	4.0
4a	27	812.8	8.0
4b	3	812.8	8.0

Several collimators are mounted along the flight path, to shape the neutron beam to a desired size of 2 cm diameter in the experimental area. A first reduction is placed at a distance of 60 m from the Pb target and is made entirely of Iron, 1 meter thick. A “source-screening” collimator, two meters long and with aperture of 11 cm diameter, is placed in sector 2 at 136.7 meters from the target. The aim of this first collimator is to minimize the divergence of the beam in the experimental area, by delimiting the position and angle of emission of neutrons traveling from the Pb target to the experimental area. It is made of 1 meter of iron and 1 m of concrete.

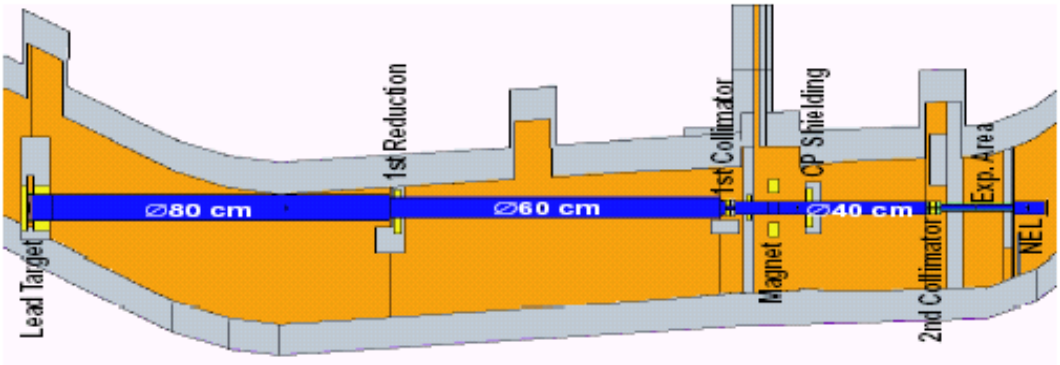

Figure 2.5: Schematic view of the TOF tube.

The main shaping of the neutron beam is however performed by a second collimator, therefore called “beam-shaping” collimator, placed at 178 meters from the target, just a few meters before the experimental area. A photo of the collimator is shown in Figure 2.6. The composition and dimension of this collimator is complicated, due to the wide energy range of neutrons to be stopped. It is divided in three parts: the first one consists of 50 centimeters borated polyethylene, with 5% concentration of ^{nat}B. This part stops mainly the low energy neutrons, preventing them from being captured later on and produce γ-rays. The second part is made of 125 centimeters of iron, whose aim is to moderate high-energy neutrons, while the third and final part is made of 75 centimeters borated polyethylene, with 5% Boron concentration, for final moderation and capture of the low-energy neutrons produced in the previous stage. The aperture of the collimator is 1.9 cm, optimized for the measurements of capture cross-sections, which require a small and well-defined neutron beam. A similar collimator, with larger aperture, has been constructed and is installed for fission cross-sections measurements. In this case, an aperture of 8 cm allows to exploit a wider neutron beam on thin samples (but with large area), necessary for the detection of the fission fragments.

Figure 2.6: The second collimator is necessary for the flux reduction in capture measurements.

After crossing the experimental area (delimited by two concrete walls), the neutron beam continues in a vacuum tube of 20 cm diameter and 12 meters length, called “the escape lane”. At the end of the tube, a polyethilene block ensures moderation of the neutrons with minimal backscattering, before they decay or are captured inside the walls and the floor of the last part of the tunnel (Figure 2.7).

Inside the experimental area, measurements are mainly performed in vacuum, except in some cases in which radioactive samples or other delicate instrumentation cannot be operated in vacuum. In this case, breaking of the vacuum for the necessary space is obtained by mounting tubes with kapton window at the vacuum-air interface, which produce little interference with the neutron beam.

Since high vacuum is not necessary for neutrons, a pressure of few tenths of mbar is kept inside the whole beam pipe by several mechanical pumps positioned along the flight path.

Figure 2.7: Neutron Escape Lane area. At the end of TOF tube is evident the polyethilene block for the beam dump.

2.2.2 Shielding

The background represents one of the most important aspects that characterize a neutron beam, as it largely determines the accuracy of the measured neutron cross-sections. Particular attention has to be devoted in minimizing the background at a time-of-flight facility, since generally it is not possible to identify and discriminate the spurious events from reaction events on the basis of the time information. Several sources of background can be present at a spallation neutron source: primary particles that cross the spallation target and propagate in the neutron direction; secondary charged particles produced by hadronic interation or by decay of other particles (π, κ, μ, e^-), neutron scattered by material along the flight path, in particular by the walls of the tunnel and by the collimators, and entering the experimental area. Finally, γ-rays can be abundantly produced in the spallation target, or by secondary particles (including neutrons) hitting the walls of the tunnel and the collimator. It should be noted that, together with the "ambient" background, which is present independently of the measurement being performed, other background components associated with the sample affect the determination of the neutron cross-section. These sample-dependent background (mainly due to scattered neutrons and γ-rays) will be discussed in a following chapter.

Figure 2.8: Sweeping Magnet.

To minimize the “ambient” background at the n_TOF facility, several shielding have been mounted along the flight path in the time-of-flight tunnel. A significant reduction of the secondary particle produced by the high-energy proton beam in the spallation target is achieved by a large shielding made mostly of concrete walls, placed immediately following the target. Since the first measurements at n_TOF revealed the presence of a large muon contamination outside the beam, the Pb target shielding was reinforced in order to prevent pion decay, mainly responsible for the muon production.

Since the collimator constitute a strong source of background (in particular neutron and γ-rays), concrete walls up to 3 meters thick are built following the two collimators, at 136 and 178 m. To allow access to the whole tunnel, the walls are made with chicanes. To reduce the high-energy muons, for which the concrete walls result inadequate, three meters iron wall has been added.

In spite of the 10° angle between the time-of-flight tube and proton beam, some charged particles still contaminate the neutron beam, propagating in the vacuum tube along the flight path. A large reduction of this contamination is achieved by means of a 2 meters long dipole magnet used to sweep these unwanted secondary particles out of the beam tube, towards the side walls of the tunnel or on the shielding placed before the experimental area. The magnet (Figure 2.8) is installed in the sector two at 145 meters and has a magnetic rigidity of 1.5 Tm, so that, all charged particles with momenta up to 10 GeV/c can be deflected out of the neutron beam.

The experimental area is positioned between the 185 and 190 meters and is delimited by two concrete walls, which shield the area on one end from the last collimator, and on the other end from backscattered neutrons or γ-rays.

2.3 The n_TOF neutron beam

The n_TOF facility was built with the aim of allowing accurate measurements of neutron cross-sections in a wide energy range. To this end, the facility has been designed so to produce a neutron beam with high flux, wide energy spectrum, low background in the experimental area and finally good resolution in time-of-flight (and therefore in neutron energy). The main factor that determines the characteristics of the neutron beam is the specific geometry of the spallation target and of the water moderator. In particular, while at high energy the resolution is determined by the time spread of the proton beam (6 ns), below 1 MeV it is strongly affected by the uncertainty in the moderation path length $d\lambda$. This can be minimized by choosing a smaller target or a thinner water layer, but at the price of a lower flux and a more limited energy spectrum. Since an interplay exist between flux, energy spectrum and energy resolution, the optimal configuration, that fulfills the best compromise between the different needs was studied by means of extensive simulations of the neutron production mechanism in the spallation target. The final choice for the geometrical parameters of the target and of the moderator, and their implications on the neutron beam are briefly discussed.

2.3.1 Flux

The simulations have been performed with two Monte Carlo codes: Fluka [29] and the EA-MC MonteCarlo code [30]. FLUKA generates spallation neutrons and transports them from high energies down to 19.6 MeV, while lower energy neutrons are transported by the EA-MC. The neutrons energy spectrum obtained with the described PS proton beam, for the various Pb target configuration and water moderator are shown in Figure 2.9. A target of large dimensions but no moderation results in a flux mostly concentrated at high energy. On the contrary, an iso-lethargic behavior, that is a flat distribution in the logarithm of the neutron energy, is obtained from 1 eV to 100 keV with the addition of a water layer, which represents a very efficient moderator due to the hydrogen content. The optimal

target-moderator combination (Pb 80×80×60 cm^3 block and 5 cm of water) produces a flat distribution with a substantial increase of the flux at very low energies and above 1 MeV. It should be noted that a gravitational cut-off occurs due to the length of flight path for neutrons with kinetic energy less than 0.02 eV, while above several hundred MeV, the neutron flux decreases due to the small probability of survival of high-energy neutrons in a large spallation volume. For this reason, conventionally, the useful energy range of the n_TOF neutron beam is indicated between 1 eV and 250 MeV.

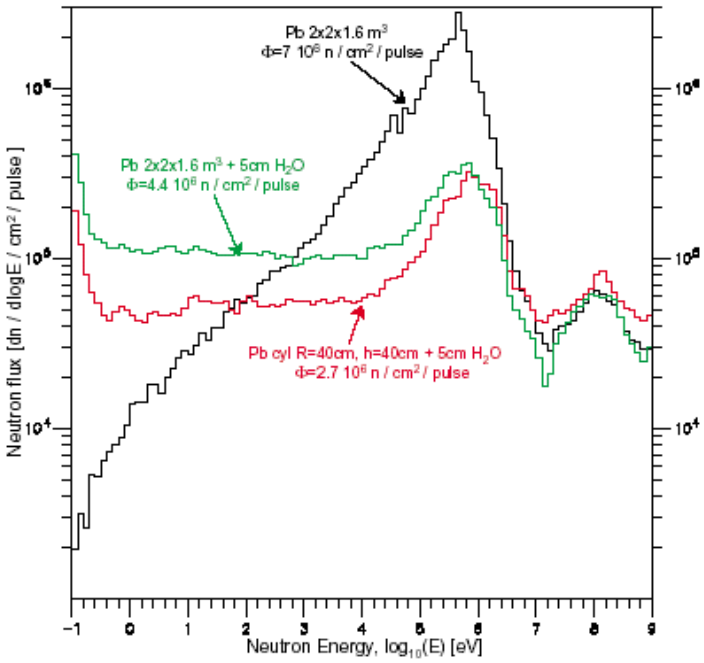

Figure 2.9: Neutron energy spectrum for various Pb target configurations with and without water moderator. The proton beam is the PS one, the details are in the text.

As will be shown in a following chapter the measurements of the neutron flux during the commissioning of the facility showed an agreement between experimental data and simulation results of the order of 20% in the whole energy spectrum. Considering the complexity of the simulation, this result confirms the validity of the neutron codes employed.

The expected neutron flux at n_TOF can be easily estimated from the simulations. The number of neutrons produced per proton inside the Pb target is approximately 300. Of these, approximately 68 enter the Time-of-flight vacuum tube; therefore the total number of neutrons produced in a supercycle, with 4 dedicated bunches of 7×10^{12} protons each, is as large as 1.9×10^{15}, or almost 10^{15} n/s, a number orders of magnitudes higher as compared to other existing facilities. After 187.5 meters and considering the solid angle, the moderation

process and the collimators, the number of neutrons is reduced to 1.4×10^5 neutrons/pulse/cm^2. It is important here to notice that the average flux at 200 m is comparable to the one available at other facilities at much smaller distance (for example, at Gelina at 30 m, see Figure 2.10), with the consequence that at n_TOF a much better energy resolution is obtained for the same flux. Most importantly, due to the very low duty cycle of the PS accelerator, the neutron flux at n_TOF is concentrated in a few bunches of 15 ms duration, separated by a minimum of 2.4 s (the duration of a neutron pulse, 15 ms, corresponds to the time of arrival of the slowest neutron, of 1 eV energy). Therefore, the instantaneous neutron flux, that is the number of neutrons per pulse, is almost three orders of magnitude higher than at any other facility. This extremely high instantaneous flux constitutes one of the most interesting and innovative aspects of the n_TOF facility, since it allows the measurement of radioactive samples, which would be nearly impossible to study anywhere else. In fact, the background associated with the natural radioactivity of the samples has hindered in the past the measurement of neutron-induced reactions, in particular capture reaction, on radioactive samples such as those of interest for the trasmutation project, i.e. long-lived fission fragments and actinides, and for energy production in alternative fuel cycles. The extremely high instantaneous neutron flux at n_TOF makes it a unique facility, where a reasonable signal-to-background ratio can be achieved even for highly radioactive samples.

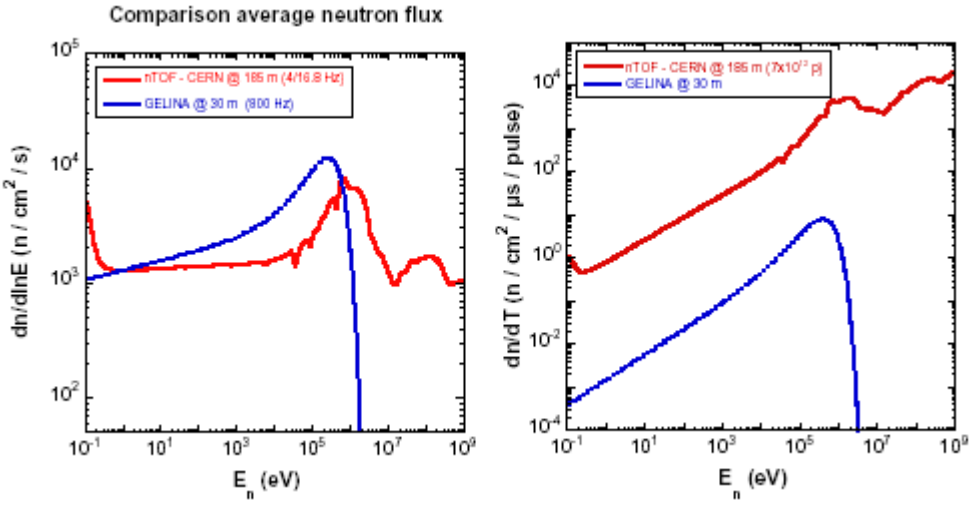

Figure 2.10: The neutron flux of GELINA at 30 m compared with the preliminary flux data from CERN-TOF at 185 m

The knowledge of the beam spatial profile assumes a considerable relevance especially in capture measurements. In this case in fact, the samples do not always cover

the whole area of the neutron beam and the intercepted flux depends on the sample dimensions. Simulations show that the beam profile at n_TOF can be approximated with a gaussian in two dimensions (see Figure 2.11). Because of the angular distribution of neutrons emitted from the Pb target, the dimension of the beam depends on the neutron energy, the higher the energy the smaller the beam profile. Table 2.4 contains a list of the values of the beam width obtained by the simulations, compared with the results of the experimental determination by the MicroMegas detectors [34].

Table 2.4: Variance of the beam profile extracted from the simulations and Micromegas detector.

Energy	σ_x (Simulation)	σ_y(Simulation)	σ_x(Micromegas)	σ_y(Micromegas)
10-100 eV	7.33 mm	7.30 mm	7.61 mm	7.21 mm
0.1-1 keV	7.32 mm	7.32 mm	7.41 mm	7.31 mm
1-10 keV	7.32 mm	7.32 mm	7.4 mm	7.6 mm
10-100 keV	7.32 mm	7.32 mm	7.9 mm	7.4 mm
0.1-1 MeV	7.20 mm	7.14 mm	6.6 mm	6.4 mm
1-10 MeV	6.28 mm	6.58 mm	6.6 mm	6.4 mm
10-100 MeV	6.00 mm	5.92 mm	6.4 mm	6.1 mm

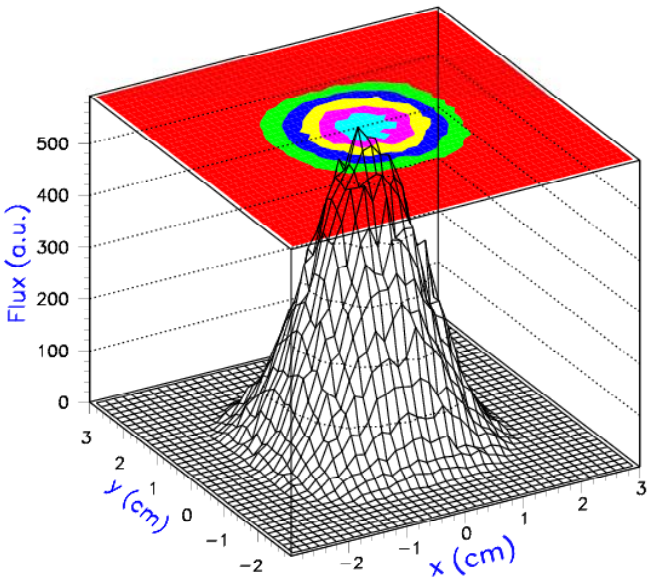

Figure 2.11: Spatial distribution of the neutron beam in the range of few eV.

2.3.2 Resolution

The time-of-flight technique consists in the determination of the particle's energy through the time measurement, according to an energy-time relation. In the relativistic case the relation is:

$$E = mc^2\left(\sqrt{1-\frac{L^2}{(tc)^2}}-1\right),$$

while in the non-relativistic case the classical expression is applied.

For an optimal determination of the particle energy, the neutron beam must have a time resolution comparable to the time resolution of the detectors of a few nanoseconds. In the case of the n_TOF neutron beam, two factors affect the energy resolution: the time resolution of the proton beam, important only at high energy and, the moderation process in the Pb spallation target and in the water layer surrounding it.

As already mentioned, some modifications of the proton beam have led to an improvement of the PS bunch resolution from 14 to 6 ns (root mean square). This factor dominates for neutron energies above 1 MeV. At lower energy, the biggest effect is related to the process of neutron moderation, or slowing down, in the spallation source and in the water moderator. Since the moderation process through successive scattering is a stochastic process, an intrinsic uncertainty exists on the time spent by the neutron in the spallation target (also called thermalization or moderation time). However, as predicted by the simulations and verified experimentally in a previous experiment [28], in a material having a large atomic number the slowing down time and the energy of outgoing neutrons are correlated. This sharp correlation is valid only in the region where the elastic scattering dominates (E<10^4 eV). More precisely, for a large block of Pb, the energy of the emerging neutron and the moderation time are inversely correlated, the larger the moderation time, the lower the energy. This can be understood intuitively by considering that, to emerge with low energy, a neutron must undergo a large number of scatterings, with the result of a longer thermalisation time inside the target. The correlation between neutron energy (or velocity) and time delay is such that an effective neutron path λ inside the target can be defined:

$$\lambda = v \times t\,,$$

where v is the velocity of the neutron when entering in the time-of-flight tube and t is the time elapsed since its creation (in this case, since the arrival of the proton beam on target). The thermalisation time, in this picture, is replaced by an increase in the flight base by an

amount equal to λ, so that the total "apparent" flight path becomes $\lambda+L$ (where L is the flight path). Alternatively, it can be thought as a displacement of a virtual neutron source emitting the neutrons already with their final energy. Such a virtual source would be located on a plane parallel to the outer face of the spallation target, but at a distance of $-\lambda$ from the real source, along the neutron beam direction.

Clearly, the energy resolution is affected by the uncertainty in the thermalization time or, equivalently, by an uncertainty in the "apparent" flight path $\Delta\lambda = v \times \Delta t$ ($\Delta\lambda$ representing the root mean square of the λ distribution, defined above). The following relation can be written:

$$\frac{dE}{E} = \frac{2 \cdot d\lambda}{\lambda + L}.$$

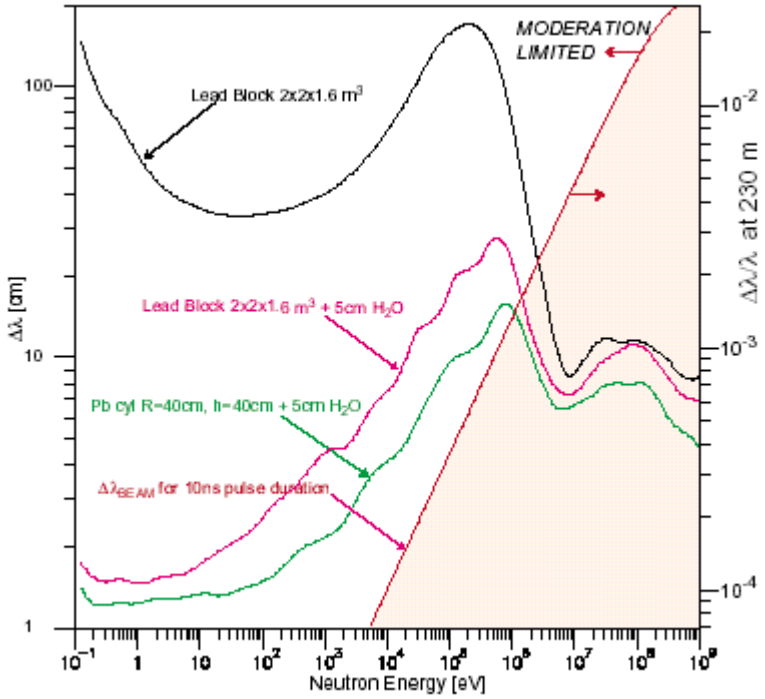

Figure 2.12: Uncertainty in the path $d\lambda$ as a function of neutron energy for different spallation target configuraitions. It is shown also the uncertainty due to the PS pulse duration 10 nsec.

It should be noted that a much smaller $\Delta\lambda$ can be obtained, at the price of a lower average energy spectrum, by using an additional hydrogen-rich moderator (such as water) at the exit of the spallation target. In this case, due to the high moderation efficiency associated with proton scattering, the neutron speed v is abruptly reduced by a large factor in a small moderation volume and with negligible additional thermalization time. As a consequence, $\Delta\lambda$ is reduced. This method is applicable in the n_TOF case, since the initial

neutrons energies are high and can be conveniently reduced, allowing to study cross-sections between 0.1-10^4 eV. In this case, the addition of 5 cm water moderator produces a large improvement of the energy resolution (see Figure 2.12).

Simulations of the complete target plus water set-up have allowed to estimate the additional flight path λ=5.7 m, and associated uncertainty $d\lambda$=0.33 m (valid for $E<10^4$ eV).

The energy resolution can now be easily calculated, according to the above expression. Considering for instance, an experimental area located at a distance from the spallation target of L=200 m, the resulting energy resolution is $dE/E = 2.87\times10^{-3}$, energy independent up to 10 keV.

This value represents an improvement relative to other existing neutron beams. Although in principle it could also be obtained in any facility, by choosing an appropriately large flight-path, only the high flux available at n_TOF allows to combine a good resolution with a still reasonable flux at 200 m.

2.4 Background

Another important aspect of any neutron facility is the background, which considerably affects the accuracy of the cross-section measurements. At monoenergetic neutron sources, spurious events can be discriminated from the reactions being investigated on the basis of the time information. This is however not possible at a Time-of-Flight facility, where in principle background events cannot be identified by the time information, and more complicated methods have to be applied (such as the calorimetric method for γ-rays in studies of capture reactions). Therefore, a large effort has to be devoted to minimize all possible background contributions.

The determination and the minimization of the background at the n_TOF experimental area was carried out by the n_TOF collaboration and SL-EET group at CERN. A large plan of simulations and measurements was undertaken to this aim both during the design phase of the facility and during the campaigns of measurements [32]. The first set of measurements performed by the n_TOF collaboration, showed that the background was about two orders of magnitude larger than tolerable, making it impossible to pursue the foreseen experimental program. This evidence determined a change in the

original design and required new measurements in order to understand and to solve the causes of this background.

Different sources of the background affect any time-of-flight facility. One of the most important is due to overlap between bunches. In this case, slow neutrons from one bunch could be misidentified as fast neutrons in the next bunch. This is a serious problem in several neutron facilities for example at Oak Ridge, Los Alamos and needs particular attentions; the energy of neutrons is usually selected by speed-chopper. At n_TOF, this background is practically absent; since even the slowest neutrons with energy less than 0.01 eV (450 ms in time-of-flight) are quite below the minimum time separation between proton bunches, which is 1.2 sec.

Two more types of background can be distinguished at n_TOF: the “ambient” background, detected in the experimental area when no sample is being measured (but the neutron beam is present) and a sample-related background. This second type depends on the particular sample and will be discussed in a following chapter together with the results of the measurement. Furthermore, the importance of the different components depends on the measurement and the type of detector being used. As an example, γ-ray detectors used in the measurements of capture cross-sections will be very sensitive to γ-ray background, while fission measurements, mainly based on gas detectors, are affected only by the presence of a neutron background. For this reason, each measurement requires a detailed analysis of the associated background.

We concentrate here only on the ambient background, which is intrinsic to the facility and independent on the particular measurement being performed.

Several sources of background can be identified at n_TOF. Inside the neutron beam, the biggest contamination comes from highly energetic charged particles, not deflected by the magnet, and by γ-rays coming from the spallation target. Both types of background give rise to a prompt flash (often referred to as γ-flash, although it is due also to charged particles), arriving 600 ns after the proton beam reaches the spallation target, as expected for particles traveling at or near the speed of light over the 200 meter path. If too strong, this flash may increase the dead time of the detectors, making them blind (that is insensitive) to high energy neutrons. γ-rays from the spallation target are present also at later times. They are mainly produced by inelastic or capture reactions of neutrons inside the Pb target or in the water moderator and affect primarily the measurement of capture reactions (as will be shown in a following chapter).

Outside the neutron beam, the main contribution to the background originates from neutrons leaking through the shielding concrete walls in the detector station, and from neutrons and γ-rays entering the detector station through the vacuum tube, after being scattered on the beam pipe or on the walls of the tunnel. In the first measurement campaign, one more unexpected component was observed. This was related to negative muons reaching the experimental area and captured in the walls of the experimental area. Following muon capture, neutrons are produced by evaporation and diffuse in the experimental area. The discovery of the muon component required an addition of a 3 meter thick iron wall for shielding.

Although the most accurate way of determining the background is by measuring it, some estimates of the expected background at n_TOF can be made on the basis of simulations of the neutron beam transport through the various elements of the facility, in particular the spallation target, the collimators and the escape lane. It should be noted that the level of background depends on the geometry of the TOF tube, the collimator apertures, and the distance of the experimental room from the spallation target.

2.4.1 Neutron background

The main contributions to the presence of these particles in the experimental area, are caused by neutrons leaking through the shielding concrete walls (out-beam component) in the detector station and neutrons entering the detector station through a scattering with the walls of the TOF tube (in-beam component) [31].

Neutrons with small angles relative to the beam line, after a given flight path collide with the TOF tube and start a random path in the tunnel; the simulations show that these neutrons introduce a significant background in the detector station equivalent to the 1% of the initial neutron beam. The evident solution to avoid this type of background is the appropriate enlargement of the radius of the TOF tube such that even the most divergent neutrons cross the TOF tube only 30 m after the detector station. Moreover, neutrons scattered on the TOF tube or leaking through the shielding can be reflected and found with random incident angle in the experimental area. Therefore it is necessary to divide the tunnel, by concrete walls 2-3 meters thick, into several compartments before and after the detector station where the tube is enlarged.

In particular, the neutrons of the beam passing through the sample under study and reaching the end of TOF beam pipe can re-enter by backscatterings in the experimental

area. The mean free path in air for neutron is around 20 meters, thus a few meters of air are enough to introduce a backscatter background. The simulations have determined that 8 meters of vacuum pipe after the detector station and a concrete wall are sufficient to eliminate such background.

In a geometry made with compartments, another contribution to the neutron background arises from the neutron scattering on concrete and entering through the beam pipe in the experimental area. In order to avoid these neutrons an additional concrete shielding of 5 meters around the neutron tube in the direction away from the detector station, is required.

In both cases the shape of the energy spectrum of the background neutrons is almost the same, as shown in Figure 2.13. The major difficulty only arises for the detector station at small distances (80 meters) due to the fast neutron component. Fast neutrons may in fact generate secondary neutrons either by spallation or by other mechanisms, requiring thicker concrete shielding.

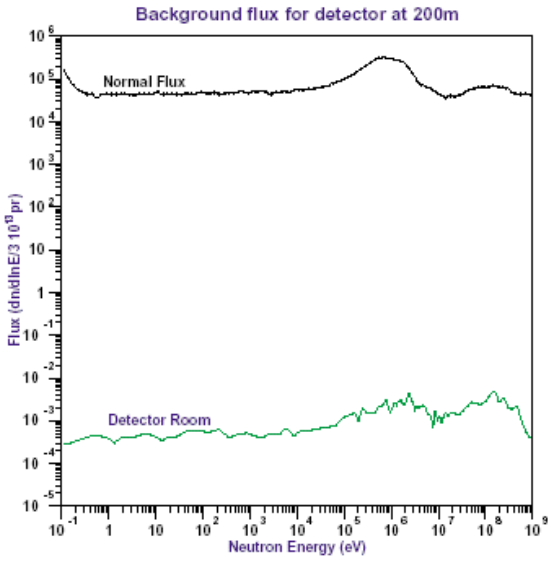

Figure 2.13: Neutron induced background at 200 meters.

Finally, a few words should be said about the beam halo. To reduce the radius of the neutron beam, the use of collimators is necessary. Some halo may however still survive in the neutron beam profile, which is larger for smaller flight paths. At small distances, in order to minimize this halo it is necessary to use more than one collimator, with a substantial reduction of the neutron flux. At large distances, only one collimator is necessary, producing a sharper beam profile, leaving the neutron beam almost unaltered.

2.4.2 Photon background

The background γ-rays present in the experimental area are mainly related to the in-beam photon component. The γ-rays are copiously produced in spallation target by several mechanisms. Among them, the most important ones are the neutron capture by Pb and especially by the Hydrogen of the water moderator, and the annihilation process. The distribution of the photons is simulated with FLUKA; the spectrum extends from several keV up to several GeV, as shown in Figure 2.14; there is a fast component due to the spallation mechanism and a slow component due to the thermal or epithermal neutrons captured in the elements of the spallation target [33].

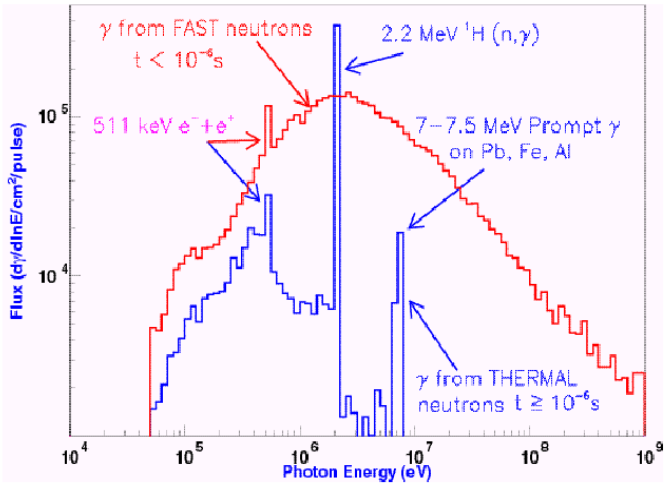

Figure 2.14: Photon distribution at 200 meters. The peaks due to the annihilation (511 keV), to hydrogen capture (2.1 MeV) and to Pb capture (7-7.5 MeV) are evident.

2.4.3 Charged Particle background

Together with neutrons and γ-rays, a lot of charged particles are created in the spallation target. With the use of FLUKA, the charge distribution is estimated at the exit surface of the water moderator or in other words at the entrance of the neutron tube. The main goal of this simulation is to determine the strength of the required magnetic field by evaluating the maximum momentum of the charged particles. Figure 2.15 shows a rather sharp fall of the momentum at 10 GeV/c [33]; using a 2 meters long sweeping magnet with a magnetic field of 1.03 Tm, the 10 GeV/c particles are swept out of the neutron tube at a distance of 15 meters.

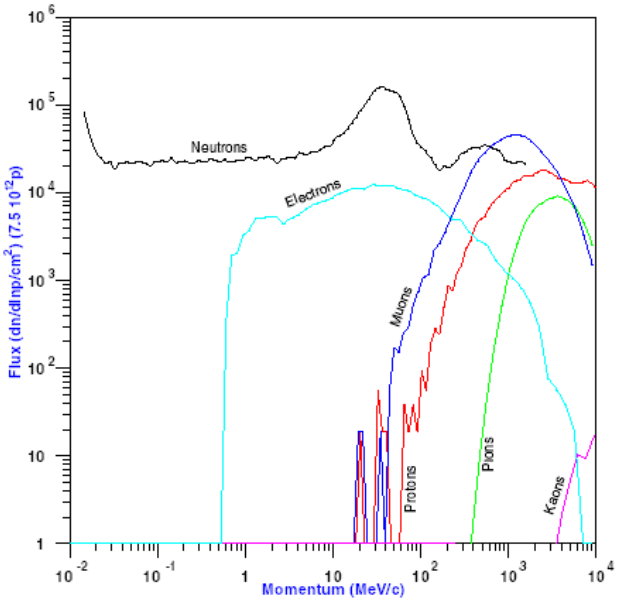

Figure 2.15: Fluxes of the charged particles as function of their momentum.

Chapter III

3.1 Introduction

High accuracy measurements of neutron cross-sections at n_TOF require state-of-the-art experimental apparata. High performance detectors and data acquisition system are in fact necessary to fully profit from the innovative features of the facility. As an example, to match the low background of the installation, new detectors with small sensitivity to sample-scattered neutrons have to be developed. Similarly, the extremely high instantaneous flux of the n_TOF neutron beam requires a fast Data Acquisition System. In this chapter, the main features of the experimental apparatus used for capture and fission cross-sections will be described.

The complete setup consists of the following devices:

- A low-mass flux monitoring system based on Silicon Detectors;
- An array of low-sensitivity liquid scintillator γ-ray detectors C_6D_6 (deuterated benzene), for capture cross-section measurements;
- A carbon fiber sample changer, remotely controlled;
- A set of Parallel Plate Avalanche Counters (PPAC) for Fission cross-section measurements;
- An acquisition system based on fast Flash ADC, in compact-PCI standard;
- A position sensitive gas chamber "MicroMega" for beam profile determination;
- Several dedicated detectors, such as HyperPure Germanium detectors (HPG), Thermoluminescence Detectors (TLD), etc, used for specific measurements in particular for the background and for *(n,xn)* reactions;
- Finally, data processing and analysis required the development of state-of-the-art software tools and analysis technique.

The main features of the experimental apparatus and techniques are described in details in the following paragraphs.

3.2 Silicon Monitor

In order to measure neutron cross-sections with the required precision of a few percent, it is important to determine the neutron fluence (that is the neutron flux integrated over the time of the measurement) and its dependence on the energy. Typically, this is done by means of standard neutron detectors placed in the beam during the measurement. ^{10}B chambers and fission chambers are the most common and natural choice. In both cases, the products of a known reaction, such as the ^{10}B(n,α) or the ^{235}U(n,f) reactions, are detected in a gas volume of an ionization chamber. The energy range in which the neutron flux has to be measured, determines the reaction to be used. Considering the reaction cross-sections, ^{10}B(n,α) and ^{6}Li(n,α) are used from thermal to approximately 1 MeV neutron energy [48], while fission chambers are used also for higher energy neutrons.

For the monitoring of the neutron flux at n_TOF, a slightly different approach has been adopted, with the aim of minimizing the perturbation produced by the monitor on the neutron beam and, especially, the background induced by the flux monitor in the experimental area. To this hand, a low-mass system has been designed, built, tested and permanently installed in the experimental area. It consists in a thin Mylar foil, 1.5 μm thick, with deposit of ^{6}Li or ^{6}Li compound such as ^{6}LiF, placed in the beam. A set of 4 Silicon detectors, placed outside the beam and viewing the foil, ensure the detection of the tritons and α-particles emitted following neutron capture by ^{6}Li (Figure 3.1). They are placed symmetrically outside the beam and around it at 45° with respect to the beam axis and at a small distance from the foil, in order to cover a large solid angle. The well known, smooth and large cross-section of the ^{6}L$(n,\alpha)^{3}$H reaction, considered as standard of measurement, allows to monitor the neutron flux from thermal up to 1 MeV. The registered signals from the Silicon detectors provide information on the time-of-flight and on the deposited charge.

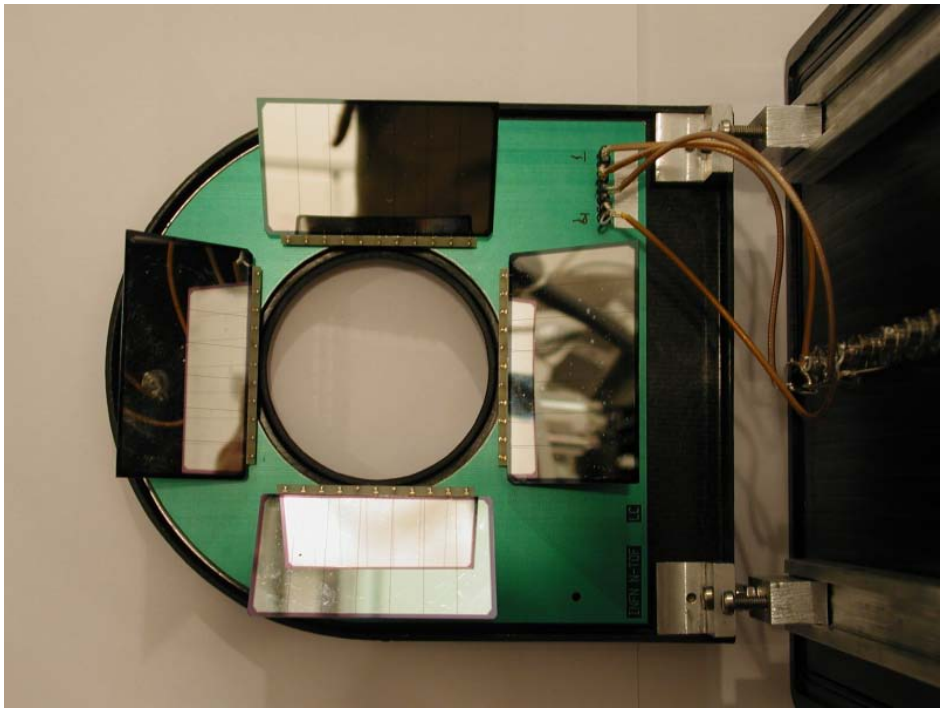

Figure 3.1: The set of 4 Silicons disposed around the centre where is placed the Lithium foil.

The system is mounted inside a carbon fiber scattering chamber, which in turn is mounted on the neutron beam line, at the entrance of the experimental area, as shown in Figure 3.2. Since some neutrons are scattered out from the beam by interaction with the Mylar foil and the ^{6}Li deposit, particular care has to be taken in reducing the amount and composition of material surrounding the flux monitor. In fact, the capture of elastically scattered neutrons in high cross-section material produces γ-rays, which could constitute a background for the measurement of capture cross-section in the same experimental area. To minimize such background, the vacuum chamber has been constructed with carbon fiber. Carbon has a very low capture cross-section and the properties of mechanical resistance of the carbon fiber allow to build very light vacuum chambers.

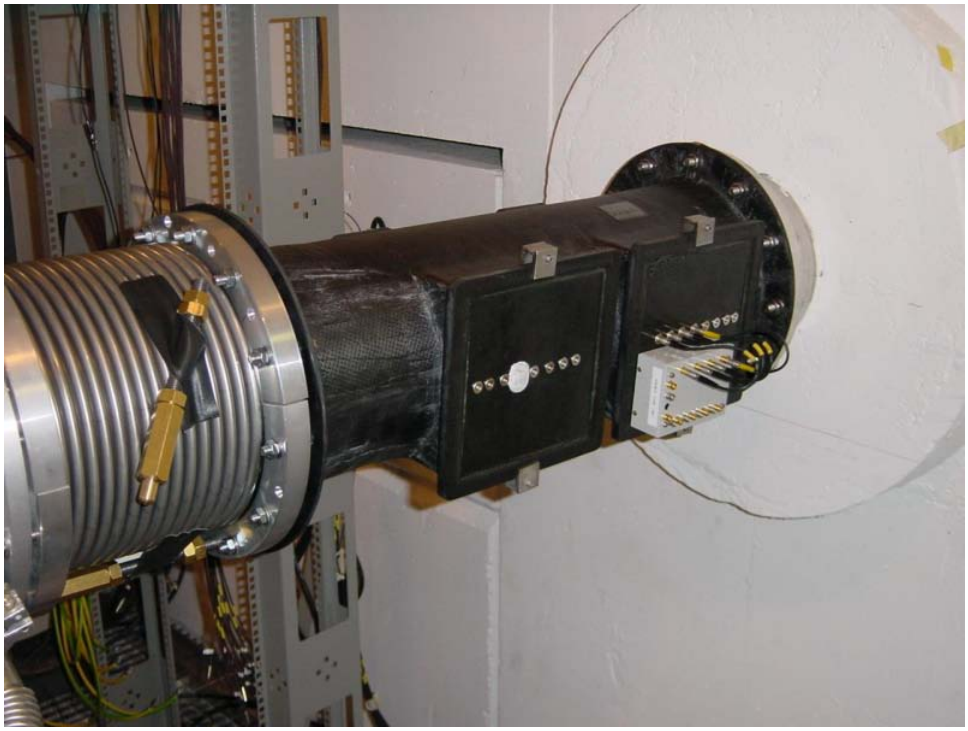

Figure 3.2: Carbon Fibre vacuum chamber containing the silicons plus the lithium foil is inserted in the beam.

To optimize the design of the system, extensive Monte Carlo simulations have been performed. The thickness of the ^{6}Li deposit, for example, has to be chosen as a compromise between the need of a high count-rate and that of a good discrimination between tritons and α-particles (the energy of the detected particles deteriorates with increasing thickness due to the energy loss inside the deposit itself). Simulations are also necessary to estimate the background induced by the system.

Monte Carlo simulations of the flux Monitor were done with GEANT-4. A schematic description of the apparatus was implemented in the code. The low-energy routines were used for neutron transport, while the electro-magnetic routines were chosen in order to calculate the energy deposition of the charged particles (α-particles, tritons and protons) in the Silicon detectors. For some specific cases, simulations were also done with the older GEANT-3.21 and the results were compared. The energy resolution of the Silicon detectors was included in the simulations. This was estimated in laboratory tests, performed with α-particle sources.

Figure 3.3 shows the results of the simulations for different thickness of the ^{6}Li and ^{6}LiF deposit. The plot shows the energy deposited in the detectors, convoluted with the measured resolution of 150 keV. As evident, the optimal solution is a deposit of 500

μg/cm^2 ^{6}LiF or equivalently 200 μg/cm^2 of pure ^{6}Li. In this case, in fact, the peaks of triton and α-particles are still clearly separated. The identification of the two regions is essential if only tritons have to be used in the analysis, in case part of the α-peak falls below the threshold.

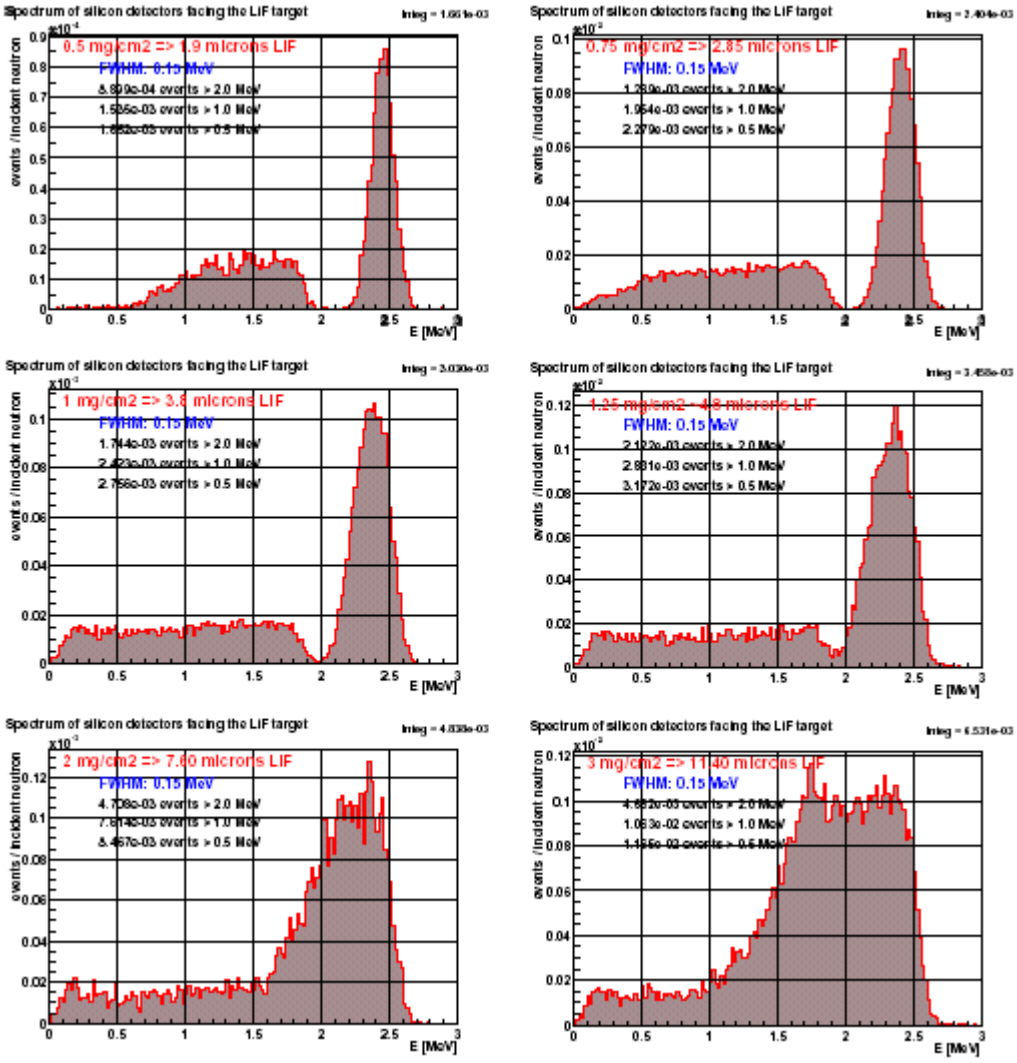

Figure 3.3: ^{6}LiF spectra for 150 keV FWHM resolution for the silicon detectors.

The charged produced in the Silicon detectors are collected through the low-noise two stages pre-amplifier EV 5194, with sensitivity of 20 mV/MeV. It is then shaped by means of a Fast Timing Amplifier ORTEC model 863, with a time constant of 200 nsec. The resulting gaussian signal is directed to the Flash ADC, operated with a 200 MHz sampling rate.

To reconstruct the neutron flux from the monitor detectors, the recorded time-of-flight spectrum has to be corrected for the geometrical acceptance and the well-known ^{6}Li$(n,\alpha)^3$H reaction cross-section.

The results of the flux measurement with the monitor detector will be discussed in the next Chapter. The device provides a measurement of the neutron flux integrated over the beam profile, with a precision mainly depending on the knowledge of the thickness and homogeneity of the ^{6}LiF sample. Although the uncertainty on these quantities can be as large as 10%, it should be noted that the main objective of this device is the monitoring of the flux and of the stability of the neutron beam and providing a relative normalization between different measurements, while the accurate absolute determination of the neutron fluence can be obtained by the ^{197}Au*(n,γ)* reaction, for capture cross-sections, or by the ^{235}U*(n,f)* for fission measurements.

3.3 Apparatus for capture cross-section measurements: the C_6D_6 detectors

The measurement of neutron capture cross-sections is based on the detection of γ-rays emitted in the de-excitation cascade following neutron capture (see Figure 3.4). Two methods are typically used for the measurement: the pulse height weighting function technique and the calorimetric method. The first method consists in the detection of only one γ-ray per cascade, but with efficiency independent on the γ-ray multiplicity and average energy of the cascade. To this end, low-efficiency detectors are used, but their response function is modified by software. On the contrary, the calorimetric method consists in detecting the whole γ-ray cascade, by means of a device with high detection efficiency and covering close to 100% of the solid angle. The advantages of a 4π calorimeter are the large efficiency, which result in a small measurement time, and the possibility to discriminate the background, typically consisting in only one γ-ray of low energy, on the basis of the hit multiplicity and total detected energy. A 4π calorimeter made of thick BaF_2 crystals is currently being built for n_TOF. A few details will be given at the end of this chapter.

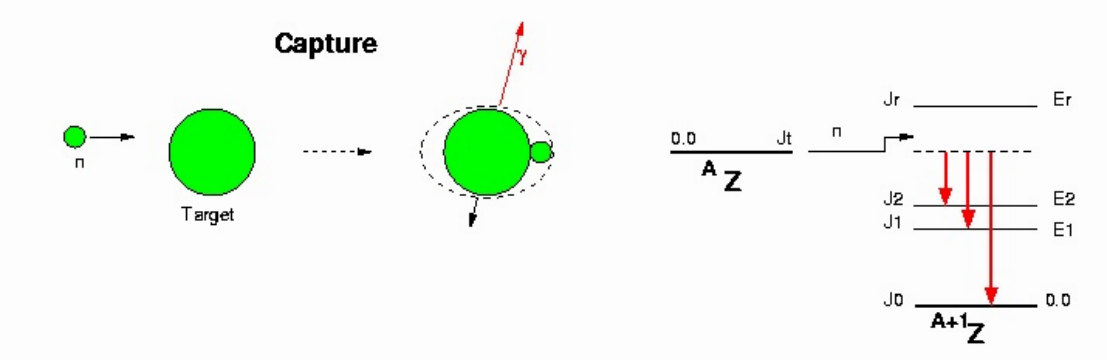

Figure 3.4: A schematic view of the neutron capture reaction and the corresponding de-excitation mechanism.

During the construction phase of the calorimeter, measurements of capture cross-sections at n_TOF are carried out with an array of low neutron sensitivity C_6D_6 liquid scintillator detectors (deuterated benzene), with the Pulse Height Weighting Function method. Due to the low atomic number of organic scintillators, the detectors present a low efficiency to γ-rays in the range 0-10 MeV, which is the typical energy range of γ-ray emitted in nuclear transitions. Combined with the small coverage of the solid angle, an overall efficiency of less that 10% is achieved, which results in the detection of at most one γ-ray per cascade, a requisite for the application of the Weighting Function method.

One of the problems of the use of liquid scintillators for capture measurements is that the method does not allow to distinguish γ-rays originated from neutron capture in the sample from the background produced by cosmic rays, ambient radioactivity and γ-rays from other reaction channels (fission, inelastic, etc). Most importantly, while scattered neutrons can be identified and rejected thanks to the n/γ discrimination property of liquid scintillators (described in Appendix I) [52], γ-rays produced by scattered neutrons captured in material surrounding the sample or in the detector itself cannot be distinguished from capture events in the sample. Therefore, particular care has to be taken in minimizing the probability of neutron capture outside the sample.

A large effect is obtained by using C_6D_6 deuterated liquid scintillators, instead of the more typical BC501 or NE213 organic liquid scintillator containing hydrogen, since the former scintillator avoids the neutron capture by hydrogen with consequent emission of a 2.2 MeV γ-ray. The low neutron sensitivity of C_6D_6 detectors can be further decreased by an optimization of the amount and composition of the support structures. In particular, an important effect has been obtained by the use of Carbon fiber in all mechanical supports.

The very low capture cross-section of Carbon and the good mechanical properties of the carbon fiber, in fact, allow to minimize the probability of neutron capture around or inside the detectors.

When using C_6D_6 detectors, a correction for the geometric and intrinsic efficiency of the detector has to be applied. This is typically made by using the Pulse Height Weighting Function technique described in a later paragraph.

Another problem that has to be addressed is the subtraction of the γ-ray background. Since this background component varies according to the sample under study, being mainly induced by in-beam photons, it needs an appropriate study related to the specific measurement. A complete treatment will be given when discussing the determination of ^{151}Sm cross-section (Chapter 5).

3.3.1 Set-up

Two different types of C_6D_6 were used in different n_TOF experiments. The type used in the first measurement campaign is a commercial detector, manufactured by Bicron, with some improvement implemented by Bicron, according to the n_TOF requirements. The detector consists of an aluminum cell filled with BC-537 liquid scintillator [50] and coupled to a XP4512 Photonis phototube [51]. The dimensions of the cell cavity are 101.6 mm diameter and 76.2 mm height for an active volume of the 611.6 cm^3; the wall thickness is 0.5 mm while the bottom is 1 mm thick. A photo of the detector is shown in Figure 3.5. A boron-free quartz window has been mounted on the phototube, to minimize its neutron sensitivity.

Table 3.1: Efficiency of C_6D_6 detectors for γ-rays emitted from a ^{197}Au sample, 45 mm diameter and 1 mm thick.

Photons Energy (MeV)	Bicron	FZK
1.266	6.1%	9.5%
2.209	5.5%	7.8%
3.163	4.9%	6.8%
4.386	4.4%	6.1%
5.515	4.2%	5.7%
6.183	4.1%	5.5%
7.383	3.9%	5.2%
8.392	3.9%	5.0%

Figure 3.5: Bicron C_6D_6.

The second type of C_6D_6 detector, particularly suitable for low capture cross-section measurements, has been designed and manufactured within the n_TOF collaboration at Forschungszentrum Karlsruhe (FZK) laboratory. The detector has a larger active volume, in order to increase the efficiency and to reduce the contribution of the support material, and the container is made with carbon fiber. The cell dimensions are 127.3 mm diameter and 78 mm height, for an active volume 992.24 cm^3, while the walls of the container are 0.4 mm thick (the bottom is reinforced to 0.7 mm thickness). The phototube is an EMI 9823QKA [52] with quartz window of 5 inches diameter. In order to have a better coupling with the phototube, the carbon fiber cell is directly glued to the photomultiplier and then filled with liquid scintillator. A photo of a prototype used in a test measurement is shown in Figure 3.6.

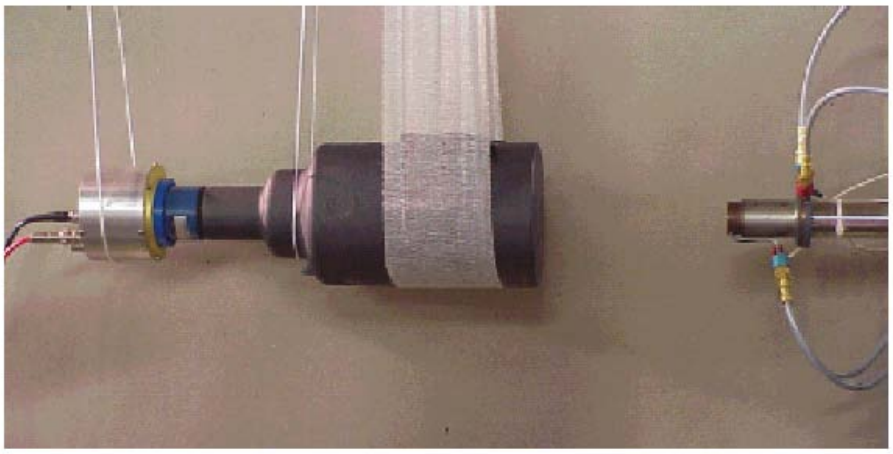

Figure 3.6: C_6D_6 designed at FZK laboratory.

A comparison between the two detectors was made by means of Monte Carlo simulations performed with GEANT-4 and GEANT-3.21 (a schematic view of the two detectors is shown in Figure 3.7). The same set-up of the experiment was implemented, with the two detectors perpendicular to the beam-line and at a distance of 4.5 cm from the center of a ^{197}Au sample from which γ-rays are emitted. The results of the efficiency for different γ-rays energies are reported in Table 3.1.

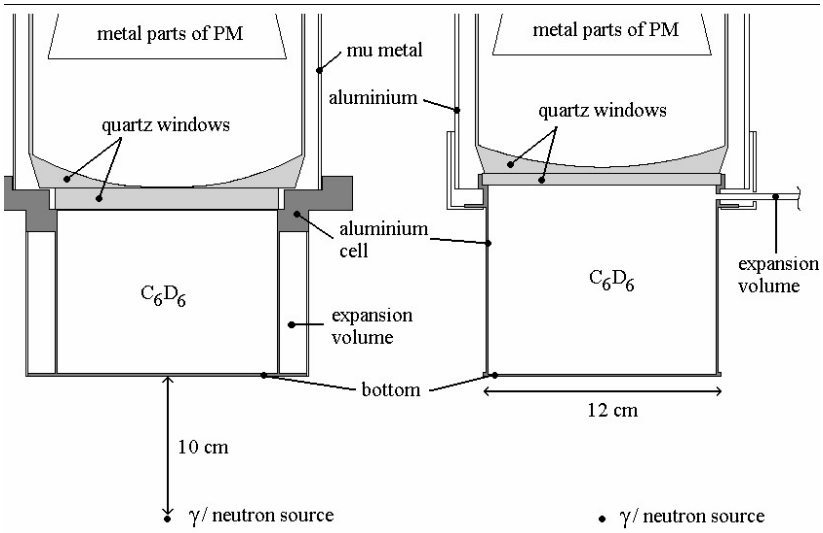

Figure 3.7: Schematic view of the C_6D_6 detectors used at n_TOF. Bicron is on the left while FZK on the right.

They indicate that the carbon-fiber C_6D_6 detector presents an efficiency approximately 50% higher than the Bicron detector, due to the larger volume. Although this is also valid for neutrons, it should be considered that neutrons of energy below 1

MeV, that is in the range of interest typical of capture reactions, produce a light output of less than 200 keV electron equivalent (keVee). Therefore, a threshold of the same magnitude is often sufficient to discard the neutron contamination.

3.4 Sample changer

For an accurate experimental determination of the cross-sections, several “reference” samples have to be measured in each experiment. As shown later, it is important to collect data on an empty sample, for “ambient” background monitoring, on C and Pb for sample-induced neutron and γ-ray background and on Au for absolute normalization purposes (all samples in each experiment have to be of the same radius of the sample being investigated). During a single measurement, different samples have to be inserted several times in the beam. For this reason, a remotely controlled sample changer has been built, in order to save time. To minimize the background, the structure has been made in carbon fiber. The sample changer is essentially a vacuum chamber in which a target ladder holding the samples is moved by means of an electrical stepping motor remotely controlled with a LabVIEW Instrument.

The sample changer is placed in the experimental area at 158 cm from the floor and 212 cm from the ceiling of the tunnel. It consists of two crossed tubes made of carbon fiber, as shown in Figure 3.8. The composition of the carbon fiber including the glue used in the construction is described in Table 3.2. The first tube runs along the beam line with an inner diameter of 50 cm; the connection with the TOF tube is obtained with an aluminum flange. The second tube is perpendicular to the beam direction has an inner diameter of 80 cm.

Table 3.2: Carbon Fiber composition in atomic fraction:

Atomic Element	Abundance (%)
C	74.85
O	23.13
F	1.57
Cl/Ca	0.46

Figure 3.8: Carbon fibre Sample changer for the measurements of the sample in the vacuum.

Two cylindrical shaped boxes placed at the top and at the bottom of vertical tube allow the installation of the samples and the lodging of the stepping motor (Figure 3.9). A carbon fiber strip, 100cm×7cm×300μm, lodge up to ten different samples, separated by a distance of 10 cm. Each sample is glued on a kapton foil and inserted in a square frame, 7 cm side. More specifics of the apparatus can be found in the Table 3.3 and in reference [53].

Table 3.3: In table are resumed the characteristics and obtained results for the 4 tubes constituting the sample changer.

	Radius r (mm)	Length l (cm)	Thickness s (mm)	80% of q' (bar)
T1	25	100	2	13
T2	40	100	2	77
T3	82.5	72	5	83
T4	157.5	42	7.5	341

Another sample changer was constructed in order to perform the measurements of the sample in air. It consists in a Carbon fiber strip connected to the stepping motor, with two aluminum plates on top and on bottom for mechanical support.

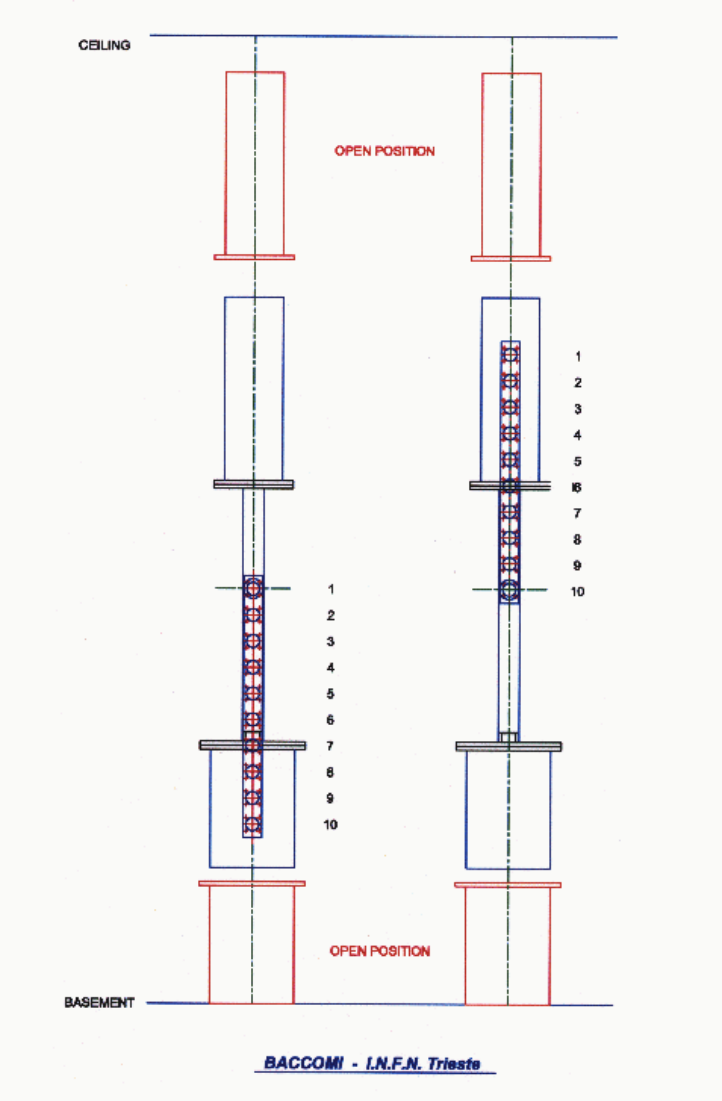

Figure 3.9: Detail of the Carbon fibre strips lodging the samples.

3.4.1 Pulse Height Weighting Function

As mentioned before, the C_6D_6 (in FZK or Bicron set-up) is a low-efficiency detector for γ-rays in 0-10 MeV energy range. This feature does not allow the detection and reconstruction of the whole γ-ray cascade emitted in capture reactions. Furthermore, since the efficiency depends on the γ-ray energy, different cascades paths are detected with different probability (de-excitation cascades may differ from each other for their γ-ray

multiplicity and average energy). If not corrected, this effect leads to large uncertainties in the reconstructed cross-sections.

In order to correct for the detector efficiency, a Pulse Height Weighting Function technique has been proposed [54]. It consists in modifying by software the detector response function so that the efficiency for detecting a γ-ray is proportional to its energy, that is:

$$\varepsilon_\gamma = kE_\gamma .$$

As a consequence, the overall efficiency for detecting a cascade (in the assumption that at most one γ-ray per event is detected), becomes proportional to the energy of the cascade E_c and independent from other details of the cascade, such as the multiplicity, deexcitation path, etc:

$$\varepsilon_c \approx \sum_j E_j = kE_c ; \qquad (3.1)$$

where E_j are the energies of the photons composing the cascade and k is a proportionality constant.

The modification of the detector response is performed by means of suitable "weighting functions", applied to the spectrum of the energy deposited by the γ-ray in the detector. It is evident that the accurate determination of the cross-section in this method relies essentially on the precise determination of the weighting functions, so that a particular attention has to be devoted to calculating the weighting functions.

In order to achieve the desired proportionality, the detector response function *R(E)* (or R_i in the discrete notation typical of measured spectra) is weighted by means of an ad hoc function *W(E)* (or W_i). This is calculated by minimizing, for various γ-ray energies, the difference between the integrated weighted spectrum and the γ-ray energy, according to the chi-square formula:

$$\chi^2 = \sum_i \left(\frac{\sum_j R_j^i W_j - kE_i}{\sigma_i} \right)^2 ; \qquad (3.2)$$

Here R_j^i is the response function of the detector to a γ-ray of energy E_i, σ_i is the relative error on the integrated response, and the sum over i is performed for several energies in the typical range of nuclear capture reactions, below 10 MeV.

In order to calculate the weighting functions, the response function of the detector has first to be determined. To this end, two methods can be used. In the first one, developed by

Corvi et al. [37], the response of a C_6D_6 detector is experimentally determined by means of a coincidence with another detector whose characteristics are well known (for example a calibrated Germanium detector). The use of *(p,γ)* reaction on ^{26}Mg, ^{30}Si and ^{34}S allows in this case to study the response of the detector to several γ-rays of energy up to 8.4 MeV. However, this "hardware" approach presents several problems. Monoenergetic γ-ray sources up to high energy are not easily available; it is difficult to take accurate measurements at low energy (less than 100 keV) because of the background and particularly of secondary radiation emitted by materials surrounding the detectors. All these effects can result in an overall uncertainty larger than the few percent requirements. For this reason, a different method has been applied in the n_TOF case, purely based on simulations. A comparison between the results of different reliable codes (MCNP, GEANT-3, GEANT-4, EGS, etc…), currently available, allows to minimize the uncertainties typically associated with simulation. More importantly, the accuracy of the simulations is verified "a posteriori", by applying the method to measurements of well-known cross-sections.

The simulations here discussed were performed with the code GEANT-3.21 (a test was also performed with GEANT-4, which gave similar results). A realistic description of the geometry and materials of the experimental set-up was implemented in the simulations. A complete simulation is made for each sample under investigation.

The γ-rays of given energies were generated according to the neutron beam gaussian profile on the surface of the sample and with a depth uniformly distributed inside the sample. The following discrete γ-ray energies were simulated, according to the work by Corvi et al.: 1.266, 2.209, 3.163, 4.386, 5.515, 6.183, 7.383, 8.392 MeV. For a realistic description of the response function, the simulated energy deposited in the C_6D_6 was convoluted with the detector resolution, estimated from the spectra measured for the calibration γ-ray sources ^{137}Cs and ^{60}Co. It should be considered that the resolution may vary depending on the detector type, the HV applied and other details. In the first measurements performed with the Bicron detectors, it was found that a good reproduction of the light output spectrum could be obtained by using a variance with a linear dependence on the light output, according to the relation $\sigma^2(E) = c \cdot E$, where E is expressed in keV. The proportionality constant c depends on the detector used. Figure 3.10 shows the measured response to the two sources, compared with the results of the simulations, for the

commercial Bicron detectors. As shown later, however, a formula with two energy terms was found more appropriate for a different detector.

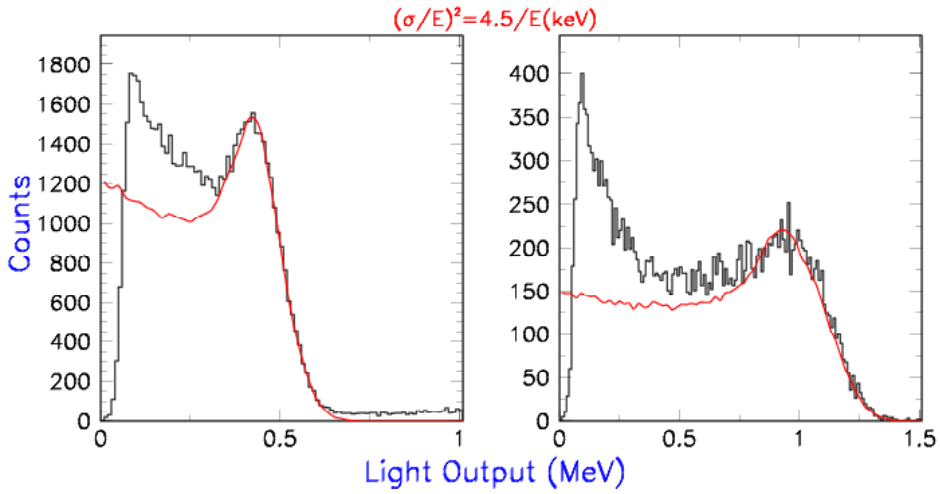

Figure 3.10: Energy calibration and resolution for one Bicron PH168 C_6D_6-detector.

Once the response function of C_6D_6 for different γ-ray energies is obtained, the weighting functions W_i can be determined by minimization of the chi-squares according to the Equation 3.2. After testing different functions, a 4th order polynomial was chosen, which seems to be the simplest formula that gives a reasonably low chi-square.

The minimization is performed with the code MINUIT implemented in the ROOT analysis package [55]. The fitting procedure allows to extract the five parameters representing the *W(E)*, as a function of energy. In the minimization, a threshold (100 or 200 keV) in the simulated spectra is applied, to account for the threshold used on the C_6D_6 signals during the experimental measurements. In this way, no correction is later required for the missing portion of the detector response spectrum. In order to extract the parameters with relative errors using Equation 3.2, the variance of the detector response function σ has to be defined. Two sets of parameters for each sample were calculated, corresponding to two different assumptions on the variance. The first one is extracted by fixing the value of σ equals to 1 for all bins of deposited energy; while the second set is obtained by using the errors according to the Poisson distribution. As shown later for some specific cases, the results obtained in the two cases are almost equivalent. Figure 3.11 shows the extracted response function and the corresponding weighting function for the ^{197}Au. The set-up

simulated consisted of two Carbon-fiber C_6D_6 described before, positioned perpendicular to the beam-axis at 4.5 cm from the center of the sample, with the vacuum sample changer. A threshold of 200 keV was kept on the detector light output in the analysis and in the simulations.

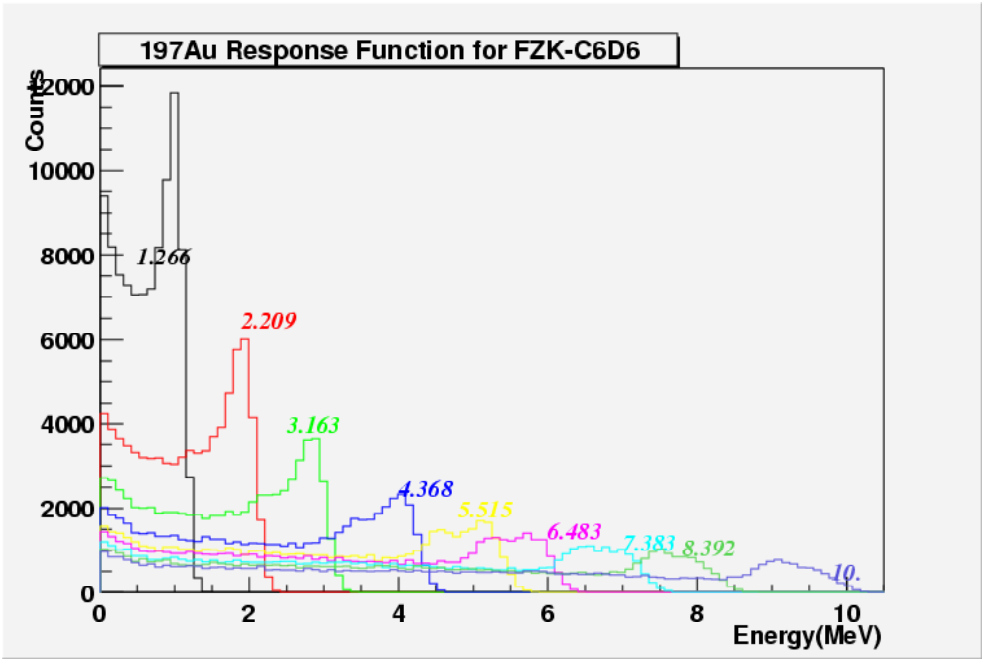

Figure 3.11: Response function to the γ-ray emitted from ^{197}Au sample in the n_TOF-02 campaign set-up.

3.5 Apparatus for fission cross-section measurements: the PPAC detector

Fission measurements at n_TOF are performed by means of several Parallel Plate Avalanche Counters (PPAC). These detectors have been known since many years as a precise timing instrument but were scarcely used before the considerable development of heavy ion physics. They consist of two thin parallel foils with a very low gas pressure in between (few millibars). The principle of detection is the same of multiwire proportional chambers. The gap between the two foils must be small in order to maintain a high electric field, for reducing the time spread and achieving good time resolution. The electric field has to be uniform to insure the same operating regime on the whole active surface of the detector. Thin foils are composed by aluminized Mylar; the printed circuit is in copper on a board coated with epoxy resin. These detectors are built to operate with pressure ranging

from 1 up to 20 mbar. Under these low-pressure conditions, a few hundred volts applied between plates (typically 300 Volts/cm/mbar) are sufficient to reach the proportional regime. Electrons produced by the ionization of particles crossing the detectors perpendicular to the planes, gain enough energy to induce immediate secondary ionization in the homogeneous electric field, forming Townsend avalanche. Pure hydrocarbons are generally adequate to reach higher gains. Multiplication factors of several thousands allow to obtain 100% efficiency in a wide domain of energy losses. For large energy losses, as in the case of Fission Fragments, pulse height saturation can occur and therefore a relatively low voltage is set. Only the fast component (2-3 ns rise time) produced by the motion of the electrons is collected, while the slow part, related to the ions, is suppressed by differentiation. In these conditions, a time resolution of the order of 250 psec (FWHM) is obtained with such detectors. The spatial resolution is given by the 2 mm Al strips deposited on the Mylar foil (the strips are 0.9 mm thick).

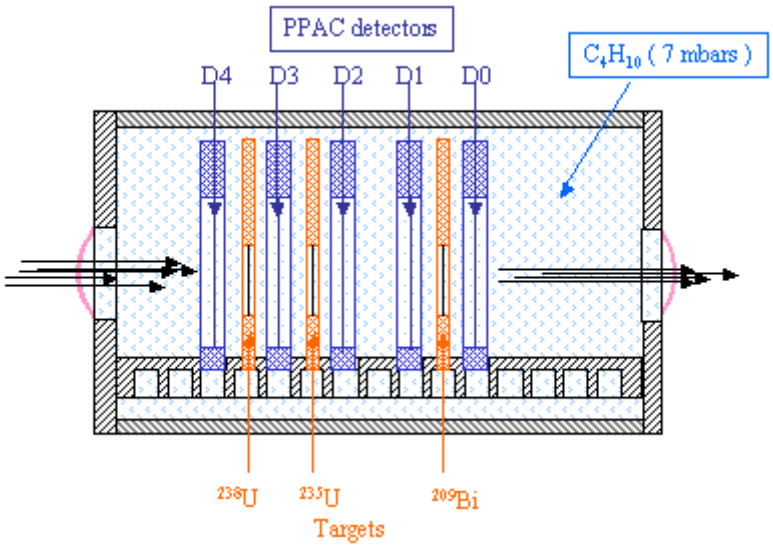

Figure 3.12: Schematic view of PPAC detectors. The several stacks are mounted in between the fission samples.

The sample to be measured is placed in between two PPACs. For higher count rate, a stack of several detectors (Figure 3.12) can be used, with samples of the same isotope between them. The distance between the PPAC and the sample is 5 mm. This way, both Fission Fragments, emitted back-to-back (at low energy), can be measured in coincidence, thus allowing for a good background rejection. Since the PPAC operates at low gas pressure (7 mbar), with a thin Mylar window for background minimization, the detectors are mounted in a vacuum chamber connected to the TOF tube, as shown in Figure 3.13.

Figure 3.13: The vacuum chamber of the PPAC detectors (left) and the associated gas and safety control unity (right).

The fission setup just described allows also to measure the neutron flux at higher neutron energy. In this case, the standard fission cross-sections of ^{235}U, ^{238}U and ^{209}Bi. These samples are permanently installed and during all measurements they serve as a flux monitor for normalization purposes. The thickness of the sample is 300 μg/cm^2 because the detection efficiency is limited by self-absorption.

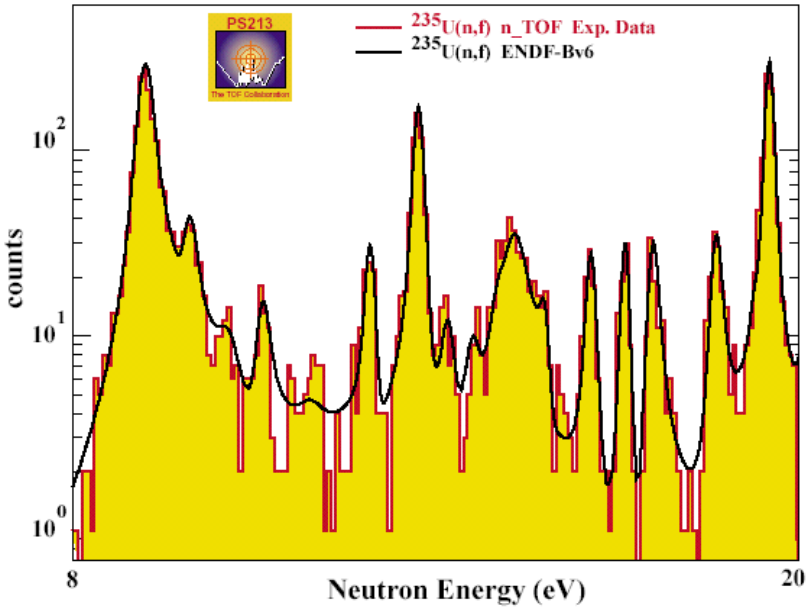

Figure 3.14: The measured fission yields with PPAC compared to evaluated data in the energy range from 8 to 20 eV.

Figure 3.14 shows the preliminary results extracted from the ^{235}U sample in the PPAC. The experimental data are compared to the evaluated cross-sections tabulated in the

ENDF-B VI database in the energy range from 8 to 20 eV [62]. The figure clearly demonstrates the high accuracy achieved at n_TOF also for fission measurements.

3.6 The n_TOF Data Acquisition System

Among the different characteristics of the n_TOF facility, one of the most important is the very high instantaneous neutron flux (up to 3 order of magnitude higher than for other facilities). While this feature represent a great advantage, especially for the measurements of small mass and radioactive samples, it poses some problems on signal processing and acquisition. In fact, the high-count rate, which is a direct consequence of the large neutron flux, results in a high density of signals and, therefore, in high pile-up probability. In those conditions, standard Data Acquisition Systems (DAQ) would be inadequate, since they would be affected by a large dead time. Moreover, it would not be possible to identify and reconstruct pile-up events, with the obvious consequence of large systematic uncertainties on the extracted cross-sections.

To overcome this problem, an innovative system has been set-up. The main feature of this system consists in the possibility to sample and record the full analogue waveform of the detector signal, which can later be analyzed off-line to extract the required information (time-of-flight, charge, amplitude, particle identification, etc…).

The sampling is performed by means of Flash Analogue to Digital Converter (FADC). In order to reduce the amount of data stored, on-line zero-suppression and a “tar” compression file format are used.

Once collected, the data of all detectors are transferred after each burst to the Central Data Recording (CDR) at CERN through a Gigabit switch for data storage.

3.6.1 FADC Modules

In order to record the shape of signals produced in fast detectors, such as the C_6D_6 liquid scintillator cells or the PPAC, Flash ADC with high sampling rate have to be used. The modules chosen at n_TOF are the commercially available DP 240 and DP 270, from ACQIRIS [56], with up to 2 GHz sampling rate. For a single channel, it consists of a PCI-card connected directly to the PC motherboard; for multichannel system, the cards are plugged in a Compact-PCI crate interfaced to a PC by a controller and a standard DMA

cable (see Figure 3.15). Together with the high sampling rate, the Acqiris digitizer was chosen because of its flexibility and adaptability to the different detection systems used at n_TOF. The basic module has a dynamic range that can vary from 5 mV up to 5 V, in positive and negative polarity, 8 bit resolution and the sampling rate can range from 1 Msample/sec (1 sample every 1 μs) up to 2 Gsample/sec (1 sample every 0.5 ns). Finally, it is equipped with a memory of 16 MByte, which allows to record data continuously at 1 GHz for 16 ms duration.

Figure 3.15: The Acqiris digitisers and the chassis;

At n_TOF, the acquisition of any detector signal is triggered by the PS pulse. For 16 ms following the start, the detector output is sampled. However, to reduce the amount of transferred data, a software zero-suppression is applied after writing the raw data to memory, but before the transfer to disk (the procedure is discussed later in more details). For any signal above a user-defined threshold, a number of samples, including some pre- and post-samples are recorded and transferred to disk.

Together with the commercial Acqiris module, a new and improved FADC has been designed specifically for the needs of n_TOF, by a collaboration between n_TOF and an electronic industry, ETEP [56]. The main improvement consists in a much larger memory on board, 512 Mbytes, which allows much faster transfer operations. Furthermore, a hardware zero-suppression is already implemented on the module, before writing to memory in order to make the operations faster. The module is currently in the commissioning phase and could substitute the commercial ones after completing the test

process. The main advantage of the new module is related to its large memory depth, which provides a very long recording time particularly useful not only at the n_TOF facility facility but also at other neutron sources.

Architecture

The Data Acquisition System Flow Chart in Figure 3.16, shows schematically the elements of the n_TOF DAQ system:

- The “Front End and Monitoring”, with the data streams for the different detectors;
- CDR Disk buffering, required to interface with the mass storage system;
- Data Transfer to Mass storage system (HSM);
- Off-lines event building and writing with a Processor farm for the Data Summary Tapes (DST).

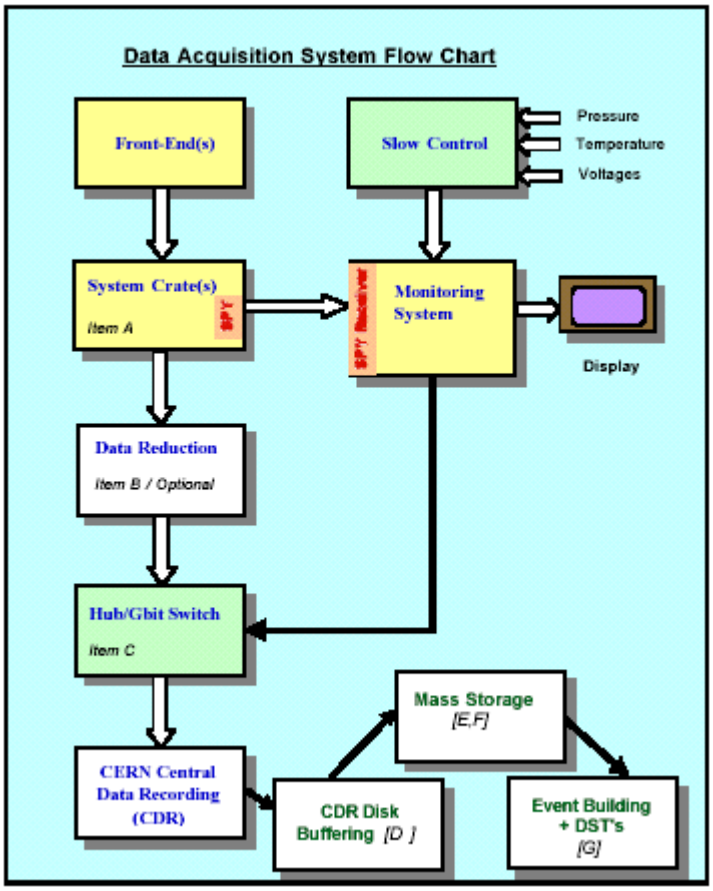

Figure 3.16: The block diagram of the n_TOF DAQ.

In a typical measurement, in which several detectors are used, the raw data are organized in 4 streams of 8 channels each, for a maximum of 36 channels. All modules are placed in the experimental hall, close to the detectors, to avoid signal degradation. A fifth stream is used for slow control information (pressure, temperature, voltages, sample in the beam, etc). In addition, information on the proton beam current, provided by the PS control-room, is also included in the stream. The data transfer to the CDR is performed via an optical Gigabit switch while a 100 MByte Ethernet switch connects all PC in the experimental area and in the n_TOF control room. A disk server (500 Gbytes) and several PCs for on-line monitoring of the detector signals and for slow control information are located in the control room.

Zero-Suppression

The goal of a zero-suppression algorithm is to remove useless information from the data stream either by hardware, before writing to the acquisition memory (ETEP digitizers), or by software after writing the detector data (ACQIRIS digitizers). The method consists of few simple steps, schematically shown in Figure 3.17: the user chooses a fixed threshold, above which a signal is considered valid; all samples with value above threshold are stored; in addition, a defined number of samples recorded before the signal crosses the threshold (pre-sample period) and after falling below it (post-sample period) are also stored, since they can provide information on the baseline, the root mean square of the noise, etc. All other samples are discarded, as they are considered noise. It is important to notice that if new valid data arrive during the post-sample period, the interval is reset and the post-sample interval is pushed forward until data fall below the threshold again, as shown in Figure 3.18. This important feature allows to correctly record pile-up events, which can be subsequently analyzed. A detailed discussion on the pile-up reconstruction procedure is given in Appendix I.

The prompt beam pulse of the PS, suitably attenuated and delayed, generates a trigger signal for the DAQ. This signal is split in a Fan-out module and distributed to the individual digitizers. It is used to make a gate of 16 ms, which is kept active during the whole acquisition period.

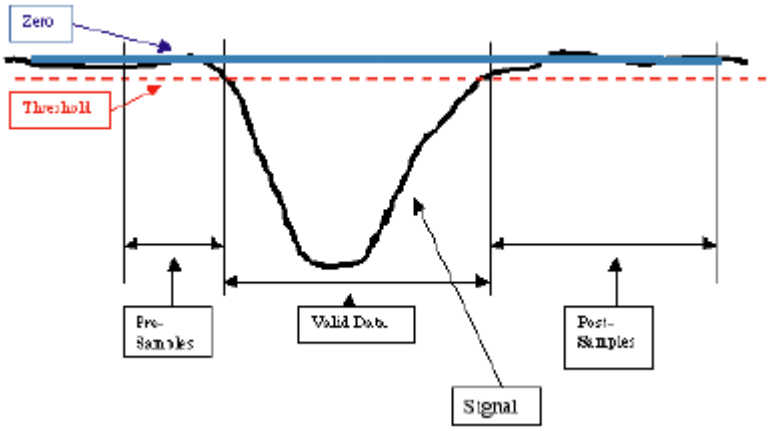

Figure 3.17: Schematic view of the pre-samples, valid data and post-samples.

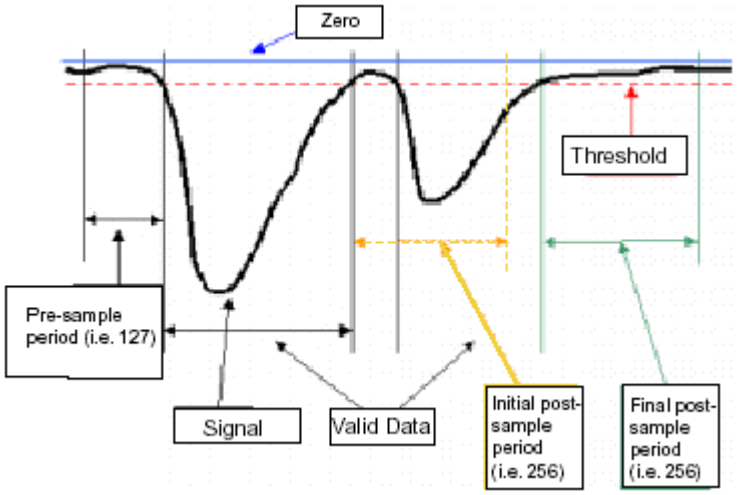

Figure 3.18: Additional pulse occurring during the post-sample interval.

Few remarks should be made on the dead time of the system. As mentioned, the digitizers acquire data in a period of 16 ms following each proton bunch (one byte per sample). Therefore, the recorded data amount to 8 MBytes per channel and per proton bunch, at the typical sampling rate of 500 Msample/s. The transfer time of 8 MBytes to the PC memory on the PCI bus is approximately 0.7 sec. On the PC, data are compressed so that a total of 10 MBytes for 5 streams are observed on average. They are transferred via the Gigabit Switch to the disk server in the control room in ~0.1 sec, while the transfer from the control room to the CDR takes another 0.1 s. If the time difference between two successive proton bunches is at least 1.2 s, the DAQ system is not affected by dead time. Such a condition persists for a peak data-rate of 18 MBytes/s, well above the typical present operation time at n_TOF [53].

3.7 BaF_2

The best signature for the identification of the neutron capture event in cross-section measurements via the TOF technique is the total energy of the γ-cascade by which the compound nucleus de-excites to the ground state. Hence, accurate measurements of *(n,γ)* cross sections can best be performed by using a detector that operates as a calorimeter with good energy resolution. In the reconstructed total γ-ray spectrum of such a detector, all capture events fall in a peak centered at the neutron binding energy (typically between 5 and 10 MeV), well separated from the γ-rays background. Furthermore, the resulting total energy spectrum is independent of the multiplicity of the γ-ray cascade, if high-efficiency detectors are used. These arguments have led the n_TOF collaboration to pursue the construction of a 4π calorimeter, made of a scintillator with high efficiency, reasonably good time and energy resolution and insensitive to the scattered neutrons. These aspects have been combined in the design of the 4π BaF_2 detector, which consists of 42 BaF_2 crystals forming a spherical shell, 15 cm thick. A part of the 4π calorimeter is illustrated in Figure 3.19.

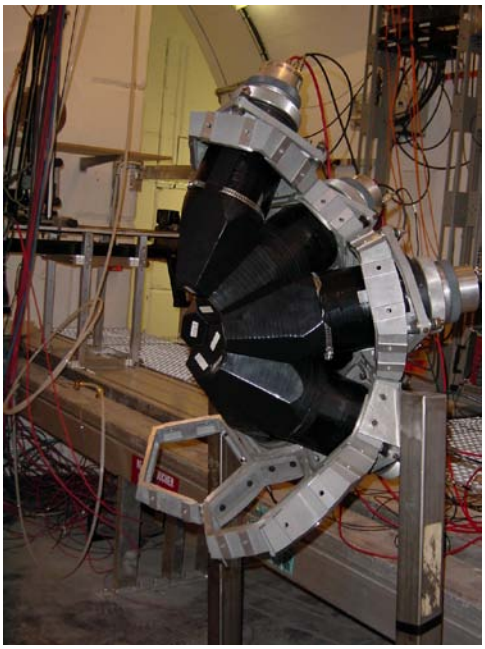

Figure 3.19: A part of the total array of BaF_2. The single crystals are well in evidence.

The essential features of this detector are a good resolution in energy, ranging from 14% at 662 keV to 6% at 6.13 MeV, a good time resolution of 500 psec and a γ-ray efficiency higher than 90% in the energy range below 10 MeV. This means that capture

events can indeed produce a total detected energy close to the neutron binding energy of the sample under investigation. The choice of BaF_2 is based on the fact that it exhibits similar sensitivity to scattered neutrons compared to other high-efficiency scintillators, such as CeF_3 and Bismuth germanate (BGO), but has a better time and energy resolution. A short list of characteristics of some inorganic scintillator is indicated in Table 3.4. Compared to C_6D_6, the main problem in using the 4π calorimeter results from the fact that the chemical composition of the scintillator may include isotopes with relatively large cross-sections for neutron capture; for the same reason, other inorganic scintillators (NaI and CsI) have to be excluded from this application.

Table 3.4: Characteristics of several scintillators.

Scintillator	Density (g/cm^3)	Decay Time (nsec)	Wavelength (nm)	Photons/MeV
BaF_2	4.88	0.6; 630	220; 310	1,800; 10,000
$Bi_4Ge_3O_{12}$	7.13	60; 300	480	700; 7,500
CeF_3	6.16	3; 27	300; 340	200; 4,300
C_6F_6	1.61	3.3	430	10,000

There are various possibilities to cover the full solid angle with an arrangement of closely packed crystal. The final geometry chosen for n_TOF is similar to the one used at FZK, Karlsruhe [58]; it consists of 42 elements, 30 hexagonal and 12 pentagonal crystals, see Figure 3.20. Higher granularity would be preferable for experiments where high counting rates or high multiplicities are expected but this solution requires a more complex geometry and is also more expensive. A calorimeter with higher granularity (162 elements) will be assembled at Los Alamos for the DANCE experiment [59]. The optimization of the detector design and the investigation of the neutron induced background will be performed by means of detailed Monte Carlo simulations. In Appendix I, it is illustrated the original contribution to the R&D of this detector. We have compared the response of two inorganic scintillators, BaF_2 and CeF_3, the possibility of n/γ discrimination, the ability to resolve pile-up events and finally a scheme of data analysis for this kind of detector.

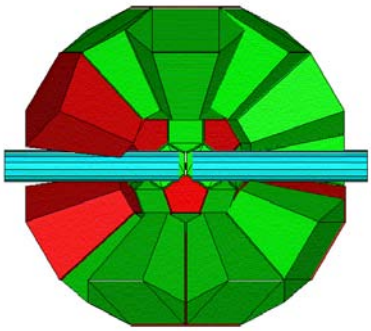

Figure 3.20:Schematic view of the 4π calorimeter in Karlsruhe set-up.

3.8 Detectors for beam profile and background determination

In order to study the characteristics of the neutron beam and of the background in the experimental area, a series of measurements with different kind of detectors have been performed during and after the commissioning phase of the facility. The detectors used for these measurements are essentially: MicroMegas, High purity Germanium detector (HPGD), TLD (ThermoLuminiscence detector), Bicron BC 702 and ^{3}He detector.

MicroMegas is a new gaseous detector based on simple geometry with planar electrodes. It consists of drift electrode, micromesh and an array of strips. Between one electrode and the micromesh there is a conversion gap where radiation liberates ionization electrons. A thin amplification gap exists between the micromesh and the other electrodes, where the multiplication is produced and recorded by the strips. A 5 μm thin grid separated the two regions. The free electrons drift in the amplification gap where printed electrodes of any shape collect the electrons from the avalanche. The detector is filled with a mixture of IsoButhane and Ar or CF_4 at a pressure of around 1 bar. The detector was mounted in an aluminum vacuum chamber (Figure 3.21), with two kapton foils that were used to maintain the pressure inside the detector and separate it from vacuum. The main goal of the MicroMegas is to determine the neutron beam profile at different energies; to this aim an appropriate neutron/charged particle converter must be employed which can be either the filling gas of the detector or a deposited target on its entrance window. Conversion reaction that are usually employed for slow or fast neutron detection are proton recoil, $^{10}B(n,\alpha)$, $^{6}Li(n,\alpha)$ reactions. The proton recoil due to the elastic scattering with a neutron is particular

useful for fast neutrons; in this case, particles are emitted with a flat energy distribution extending from zero to the full neutron energy. The Lithium reaction is particularly useful for slow neutrons and was used in the first n_TOF measurements campaign. In chapter 4, some of the results extracted from the measurements will be shown compared with the simulations.

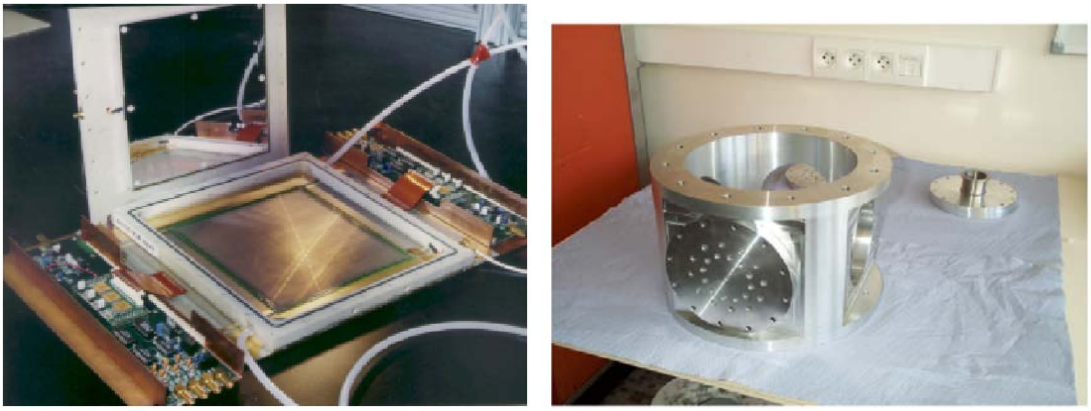

Figure 3.21: Micromegas detector is shown in left panel while the right panel illustrates the vacuum chamber.

The HPGD is a high-resolution Canberra model GR25195-7935.7S γ-spectrometry with the following characteristics: diameter 52.5 mm length 56 mm, relative efficiency 25%, energy resolution 1.95 keV FWHM at 1.33 MeV. The detector was used also for the measurements of γ-ray activation in the experimental area [60].

The ^{3}He detector SP9 Centronix, instead, is used for neutron measurements. It has a spherical shape (30 mm diameter) containing a mixture of ^{3}He (2 atm) and Kr (1atm). The detector was mostly used inside spheres of polyethylene of different diameter, 81 mm and 233 mm, being sensitive to different neutron energies. Measurements with 1 mm thick layer of cadmium covering the 81 mm sphere to cut the thermal neutrons were also performed [40].

Chapter IV

4.1 Introduction

On April 2001, the first measurements began at the n_TOF facility. The main goal of the campaign, which ended at the beginning of November 2001 with only two months interruption, was the experimental validation of the characteristics of the facility. In particular, the measurements were devoted to the accurate determination of the neutron flux, beam profile, energy resolution and background in the experimental area. To verify the accuracy of the experimental cross-section data collected at n_TOF, part of the program was dedicated to measurements of well-known cross-sections, typically considered "standard of measurements". In particular, capture cross-section on ^{197}Au, ^{109}Ag and ^{56}Fe samples were measured with the aim of validating the weighting function technique used with C_6D_6 detector (described in Chapter 3). Beam characteristics at high energy were instead studied by measuring the ^{235,238}U*(n,f)* and ^{209}Bi*(n,f)* reactions with PPAC.

During the first phase of the measurements, an unexpectedly high level of ambient background was observed (the ambient background is the energy spectrum recorded in the detectors with the beam in the experimental area, but without any sample in the beam). The measured background was approximately two orders of magnitude higher than predicted on the basis of the simulations for the design of the facility. Since this level was too high to pursue the foreseen experimental program, an extensive study of the background was undertaken, consisting of dedicated simulations and measurements. This study allowed to isolate the source of background which was associated to muon capture followed by emission of a neutron in the experimental area. The solution to this problem consisted in the addition of a 3 meters thick iron wall before the experimental area, for muon attenuation.

The following paragraphs present a description and the results of the first measurement campaign at n_TOF, carried out at CERN with the aim of characterizing the neutron beam.

4.2 Neutron flux determination

The measurement of the neutron flux was performed with several detection systems. We concentrate here on the analysis of the Silicon Flux Monitor Detector. Details on the geometry, electronics and simulations for this system are described in the previous chapter. Figure 4.1 shows the two-dimensional plot of the energy deposited in the Silicon detectors as a function of the neutron energy (reconstructed from the time-of-flight). The energy deposited was calibrated by considering that the amplitude of the triton peak for low neutron energies corresponds to 2.5 MeV. Other information available from the recorded data, such as the baseline, its variance, the area in the rising part of the signal, etc, were useful to discriminate the noise from alpha and triton particle events in the spectra. Since part of the alpha spectrum was below the threshold, it was decided to perform the analysis only on the tritons. Therefore, a banana gate was applied to select the triton region in Figure 4.1. It should be noted that because of the presence of a strong γ-flash, useful data extend only up to 700 keV, although a better reconstruction routine, currently being implemented, is expected to allow to better discriminate signals from the tail of the γ-flash at higher energy.

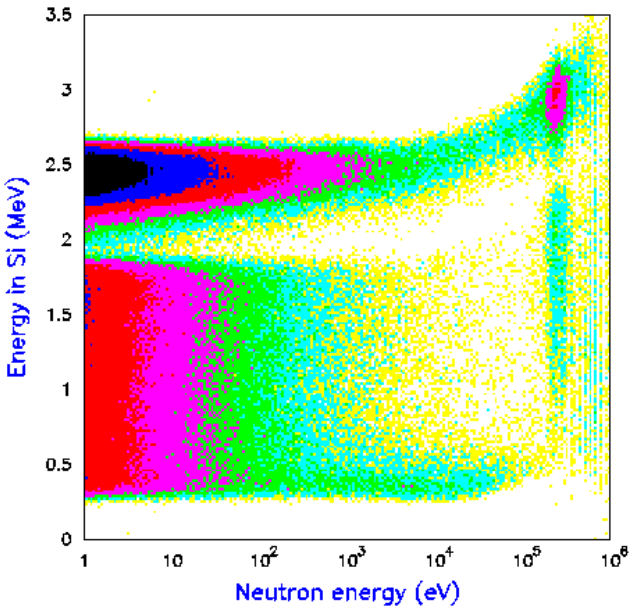

Figure 4.1: Energy deposited in Si detectors as a function of the reconstructed neutron energy. The two loci, corresponding to tritons and alpha particles, are well separated.

The following expression was used to extract the integrated iso-lethargic neutron flux from the data:

$$\frac{dn}{d\ln E} = \frac{dN_{Si}}{d\ln E} \cdot \frac{1}{Y(E)\cdot\varepsilon}.$$

In the formula, E represents the energy reconstructed from the time-of-flight $dN_{Si}/dlnE$ is the spectrum of detected events in the Silicon monitor normalized to 7×10^{12} protons (nominal proton bunch), $Y(E)$ is the capture yield of the ^{6}Li$(n,\alpha)^{3}$H reaction and ε is the geometric efficiency. Since the ^{6}LiF deposit intercepts the whole beam, no correction for the beam profile has to be applied. It should be noted that the iso-lethargic flux, defined as the derivative of the flux with respect to the natural logarithm of the energy, results independent from the choice of the energy binning and is particularly useful to represent the flux in a wide energy spectrum, extending over several orders of magnitude.

While the evaluation of the capture yield is straightforward, the estimate of the geometric efficiency requires some more consideration, since the Silicon detectors ensure only a partial coverage of the emission solid angle and the angular distribution of the emitted tritons exhibits a strong anisotropy for neutron energies above 10 keV. The geometric efficiency was estimated by means of simulations with GEANT-4, with a detailed software replica of the apparatus. Tritons were generated according to the angular distribution from the ENDF B-VI file [35], shown in Figure 4.2, transformed in the Laboratory system. The resulting efficiency is shown in Figure 4.3.

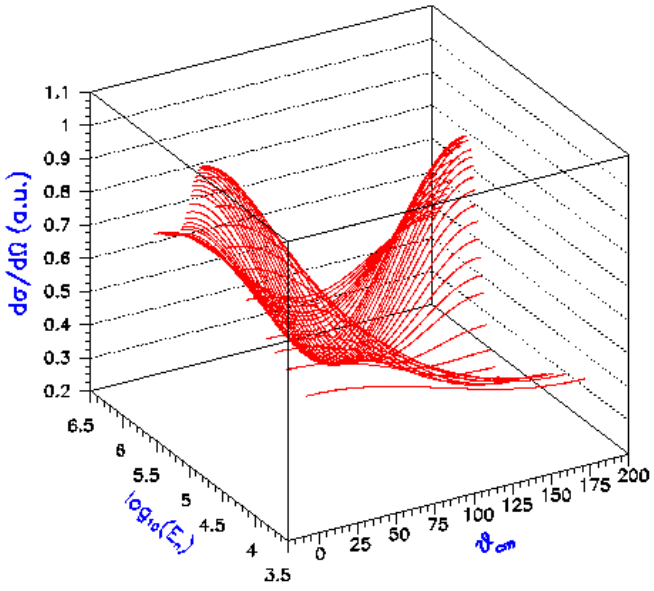

Figure 4.2: The angular distribution of emitted tritons in ^{6}Li$(n,t)^{4}$H reaction is shown in the function of the neutron energy.

The reconstructed isolethargic integrated neutron flux, normalized to the nominal PS proton bunch of 7×10^{12} protons, is shown by the green histogram in Figure 4.4. In the same

figure the isoflux determined with other detectors, such as the fission chambers, parallel plates avalanche counter and C_6D_6, is shown (a discussion on this other results is given at the end of the paragraph).

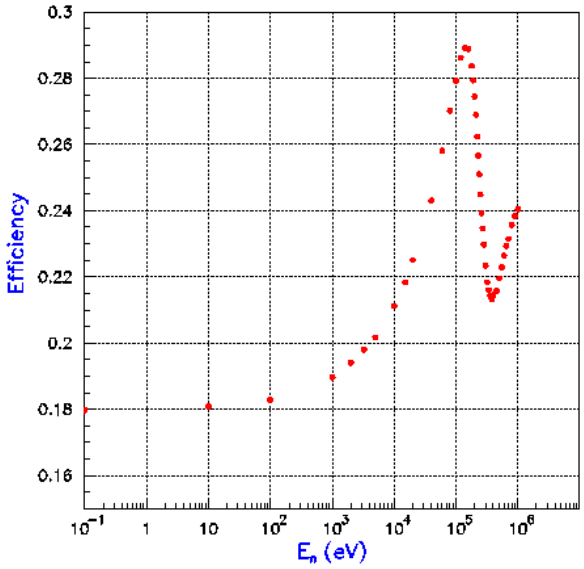

Figure 4.3: The panel shows the geometric efficiency, as obtained from simulations of the Silicon Monitor.

Several systematic uncertainties could affect both the absolute normalization and the shape of neutron flux. The most important ones are associated with the evaluation of the total number of protons in the measurement, the thickness and uniformity of the ^{6}LiF deposit and the geometric efficiency. The different sources of systematic uncertainties are discussed hereafter:

Number of protons used in the normalization. A comparison of several runs showed that non-statistical fluctuations of up to 5% are observed in the ratio between the number of events in the Monitor and the number of protons recorded in the run. Probably, such fluctuations are associated to a loss of information on the number of protons for some bunches. Although some corrective actions can be used, such as to reject the events for bunches without proton information, the problem can result in an uncertainty of the order of a few percent in the absolute value of the flux.

Thickness and uniformity of the ^{6}LiF deposit. The target laboratory of the "Laboratori Nazionali di Legnaro" (LNL), were the foils with ^{6}LiF deposit were prepared, certifies that the total mass of the deposit is accurate in within few percent. However, a larger uncertainty of up to 10% could exist on the uniformity. If the neutron beam had a flat profile, the non-uniformity of the deposit would have no effect on the measured flux. As shown later, however, the beam has a gaussian profile, so that an uncertainty on the

absolute value of the flux has to be expected, of the same magnitude of the disuniformity. The effect on the shape of the isolethargic flux is negligible, considering that the beam profile does not change dramatically with the neutron energy.

Geometric efficiency. A detailed replica of the apparatus was implemented in the simulations. However, small differences between the real and simulated setup cannot be excluded. In particular, the foil-Si distance and the angle of the Si detector may in reality be slightly different than the simulated ones. A test was performed by changing some parameters in the simulations, and under realistic assumptions, the observed effect was of a few percent both on the absolute scaling of the flux and on the shape, with the region above 100 keV of reconstructed neutron energy more sensitive to differences in geometrical details.

A combination of the effects discussed above leads to an estimated uncertainty of the order of 10% in the absolute normalization, with the shape of the flux also slightly affected, in particular above 10 keV. Nevertheless, the results here shown demonstrate the reliability of the apparatus as flux Monitor device, particularly useful in capture cross-section measurements for relative normalization.

A more precise determination of the neutron flux at n_TOF, extending up to several hundreds of MeV, was obtained during the commissioning of the facility with a calibrated fission chamber from Physikalisch-Technische Bundesanstalt (PTB), Braunschweig, Germany [60], using the ^{235,238}U*(n,f)* and ^{209}Bi*(n,f)*. The red curve in Figure 4.4 shows the results obtained with this detector. A similar flux was also measured with the PPAC, and with the activation technique at some specific energy (in particular at the 4.9 eV resonance of a Au activation foil). Considering the relative uncertainties, all measurements agree with each other. When compared with the flux expected on the basis of the simulation, represented by the black curve in the Figure 4.4, the measured neutron flux is systematically lower than predicted, by approximately 20%. Probably this discrepancy is due to a slight misalignment of the last collimator or to some other effect not included in the simulations.

Since the most accurate measurement is the one performed with the calibrated PTB chamber, it is considered in the analysis as the effective neutron flux in the experimental area.

For simplicity, the measured neutron flux has been parameterized by two 4th degree polynomials as a function of the $log_{10}E$ from 1 eV to 10 keV and from 10 keV to 1 MeV. The parameters are indicated in Table 4.1. Although a more accurate number for the flux is

obtained for each measurement form the ^{197}Au(n,γ) reaction or from ^{235}U(n,f) reaction, the parameterized values represent a convenient first assumption of the neutron flux in the analysis.

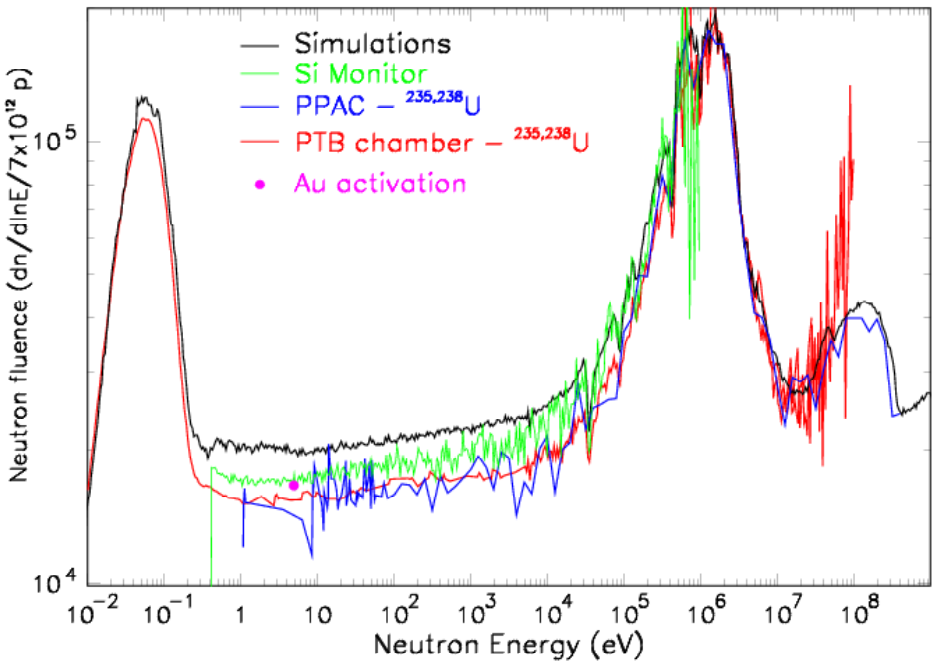

Figure 4.4: Compilation of different determination of the flux at n_TOF.

Table 4.1: Coefficients of the 4th degree polynomial fitting the isoflux.

Energy range	p_0	p_1	p_2	p_3	P_4
0.1eV-31.62keV	15628.0	-1552.1	2653.7	-1067.8	140.47
31.62keV-1.MeV	$1.087\cdot10^7$	$-9.425\cdot10^5$	$3.078\cdot10^6$	$-4.486\cdot10^5$	24675

4.3 Analysis of capture data with C_6D_6

The first measurements of capture cross-sections at n_TOF were performed with two C_6D_6 liquid scintillator detectors (deuterated benzene) from Bicron (see previous chapter for details). The detectors were placed symmetrically with respect to the neutron beam direction and at 4.5 cm from the center of the sample, as shown in the Figure 4.5. The aim

of the measurements was to verify the accuracy of the Pulse Height Weighting Function technique and, ultimately, to estimate the precision of the extracted cross-sections. To this end, several samples with well-known cross-sections were measured: ^{197}Au, ^{109}Ag and ^{56}Fe. For each sample, the corresponding Weighting Functions were calculated and capture yield were extracted. The accuracy of the measured cross-section from n_TOF was estimated by comparing the results with the known cross-sections, tabulated in the databases.

The following paragraphs contain a detailed description of the method and the results on the Weighting Function validation. A cross-check of the neutron flux was also obtained with this analysis.

4.3.1 Determination of the weighting function

In order to extract the weighting function, the γ-ray response of the detector was calculated by means of Monte Carlo simulations. To this end the experimental apparatus was reproduced in two codes (GEANT-3.21 and GEANT-4). The most important geometrical and material details have been included in the simulations. Particular attention has been devoted to include a description as realistic as possible of the C_6D_6 detectors and of the sample changer.

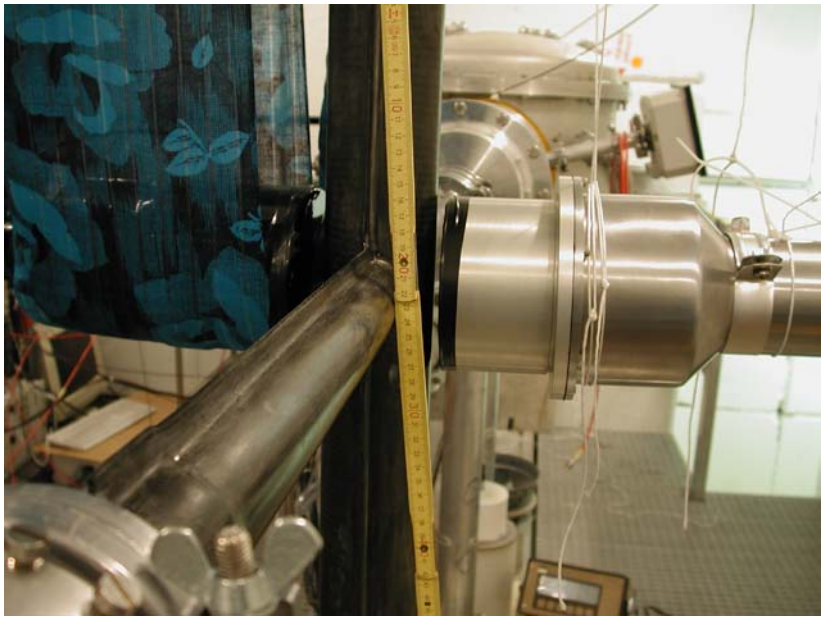

Figure 4.5: Set-up of Bicron C_6D_6 for the determination of the Weighting Function.

In fact, it is important to include in the simulations all details of the experimental apparatus, both in terms of geometry and materials, since every part can absorb or scatter the γ-rays and constitute a source of secondary radiation, modifying in appreciable way the detector response. Figure 4.5 shows the set-up for the Bicron C_6D_6 while Figure 4.6 illustrates the detailed geometry simulated with GEANT-4.

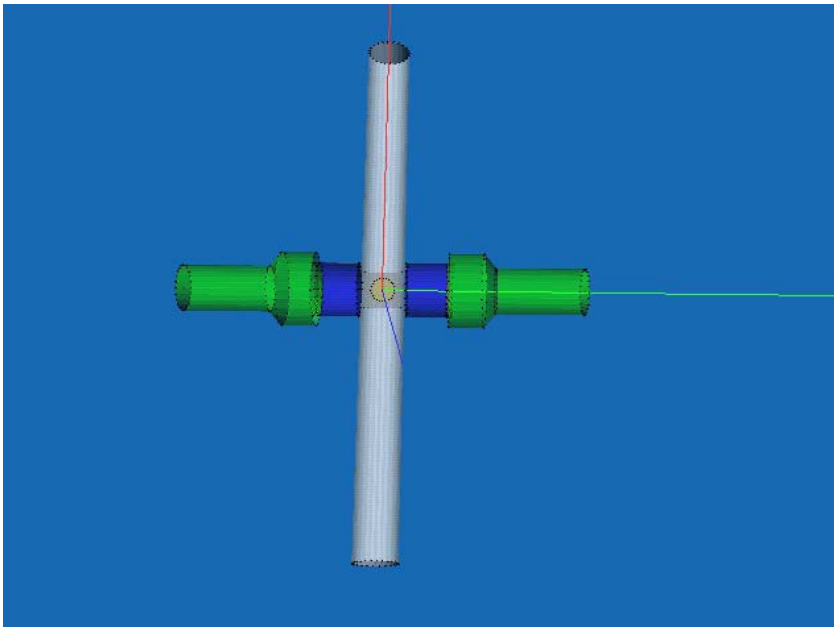

Figure 4.6: Detailed geometry simulated with GEANT-4.

A set of simulations was performed for the samples under study: ^{197}Au (4.5 cm diameter × 0.01 cm thickness), ^{107}Ag (2. cm diameter × 0.02 cm thickness) and ^{56}Fe (4.5 cm diameter × 0.05 cm thickness). According to previous publications on the subject [36], the following energies of primary γ-rays were generated in the simulations: 1.266, 2.209, 3.163, 4.386, 5.515, 6.183, 7.383 and 8.392 MeV, which correspond to the energies involved in the experimental measurements of the weighting function performed by Corvi et al. [37].

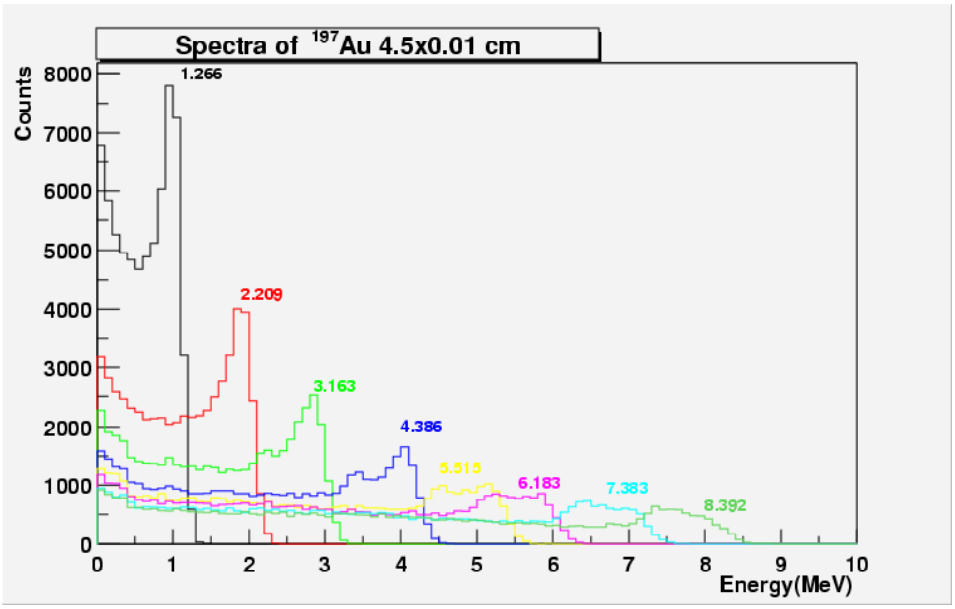

Figure 4.7: Simulated response function in C_6D_6 detectors for ^{197}Au sample.

For a realistic calculation of the C_6D_6 response functions, the simulated energy deposited in the liquid scintillator volume was convoluted with the detector resolution. This was estimated by analyzing the calibration runs performed with the γ-ray sources ^{137}Cs and ^{60}Co. The variance for the gaussian resolution was found to depend on the deposited energy according to the following relation: $\sigma^2(E) = 3.8 \cdot E$ where E is expressed in keV. Figures 4.7, 4.8 and 4.9 show the simulated distributions, convoluted with the resolution of the detector for all samples and for the set of primary γ-rays indicated above. As expected, the shapes of the response function for the three samples are quite similar. The main differences are observed for low energy deposited and at low γ-ray energy, due to the larger influence of the atomic charge and dimensions of the sample. In the minimization procedure, used to obtain the parameters of the weighting functions (described in Chapter 3), a threshold of 100 keV in the simulated spectra is applied, to account for the acquisition threshold used on C_6D_6 signals during the measurement. In this way, no correction is later required for the missing portion of the detector response spectrum. The values of the efficiencies with and without the threshold are indicated in Table 4.2.

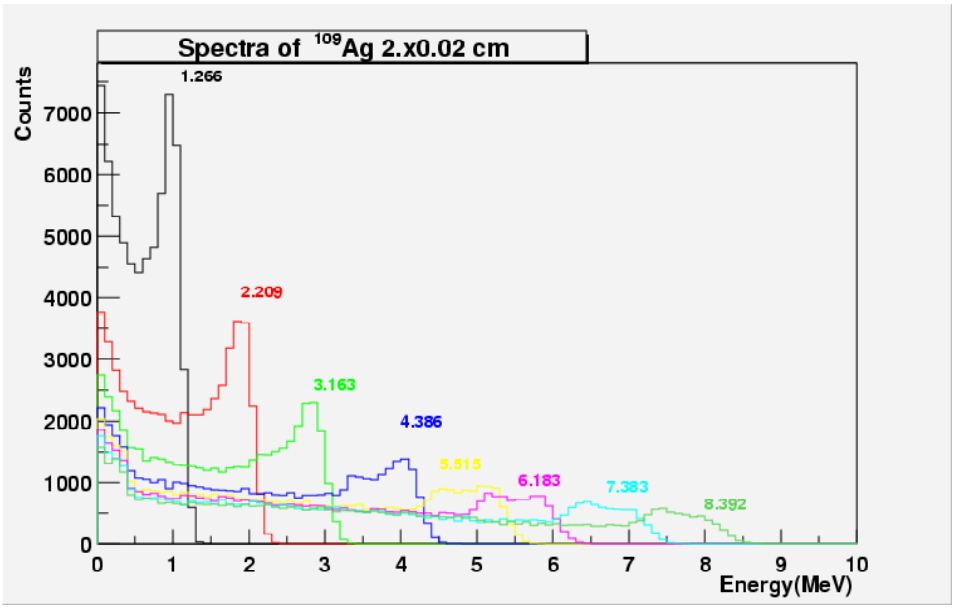

Figure 4.8: Simulated response function in C_6D_6 detectors for ^{109}Ag sample.

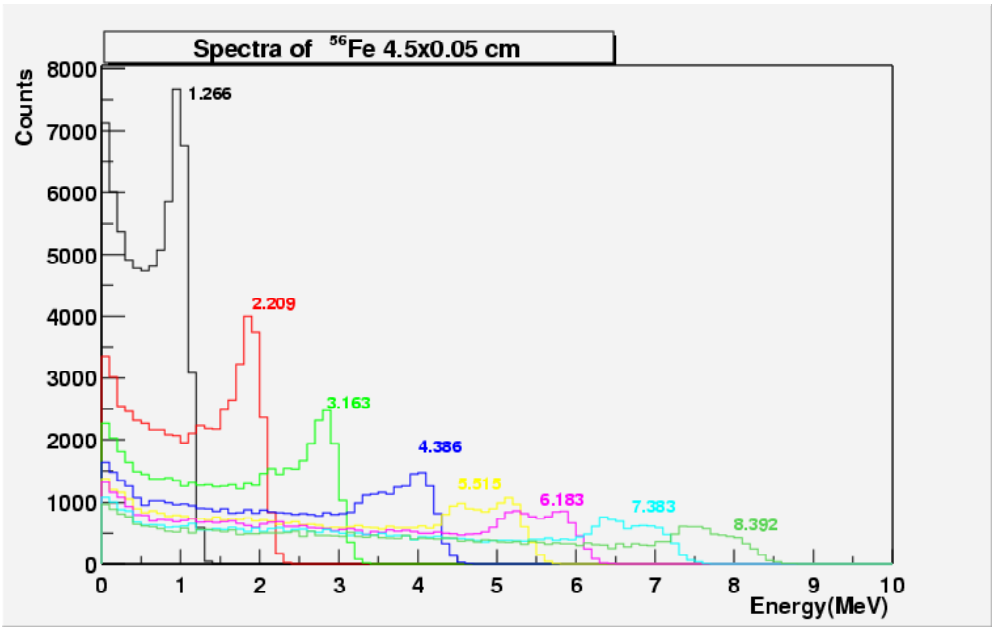

Figure 4.9: Simulated response function in C_6D_6 detectors for ^{56}Fe sample.

To extract the parameters with relative errors using Equation 3.2, the variance of the detector response function σ_R has to be defined (note that this should not be confused with the energy resolution of the detector $\sigma(E)$, but it represents the uncertainty associated to each bin of the simulated response distribution). Two sets of parameters of the Weighting Function have been extracted for each sample with the minimization procedure. The first one is extracted by fixing the value of σ_R to 1 for all bins of deposited energy; the second

set is obtained using the errors according to the Poisson distribution. The two sets of values are indicated in the Table 4.3, with the relative weighting functions shown in Figures 4.10, 4.11, 4.12.

Table 4.2: Simulated efficiencies for the different samples with and without a cut on the energy deposited in the detector (200 keV).

□□γ-ENERGIES(MEV) SAMPLES		1.266	2.209	3.163	4.386	5.515	6.183	7.383	8.392
^{197}Au	No cut	6.07%	5.48%	4.90%	4.43%	4.19%	4.13%	3.99%	3.96%
	Cut	6.05%	5.16%	4.67%	4.27%	4.06%	4.01%	3.90%	3.87%
^{107}Ag	No cut	6.50%	5.43%	4.90%	4.52%	4.43%	4.38%	4.40%	4.42%
	Cut	6.00%	5.10%	4.61%	4.18%	3.97%	3.87%	3.68%	3.58%
^{56}Fe	No cut	6.67%	5.46%	4.82%	4.40%	4.20%	4.10%	3.94%	3.84%
	Cut	5.96%	5.12%	4.60%	4.24%	4.05%	3.97%	3.83%	3.74%

The parameter errors, determined by normalizing the value of the reduced χ^2 to 1, are comprised between the 0.01% and 10%. It is important to note that the weighting functions obtained with the two different assumptions for σ_R are not significantly different. Only the weighting function of the Au at high energies (above 9 MeV) shows appreciable differences, while no difference is observed for the other two samples. In Table 4.4, the elements of the correlation matrix are also indicated. The matrix provides information on the goodness of 4th degree polynomial assumption for *W(E)*. For all samples studied, the off-diagonal elements are in general close to one, which demonstrates that the number of the parameters is redundant, thus providing confidence on the correctness of the assumption.

Table 4.3: Parameter of the weighting functions.

Paramenters sample		a_0	a_1	a_2	a_3	a_4
^{197}Au	σ=1	-0.058	29.143	3.968	0.930	-0.113
	$\sigma_{Poisson}$	-3.638	38.217	-1.552	2.085	-0.189
^{107}Ag	σ=1	-2.454	35.077	0.677	1.513	-0.132
	$\sigma_{Poisson}$	-2.765	35.768	0.343	1.561	-0.132
^{56}Fe	σ=1	2.803	21.516	10.25	-0.733	0.024
	$\sigma_{Poisson}$	0.520	27.266	6.822	-0.035	-0.020

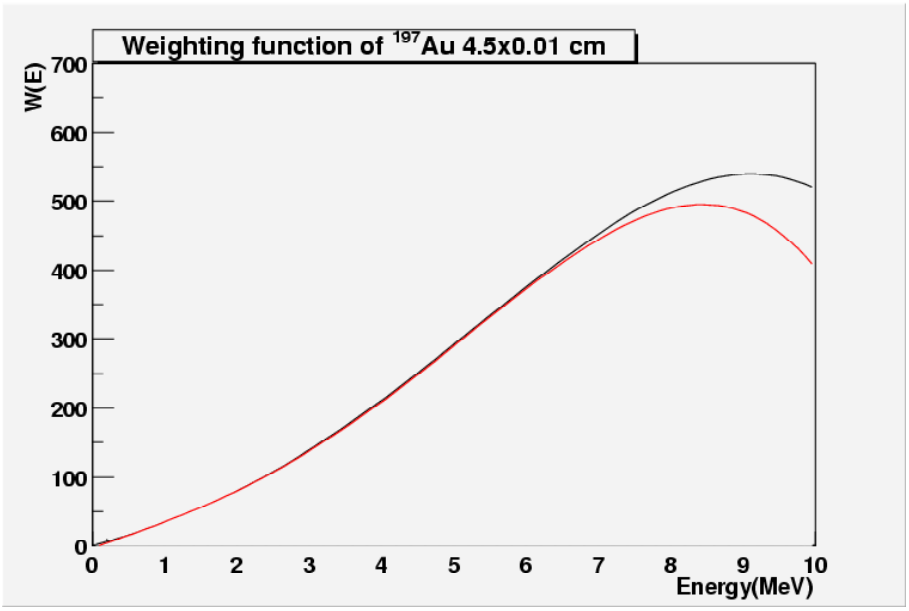

Figure 4.10: Weighting Function of the ^{197}Au sample.

Table 4.4: Correlation matrices respectively for: ^{197}Au, ^{107}Ag and ^{56}Fe.

^{197}Au	1.	-0.983	0.950	-0.912	0.876
	-0.983	1.	-0.989	0.965	-0.937
	0.950	-0.989	1.	-0.993	0.997
	-0.912	0.965	-0.993	1.	0.995
	0.876	-0.937	0.997	-0.995	1.
^{107}Ag	1.	-0.984	0.951	-0.914	0.880
	-0.984	1.	-0.989	0.965	-0.939
	0.951	-0.989	1.	-0.993	0.978
	-0.914	0.965	-0.993	1.	-0.995
	0.880	-0.939	0.978	-0.995	1.
^{56}Fe	1.	-0.983	0.950	-0.913	0.887
	-0.983	1.	-0.989	0.965	-0.938
	0.950	-0.989	1.	-0.993	0.997
	-0.913	0.965	-0.993	1.	-0.995
	0.817	-0.937	0.977	-0.995	1.

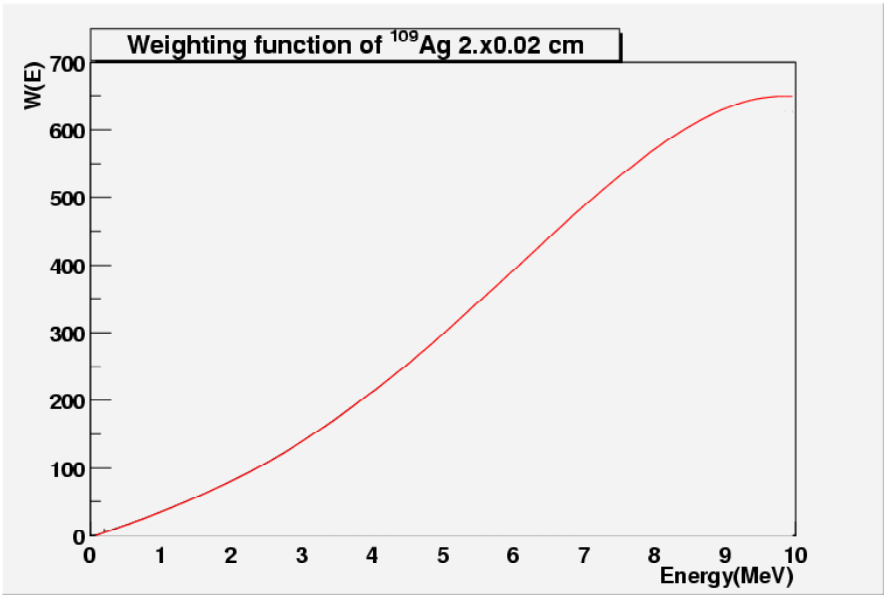

Figure 4.11: Weighting Function of the ^{107}Ag sample.

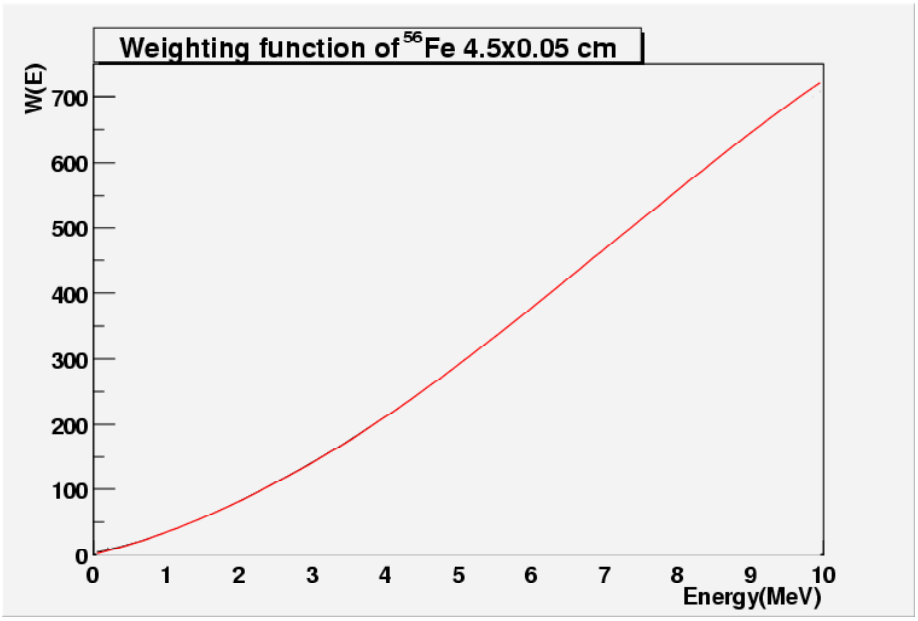

Figure 4.12: Weighting function of the ^{56}Fe sample

4.3.2 Capture Yield

In the measurement of capture cross-sections, the experimental quantity that has to be determined is the capture yield *Y(E)*, that is the probability that a neutron of energy *E* undergoes a capture reaction in the sample. This quantity is linked to the total cross-sections σ_t and to the capture cross-section σ_γ by the following expression:

$$Y(E) = \left(1 - e^{-n\sigma_T(E)}\right) \cdot \frac{\sigma_\gamma(E)}{\sigma_t(E)} \tag{4.1}$$

where *n* is the number of atoms per barn in the sample.

For the determination of the capture yield, several steps have been followed. The raw data collected with the FADC, in this case the total area of the C_6D_6 signal, have been calibrated in energy (in keV), by means of two γ-ray sources: ^{137}Cs (0.662 MeV) and ^{60}Co (1.173 and 1.333 MeV). For the measurement here considered, a fit with a first order polynomial gives an offset of 8.4 keV and a slope of 6.45 keV/channel. The experimental response function *R(E)* of the detector, obtained after the calibration, can then be convoluted with the weighting function *W(E)* to obtained the weighted energy spectrum. This spectrum, integrated over a given neutron energy range *ΔE* (typically the area of a resonance), is linked to the capture yield *Y(E)* and to the neutron flux by the following relation:

$$\sum_i R_i W_i = E_{binding} \cdot \int_{\Delta E} \Phi(E) \cdot Y(E) dE \,. \tag{4.2}$$

Here, R_i is the measured count rate in the detectors for the i^{th} bin of energy deposited (in other words, the discrete energy spectrum) and W_i the corresponding weight, $\Phi(E)$ is the neutron flux integrated over the sample area and $E_{binding}$ the total energy of the cascade (or capture energy) [38]. Equation 4.2 is derived from the definition of the weighting functions, discussed in Chapter 3.

The measured weighted spectrum can be used to check the accuracy of the Weighting Functions, if the neutron flux is already known with good accuracy and a reliable theoretical value for the capture yield is available. This is the case of "standard" isotopes like Au, in which cross-sections are known, so that *Y(E)* is simply obtained from Equation 4.1. On the other hand, if one assumes that the Weighting Function is correct, it is possible to extract the neutron flux, in case this is still unknown, by inverting Equation 4.2. In the present case, the use of different samples allowed to obtain information both on the validity of the weighting function and on the neutron flux at different energies, corresponding to some particular resonances.

Before discussing the results, few considerations have to be made on the intrinsic uncertainties on the application of the weighting function technique to the measurements of capture reactions. Some uncertainty in the reconstruction may derive from two processes that are not considered in the weighting functions determination: the detection of two or more photons produced in the same de-excitation γ-ray cascade (following neutron capture)

and the loss of photons of a cascade due to internal electron conversion process. Both effects, however, are characterized by low probability, given the small solid angle covered by the detectors and the low multiplicity of the cascade (typically 3 γ-rays are emitted in average in a capture reaction). Therefore, as also suggested by the simulations, such effects can be neglected as they contribute to an uncertainty of less than 1%. The main source of uncertainty, instead, could be associated with the adequacy of the minimization procedure and, most importantly, the reliability of the simulations of the detector response. These effects can only be checked by comparison of the cross-sections extracted at n_TOF for a number of "standard" isotopes with the known cross-sections, available from the Evaluated Nuclear Data Files [37].

Figures 4.13, 4.14 and 4.15 show the measured capture yield for three well-known isotopes: Au, Ag and Fe. The main resonances of such isotopes were analyzed in order to validate the weighting function technique, verify the neutron flux at the corresponding energy and, finally, provide confidence on the quality and accuracy of the cross-sections extracted at n_TOF.

The procedure described above was applied to the saturated resonance at 4.9 eV of ^{197}Au(n,γ) reaction ($E_{binding}$ = 6.5 MeV), to the saturated resonance at 5.2 eV in the ^{109}Ag(n,γ) reaction, ($E_{binding}$ = 6.88 MeV) and to the ^{56}Fe(n,γ) resonance at 1.15 keV ($E_{binding}$ = 7.64 MeV). We have calculated the neutron flux at those energies, in the assumption that the Weighting Functions are correct. In all cases, the Silicon Flux Monitors was used for normalization to the neutron flux. In the case of Ag, the sample has a diameter of 2 cm and therefore it is necessary to apply a correction factor for the missing part of the beam, since the sample is smaller than the beam profile. The neutron flux intercepting the sample was estimated from the simulations to be 58 % of the total flux. The results for all samples are listed in Table 4.5, under the column $\Phi_{binding}$.

Table 4.5: Parameters used in SAMMY and extracted IsoFlux. The different parameters are defined in the text.

	α	β	ω	$\Phi_{binding}$	Φ_{sammy}
^{197}Au	$9.80\ 10^{-5}$	$9.83\ 10^{-4}$	$3.19\ 10^{-7}$	$1.6839\ 10^{4}$	$1.6040\ 10^{4}$
^{109}Ag	$9.05\ 10^{-5}$	$1.15\ 10^{-4}$	$3.22\ 10^{-7}$	$1.6875\ 10^{4}$	$1.6000\ 10^{4}$
^{56}Fe	$7.90\ 10^{-4}$	$3.34\ 10^{-4}$	$3.13\ 10^{-6}$	$2.0460\ 10^{4}$	$2.0150\ 10^{4}$

A more accurate analysis of the flux is obtained by fitting the resonance with the code SAMMY version 6-beta [39]. A brief description of the code is given in Appendix II. In brief, the code is typically used in the determination of neutron cross-section, in particular

in the resolved resonance region. The use of a resonance formalism (*R*-matrix analysis) allows to extract the resonance parameters, that is the energy, total and partial width of the resonances, etc…, by a best fit to the experimental data. The level of the background present in the data and the absolute normalization of the data can also be kept as free parameters. In the present analysis of the Au, Ag and Fe capture cross-sections, the initial guess of the resonance parameters, needed as input in SAMMY, were extracted from the database ENDF/B-VI File 2. The main Au and Ag resonances were analysed in the Multi Level Breit-Wigner (MLBW) approximation, while for the Fe sample the Reich-Moore approximation was used. The resolution function used in the fit was assumed to be a Gaussian, with the width correlated to the time resolution of the proton burst (6 ns) and to the time uncertainty of the moderation process. The Doppler broadening was also included in the fit. At low energy, this represents the major effect that determines the resonance broadening, while above 1 keV the energy resolution of the neutron beam becomes the dominant effect. The background in the experimental data was represented by two contributions. The first one was assumed to be constant (α) in energy while for the second contribution an exponential trend was used: $\beta \cdot exp\left(-\omega\sqrt{E}\right)$. The parameters α, β and ω were treated as free parameters in the fit, together with the normalization constant. For all samples, the single scattering approximation was used, which relies on the assumption that the neutron undergoes at most one scattering inside the sample before being captured. A more complicated multi-scattering approximation was not judged necessary, given the small thickness of the samples used in the measurements.

The results of the fitting procedure are shown in Figures 4.13, 4.14, 4.15. Some indications can be obtained by the analysis of the normalization constant. The results on the extracted flux are reported in Table 4 under the column Φ_{Sammy}. They show an overall good agreement with the flux estimated by means of Equation (2), and is close to the one obtained from the PTB chamber and the Si monitor detector (see Figure 4.4). This result confirms the correctness of the measured flux.

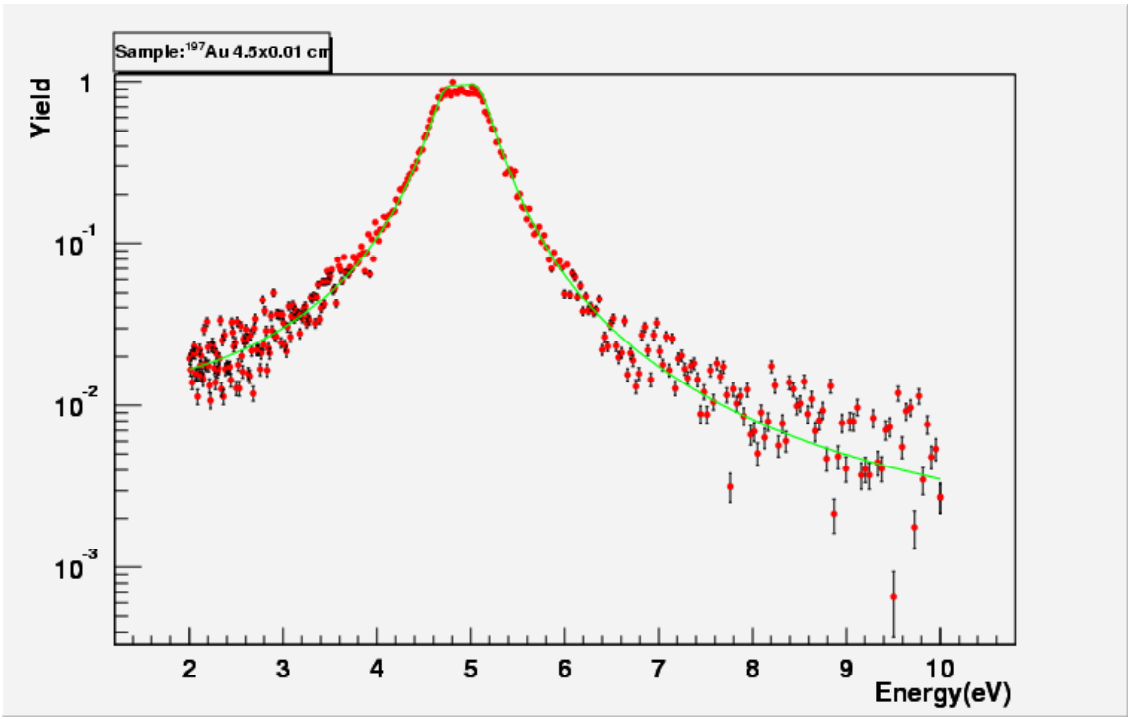

Figure 4.13: Fit of the ^{197}Au 4.9 eV resonance with SAMMY code.

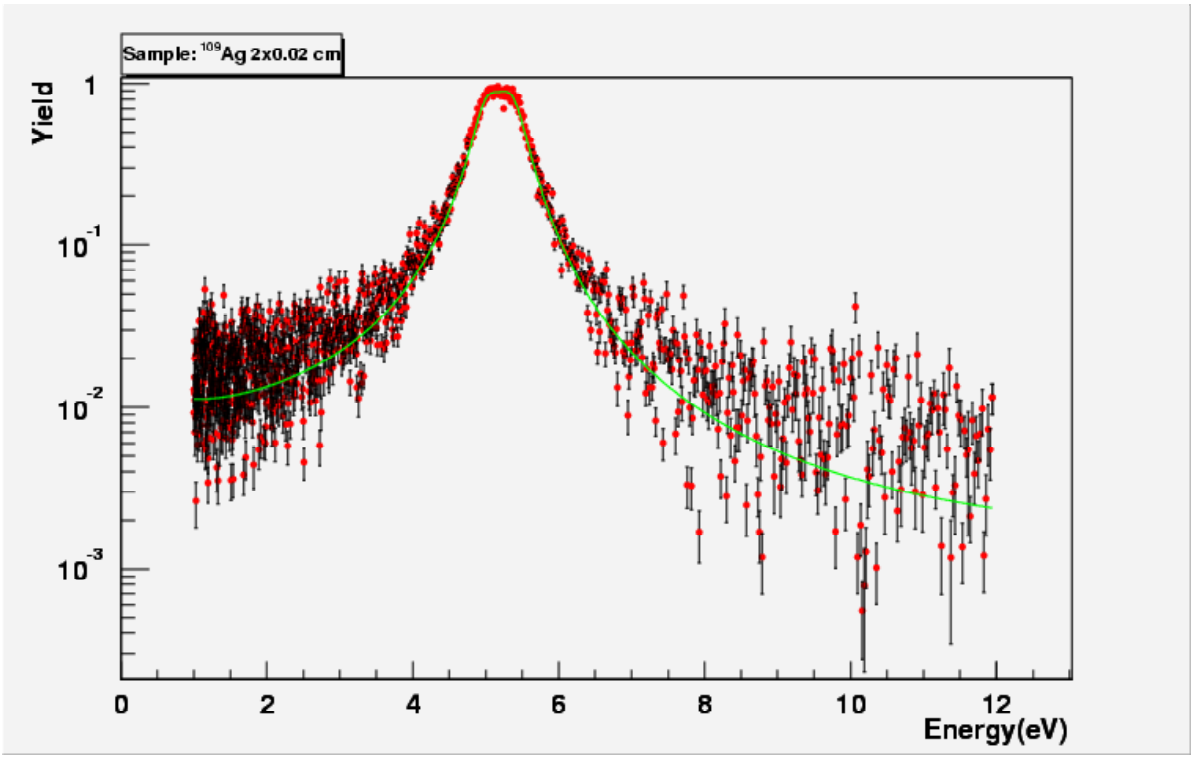

Figure 4.14: Fitting of the ^{109}Ag 5.2eV resonance with SAMMY code.

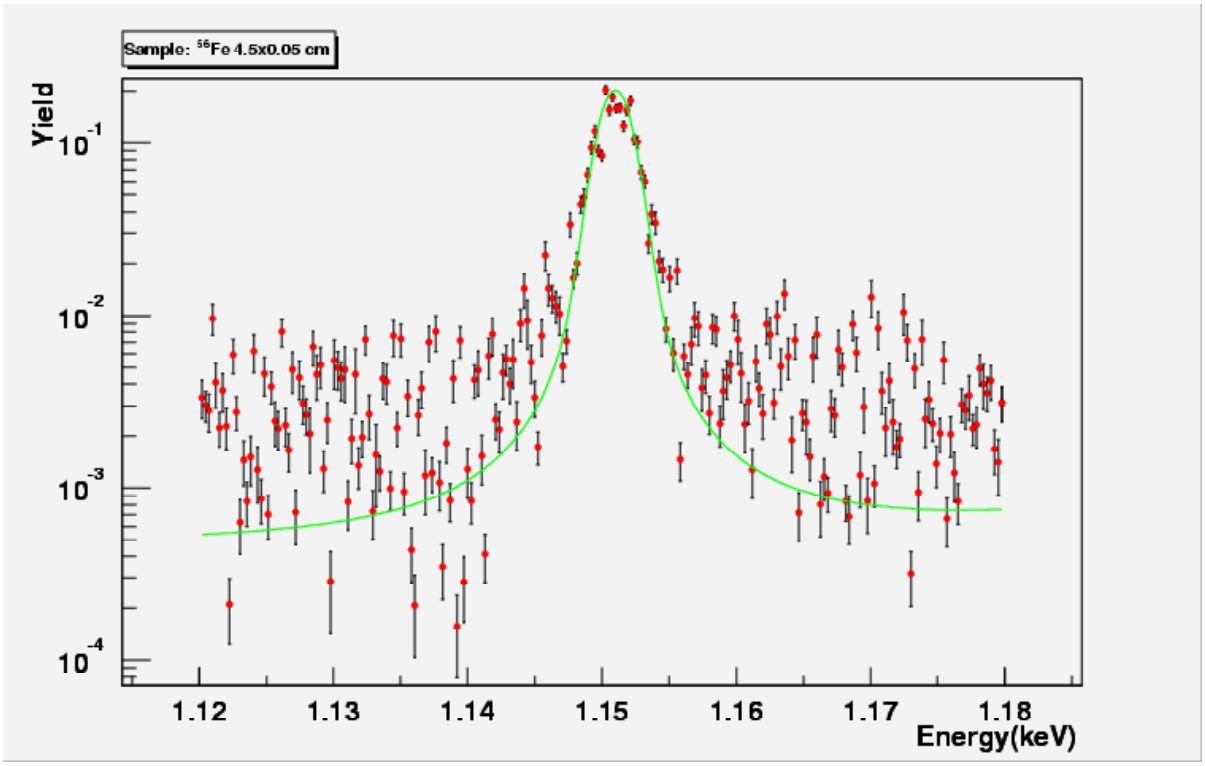

Figure 4.15: Fitting of the ^{56}Fe 1.15 keV resonance with SAMMY code.

4.4 Background

As in all neutron time-of-flight facilities, particular care has to be taken in understanding the different sources of background. For capture reactions, different contributions can affect the capture cross-section measurements. In general, they can be classified as:

Ambient or empty-sample background: this is the background observed in the detectors when the neutron beam is present in the experimental area but no sample is inserted in the beam. It is due to environmental background, such as cosmic rays, natural radioactivity, decay of neutron activated material, neutrons or other particles leaking through the shielding of the experimental area, etc…

Sample-induced neutron background: when a sample is inserted in the beam, neutrons can be scattered, by means of elastic or inelastic reactions, outside the neutron beam direction. They can then undergo different reactions either in the detectors or in the walls and other material present in the experimental area. As a consequence, they can be detected or produce γ-rays (for example after being captured) that can be detected in the apparatus.

In-beam γ-rays background: γ-rays of various origins (from the spallation process, from neutron moderation, etc…) are present in the neutron beam. When a sample is inserted, they can be scattered into the detectors, mainly by Compton and pair production processes, giving rise to a background event.

With the aim of characterizing the background at n_TOF in all its components, a large effort was devoted in the first measurement campaign, with dedicated measurements [40] and simulations [41]. In following sections, the results on the background characterization are presented and discussed, together with the actions taken to reduce the background to a level up to one order of magnitude smaller than other existing facilities.

4.4.1 The ambient background

The first measurement campaign, performed at n_TOF with the aim of characterizing the new neutron beam, provided important information on the background in the experimental area. An unexpectedly high level was immediately observed for the so-called "ambient" or "empty-sample" background that is the count rate observed in the detectors when the beam was crossing the experimental area without any sample target in the beam position. The most important features of this background were:

- A strong asymmetry, with a higher background on one side of the experimental area relative to the beam direction;
- The presence of two components: a fast one, traveling with the speed of light (also called γ-flash) and a slow component coming at later times and up to 15 msec.

It was further estimated that the observed level was one or two orders of magnitude higher than expected from the design of the facility and therefore it constituted by large the dominant contribution of the background affecting the measurement of capture cross-sections. Other contributions such as the sample-induced neutron and in-beam photons background, were in fact much smaller than the "empty-sample" background since little difference was observed when different samples (in particular C and Pb) were inserted in the beam.

Dedicated measurements and simulations allowed to associate this strong background to muons produced by the proton beam in the spallation target where they originate mainly from the decay of pions and kaons. In particular, the fast component observed in the detectors was recognized as produced by high energy muons crossing all concrete

shieldings, which were inadequate on one side of the n_TOF beam tube, thus explaining the observed asymmetry (on the other side the tube runs close to the walls of the tunnel, which act as a much thicker shielding). The slow component, instead, was finally associated with neutrons and subsequent γ-rays from their interaction, produced after muon capture in the walls of the experimental area. After collecting sufficient experimental evidences supporting this hypothesis (described below), an iron wall 3 meters thick was mounted before the experimental area, to attenuate the muon flux.

The experimental program for identifying and curing the background was divided into three steps.

A first phase of measurements was performed to characterize the background in the experimental hall and to test the different hypotheses on the origin of the background. The detectors used for this goal were: ^{3}He counters for neutrons, two Bicron C_6D_6 for γ-rays and one Hyper Pure Germanium Detectors for activation measurements. Measurements were performed with the detectors placed in different positions. To understand whether the background was due to the neutron beam or to particles traveling outside the beam, tests were made with an additional barytic concrete wall outside the beam and, alternatively, by blocking the neutron beam 100 m before the experimental area with a 1.1 m long “shadow bar” (or beam stopper) inserted in the hole of the first collimator.

The experimental evidence indicated that the background was primarily caused by high-energy particles traveling outside the neutron beam; therefore an intervention in the n_TOF tunnel was made to install a 3.2 meters thick iron wall between the magnet and the second collimator (Figure 4.16). Furthermore, to reduce the background related to air activation around the collimators, the experimental area was sealed with plastic foils. Finally, new measurements were made to estimate the background reduction in the experimental hall.

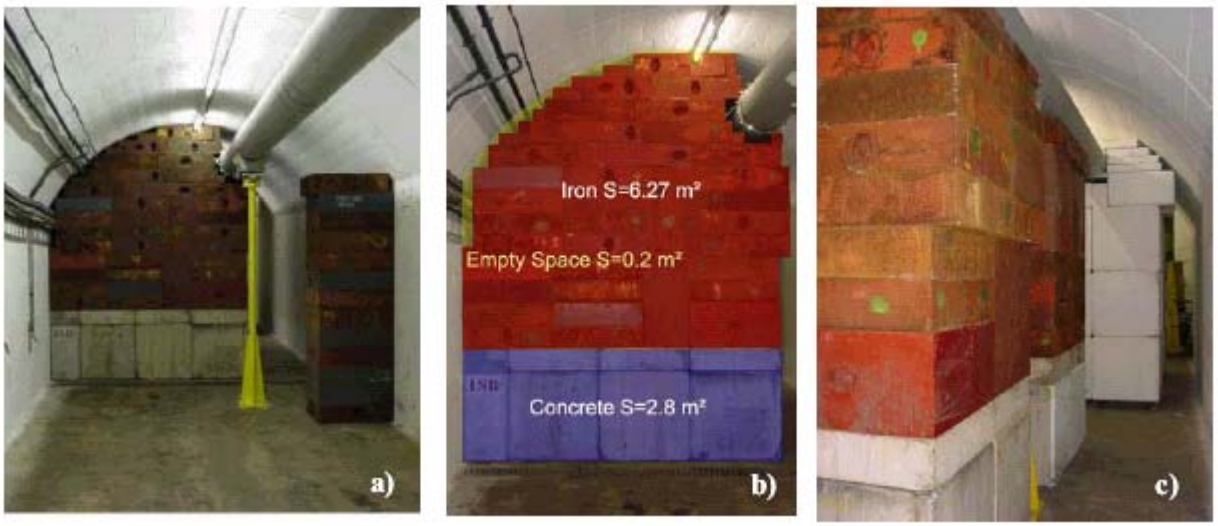

Figure 4.16: The iron wall mounted in n_TOF tunnel between the sweeping magnet and the second collimator; a) front view from the second collimator, b) front view showing the area of the concrete, c) side view.

After the installation of the iron shielding, a strong reduction of the prompt flash (mainly due to γ-rays and high-energy muons) was observed. The comparison of the events recorded before and after the installation, shown in Figure 4.17, demonstrates qualitatively the considerable reduction achieved.

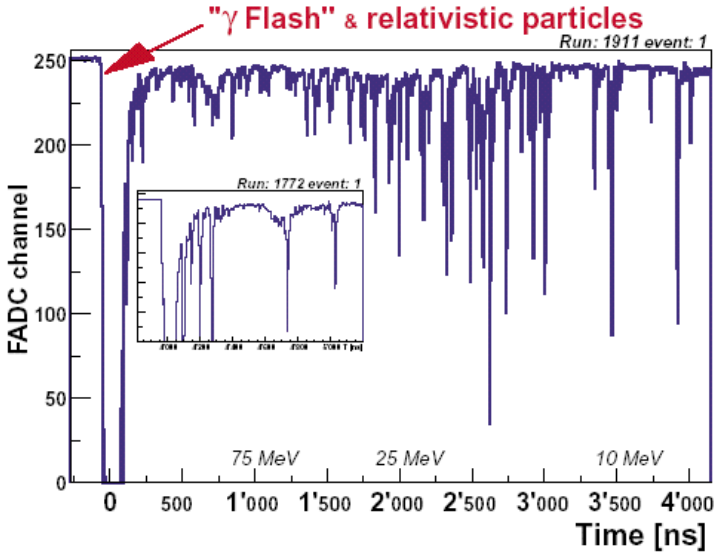

Figure 4.17:Comparison of the γ-flash before (Run 1722 in small panel) and after (Run 1911) the installation of the iron wall. Although the time scales are different, the duration in such two cases are appreciable.

Figure 4.18 shows a summary of the different measurements on the neutron-induced background. The time-of-flight of events detected in C_6D_6 cells is transformed into apparent neutron energy, to give a visual idea of how the background affects the various

neutron energy regions. The black curve shows the observed level of “empty-sample” background as it was first observed at n_TOF. The blue curve shows the level of background after the addition of the iron wall. A large reduction, of a factor of 30, is observed. Part of the residual background is due to the neutron beam itself, as demonstrated by the red curve that shows the background when the beam is stopped in the first collimator (~ 50 m before the experimental area).

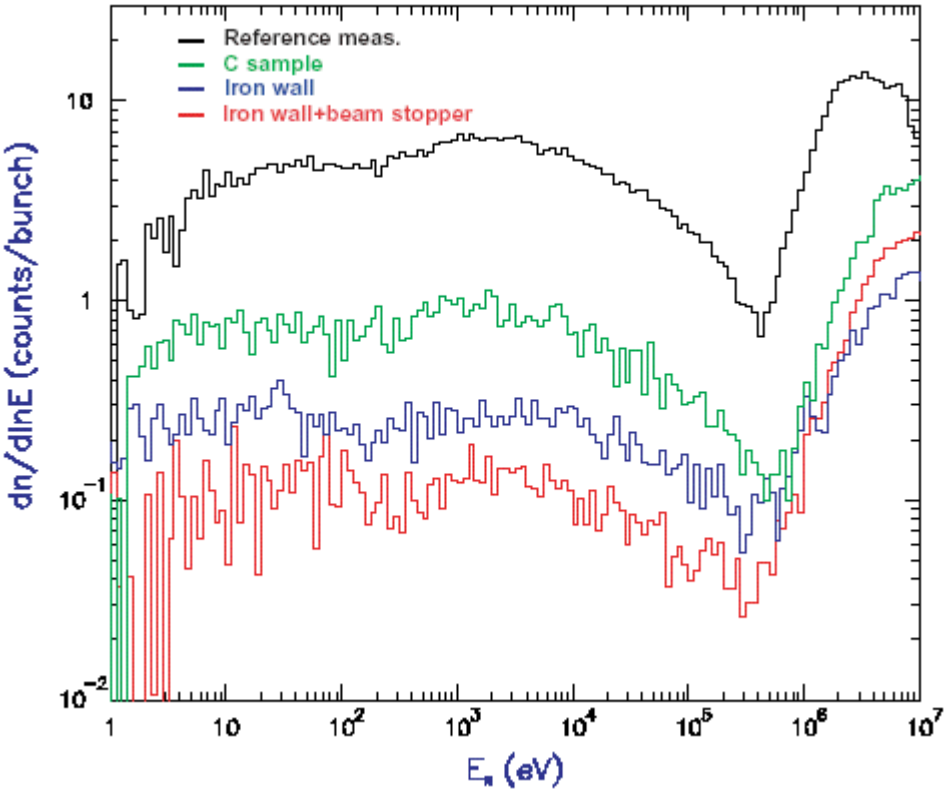

Figure 4.18: Comparison of the background level in different conditions measured with the C_6D_6 in position 1. The black curve represents the reference measurement while the red one is the residual contribution of the muon background after the installation of the iron wall and the insertion of the beam stopper. The beam related component is described in green and represents the 2/3 of the overall estimated background.

Finally, a measurement with the Carbon sample inserted in the beam shows a further increase of the background induced by the neutrons scattered from the sample and captured in the wall of the experimental area or other material therein. The sample-related background constitutes in this case the dominant component.

Other contributions to the ambient background derive from the magnet and the apertures in the experimental area. Finally an important source of background, is related to activation, produced in the primary and secondary area. Low-energy neutrons abundantly produced in the collimator may in fact undergo neutron capture in air or in other material

present in the tunnel. The radioactive isotopes produced by activation can then drift in the experimental area, where they can decay giving origin to signals in the C_6D_6 or other γ-ray detectors. In time, this background is expected to have a constant distribution, while in "apparent" neutron energy it shows up with a power low behavior. Part of the enhancement at low energy is therefore due to activation. With the aim of studying this component, high-resolution γ–spectrometry was performed with HPGD detector. For energy and efficiency calibration the ^{60}Co and ^{152}Eu γ-ray sources were used. Standard NIM electronics was used for the measurement. The detector was placed in the experimental room, 30 cm from the sample changer and at 50 cm below the beam line. The activation measurements were made shortly after shutting down the neutron beam in the experimental area, while a reference background measurement was performed after several hours. The presence of short-lived activation products is evident after subtracting the background from the measured activation spectra, as shown in the right-side plot of Figure 4.19. The 511 keV annihilation peak and the 1293 keV γ–line from the ^{41}Ar decay (1.82 hours) are clearly observed. These therefore represent the main sources of additional γ–background, which is not directly beam related.

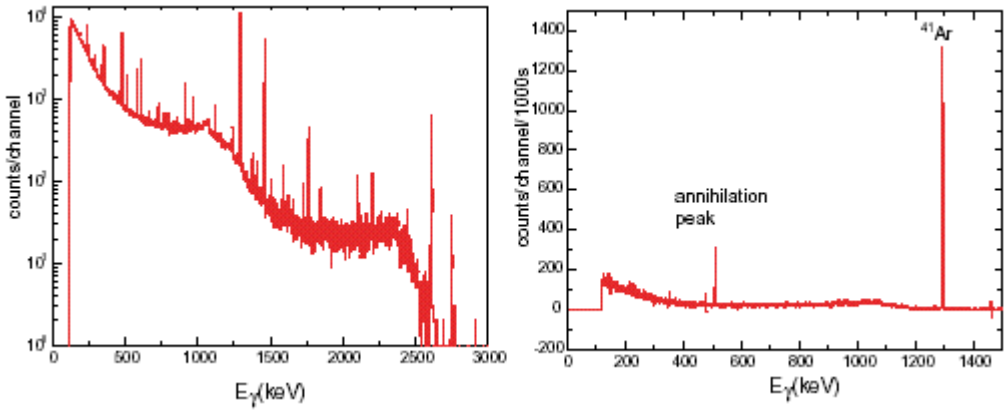

Figure 4.19: γ-ray spectrum measured with HPG detector 3.5 hours after the beam stop (left) and background subtracted spectrum showing the short lived component (right).

The presence of γ–rays from activation was also evident from C_6D_6 measurements. Figure 4.20 shows a background spectrum (black histogram), measured with a C_6D_6 in the fixed position with no sample in place, normalized to the reference n_TOF bunch of 7×10^{12} protons. On the horizontal axis the recording time has been converted into neutron energy in order to illustrate how the various energy zones are affected. In agreement with the

HPGe results, the rise at low energy (long times) was attributed to air activation (^{41}Ar), most probably produced in the primary zone and flowing to the experimental area.

The data shown in the figure were taken after a few days of running with high proton intensity, so that a large activation had already built up. In these conditions, the background due to activation contributes significantly up to few hundreds electronvolts, with the level depending on several factors, such as the beam intensity, build up time, differential air pressure, etc…. The assumption that the observed behavior is due to activation was verified by subtracting the normalized background spectra measured at different times with the same detector and in the same experimental conditions. Since the other components do not change with time, only the activation component survives after the subtraction. As expected, a pure exponential trend is observed over the whole range, (Figure 4.20), with the decay constant of 1.15 for the iso-flux as function of the neutron energy corresponding to a flat time-of-flight distribution. A good remedy to the activation was found by sealing the experimental area with plastic foils. After this intervention a strong reduction of the activation level was achieved.

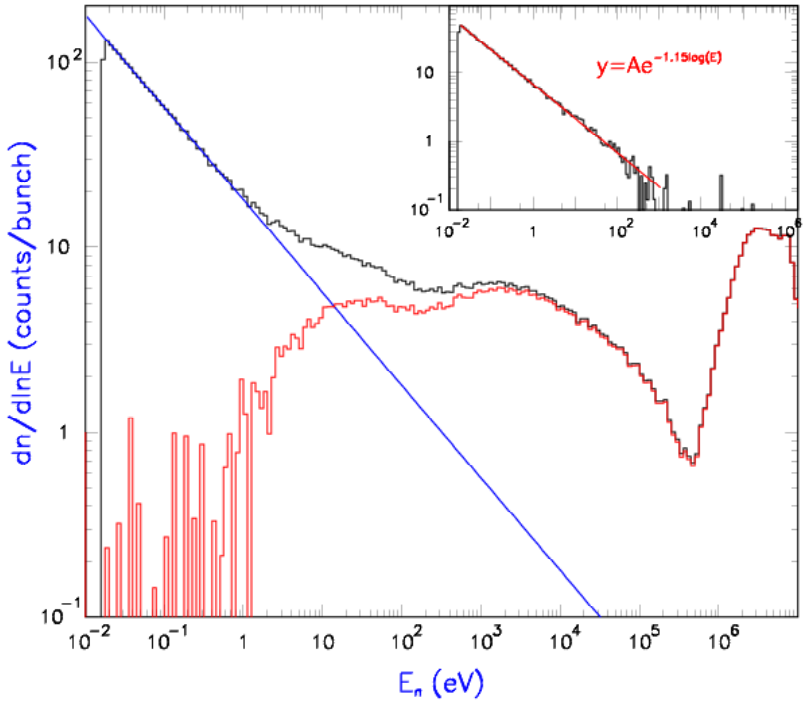

Figure 4.20: Empty-sample background spectrum, measured with a C_6D_6 detector at the sample position (black curve). The activation-free background spectrum (red histogram) is obtained by subtracting an exponential function, normalized to the data in the low-energy region. The subtraction of background spectra taken at different times in the same running conditions shows the exponential trend in logarithmic scale, as expected from a constant activation background.

4.4.2 In-beam photon background

Together with the ambient background, observed without sample, two more components, due to scattered neutrons and γ-rays, have been observed when a sample is inserted in the beam. Figures 4.18 and 4.21 show the effect of a 6.35 mm Carbon sample on the background. At large distances from the sample position, the enhancement of the background can be associated with neutrons elastically scattered from the sample and captured in the walls of the experimental area.

On the other hand, a different mechanism seems to be at the origin of the strong enhancement observed in the detectors close to the sample, with a bump centered around 100 μs (or 10 keV in the reconstructed neutron energy). Since the magnitude of this component drops when moving away from the sample, solid angle considerations suggest that these γ-rays are generated from the sample itself. Furthermore, the time-of-flight distribution of the background resembles the predicted time-of-flight distribution of in-beam photons, shown in Figure 2.14.

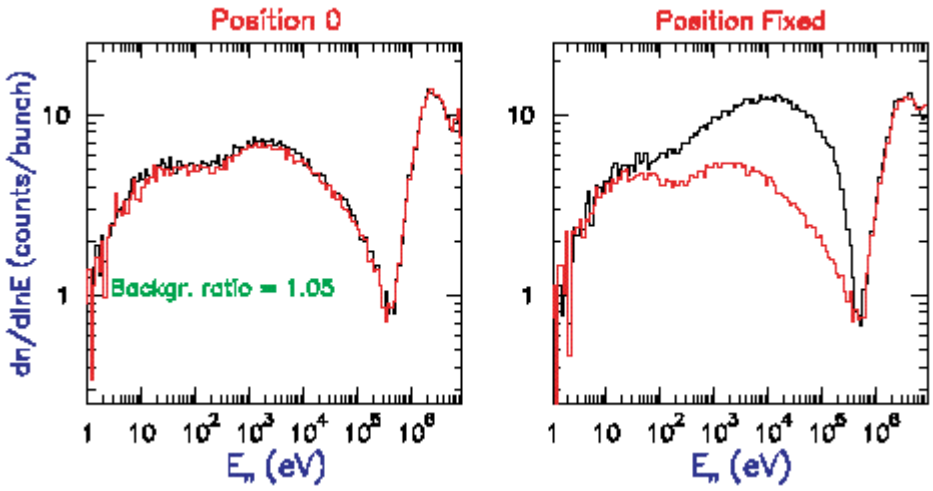

Figure 4.21: Comparison of the background spectra relative to no-sample (red) and C-sample (black), for two different positions inside the experimental area. At large distances (position 0), the two components result almost equal while close to the sample an additional soft γ-ray spectrum is observed.

To study this component of the background, we have simulated the interaction of in-beam photons in two samples: Carbon and Thorium. For sake of simplicity, simulations have been performed for three energies: 0.511, 2.2 and 7 MeV, which constitute the largest component of the in-beam photons (see Figure 2.14). Figure 4.22 shows the results of the simulations for a Carbon sample 6.35 mm thick and 2 cm diameter while in Figure 4.23 the

same results are illustrated for a Thorium sample of 1 g/cm^2 of superficial density. The interaction mechanism strongly depends on the isotope considered, being Compton scattering the main process for light elements, while pair production dominates for nuclei of large atomic number. However the overall background does not show significant variations if the samples have the same superficial density. Furthermore, a general conclusion is that the spectrum of this background component is soft, and does not extend much above 500 keV. Therefore the application of the weighting function or a higher threshold in the detectors (more than 100 keV) should allow to cut a large fraction of this background component.

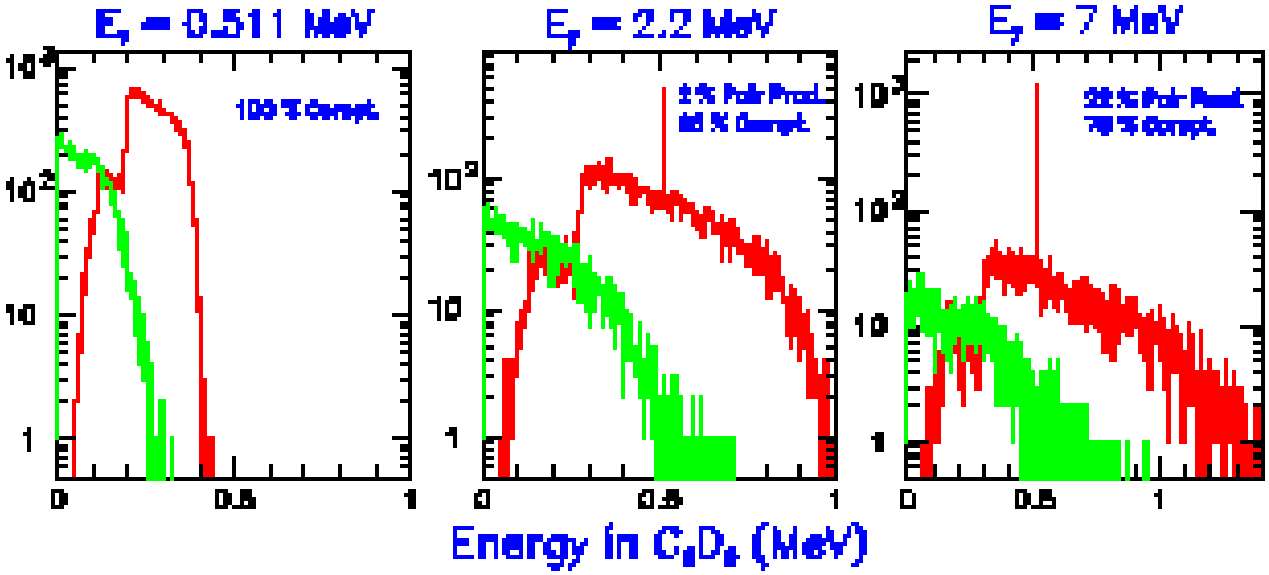

Figure 4.22: Spectrum of the γ-ray (in red) scattered on a Carbon sample 6.35 mm thick. Green histogram shows the deposited energy of the γ-ray in the C_6D_6.

Another consideration should be made on this background component, related to the angular distribution of the Compton scattering and pair production process. The first process is peaked forward while in the second one, photons are isotropically emitted in the center of mass system. Therefore a strong reduction of the background associated with Compton scattering, which dominates at low γ-ray energy and for light elements, can be achieved by placing the C_6D_6 detectors at 90°, or backwards, with respect to the beam direction; this set-up has been used in the measurement of ^{151}Sm, discussed in Chapter 5.

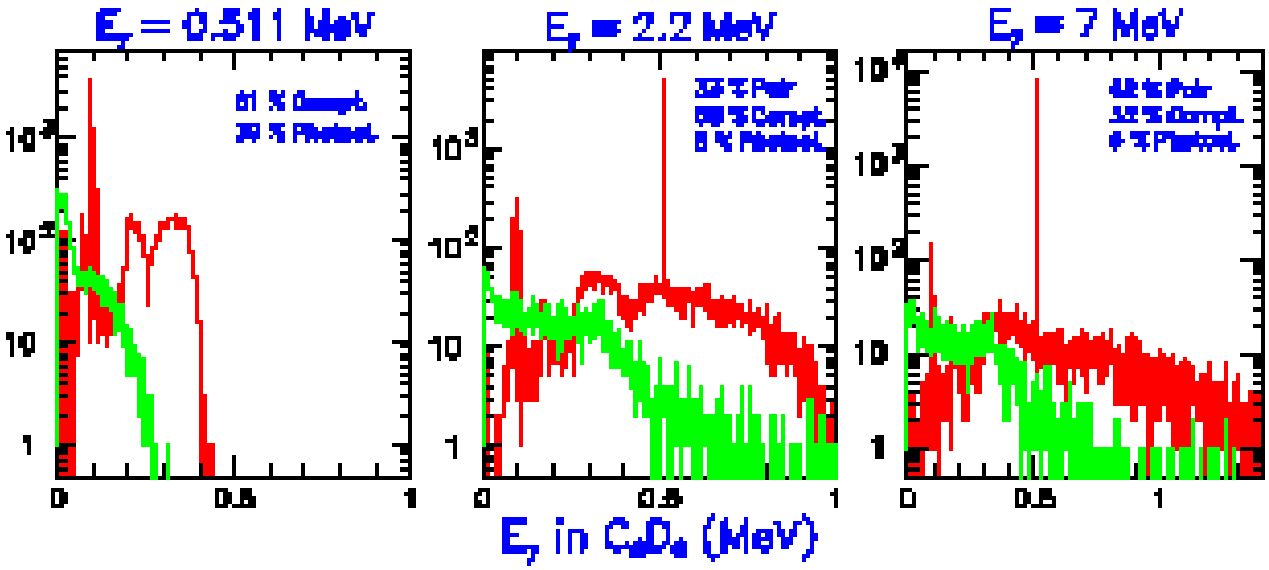

Figure 4.23: The same simulations of Figure 4.22 for a Th sample of 1 g/cm^2 superficial density.

4.4.3 Background from sample-scattered neutrons

As already mentioned, at large distances from the sample position, the enhancement of the background can be associated with neutrons elastically scattered from the sample (see Figures 4.18 and 4.21). The background producing mechanism, in this case, consists of neutrons scattered by the sample and being captured by the concrete walls and/or massive surrounding materials. Such a mechanism becomes particularly important for samples with a capture cross-section much smaller then the elastic one. Under these conditions for some specific isotopes, the sample related background becomes dominant over other contributions and needs to be investigated.

Monte Carlo simulations have been performed with GEANT, in which the experimental area and the Bicron C_6D_6 detector geometry have been reproduced. The effect of the neutron scattering was estimated by simulating the neutron interaction with a C sample 6.35 mm thick and 45 mm diameter. It should be noticed that C is a very convenient sample for studying the effect of neutron-induced background both in the simulations and in the real measurements of capture reactions. In fact, as shown in Figure 4.24, the capture cross-section of C is negligible relative to its elastic cross-section. As a consequence, γ-rays measured with a C sample in the beam are exclusively related to the background. Figure 4.25 shows the background distributions as a function of the neutron energy (reconstructed from the time-of-flight) for the “nude” experimental area, i.e. without any other material. This background component is approximately flat up to a few hundred keV. For higher

energies (especially above 1 MeV) the onset of inelastic reactions, and the detection of the scattered neutrons inside the detectors, produce a fast rise of the background component.

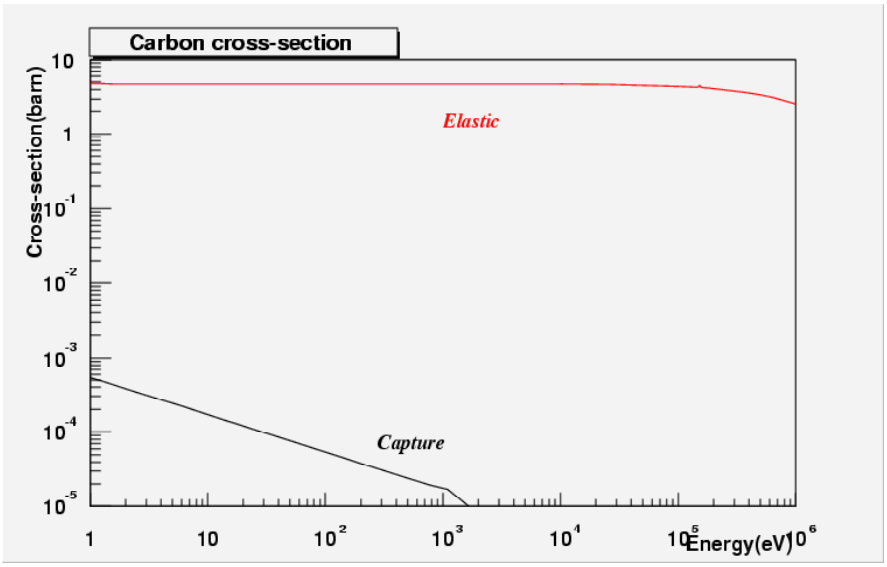

Figure 4.24: Comparison of the Carbon elastic and capture cross-section.

Since capture cross-section measurements are typically performed for neutron energies below 1 MeV, the large neutron and γ-ray background present at higher energy does not poses particular problems for capture measurements. Nevertheless, an accurate experimental determination of the neutron-induced background is performed in all measurements by means of a C sample, which has a negligible capture cross-section and allows to isolate the neutron-induced background in the specific experimental condition.

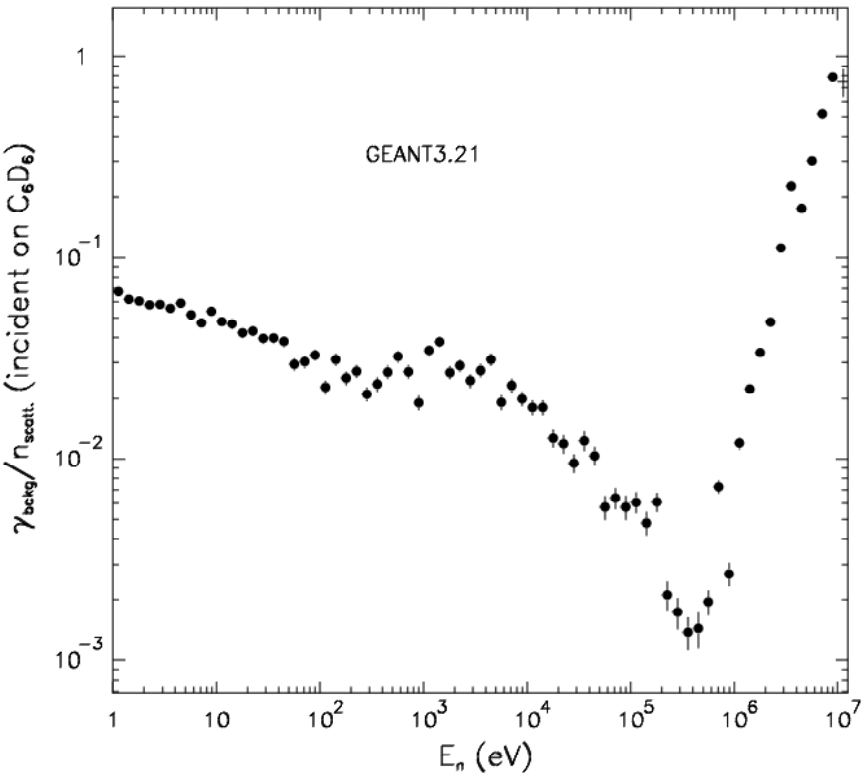

Figure 4.25: γ/n ratio of the particles, scattered by a C sample and detected in the C_6D_6, as function of the neutron energy.

The effect of the background on the capture cross-section measurements can be estimated from the analysis of the main resonances in standard samples, such as ^{197}Au, ^{109}Ag and ^{56}Fe. The improvement in the background level achieved with the installation of the iron wall can be appreciated by considering the peak-to-valley ratio for the largest resonances (4.9 eV in ^{197}Au or 1.150 keV in ^{56}Fe), as well as by the possibility to identify some weak resonances. Figure 4.26 illustrates the situation of the sample for the ^{197}Au before and after the installation of the iron shielding. The improvement is the region up to 100 eV and is evident, and it is still appreciable until 1 MeV. For higher energies, a different method, based on fission measurements has to be used.

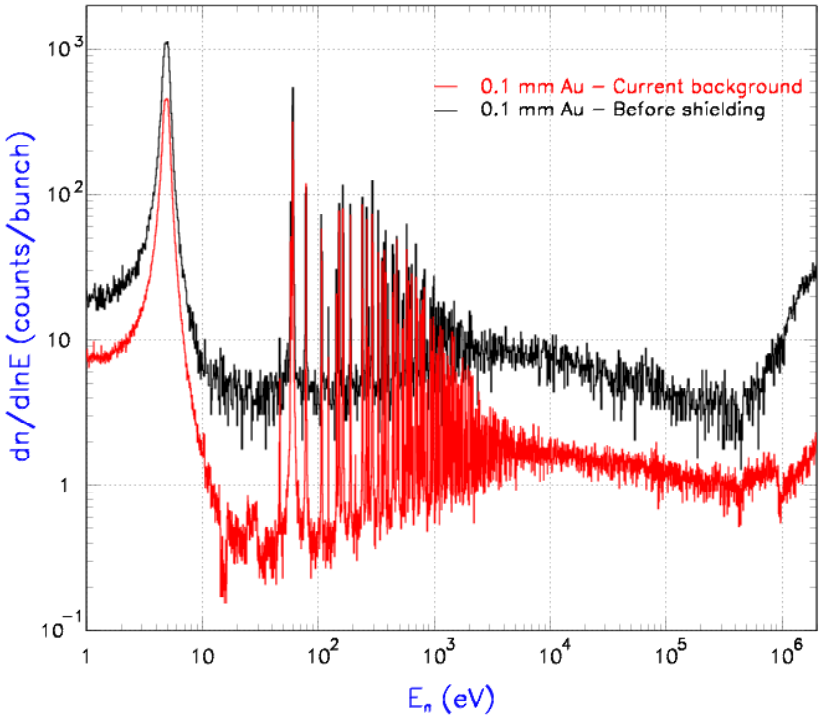

Figure 4.26: Count rate measured with the C_6D_6 for Au 0.1mm thick a). Black lines are referred to measurements before the installation of the iron wall.

In conclusion, the results of the measurements indicate that the ambient background at n_TOF, after the addition of appropriate shielding for muons, is as low as originally planned. As expected on the basis of the simulations, the observed level is lower than the one present at other facilities. The presence of additional background components related to the sample, however, cannot be neglected. One of these components is due to neutron scattered from the sample and moderated or captured in the walls of the experimental area or other material. Some attempt to minimize this component could be performed in the future by covering the experimental wall with lithiated paraffin.

The second component of the background, which is particularly strong in the keV region, has been identified as due to the γ-ray contamination of the neutron beam. Following interaction with the sample, such γ-rays can be scattered in the detectors, thus affecting the cross-section measurements, in particular for capture reactions. It needs to be accurately investigated and subtracted for each sample under investigation. Since most of

the in-beam γ-rays are originated by the radiative capture in the moderator water (producing 2.2 MeV photons, as evident in figure 2.14), a strong reduction of this component would be achieved by using heavy water for cooling of the spallation target and for moderation.

Chapter V

5.1 Introduction

Following the completion of the facility and the neutron beam characterization, a large experimental program has started at n_TOF. Aim of the project is the measurement of neutron cross-sections relevant to Astrophysics and to several applications, in particular to Accelerator Driven Systems for energy production and nuclear waste transmutation.

The main objective of the measurements is to collect new and accurate data on capture, neutron induced fission and inelastic reactions for different isotopes. Taking advantage of the innovative characteristics of the neutron beam, the new measurements are expected to improve the quality of existing data and, more importantly, to provide cross-section data still completely missing or incomplete, as in the case of most radioactive sample that constitute the nuclear waste. In particular, the low background, high resolution, wide energy range and high instantaneous flux of n_TOF will allow:

to improve the accuracy on some isotopes for which discrepancies exist (low background);

to extend the resolved resonance region (high resolution);

to collect data at higher energy, for fission and inelastic reactions (wide energy range);

to measure radioactive isotopes or small sample isotopes (high instantaneous neutron flux).

The experimental program started with the measurement of capture reactions. This thesis discusses one of the first measurements performed at n_TOF: the ^{151}Sm(n,γ) reaction. For this isotope, no data on neutron capture are reported in literature, mainly due to the radioactivity of the sample, that makes difficult to measure capture cross-sections with good accuracy at previously existing facilities. Since the lifetime of ^{151}Sm is 90 years, even a few hundred milligrams of this isotope results in a very large activity, of the order of several Gigabecquerel, which may strongly affect the measurement of γ-ray from capture reactions. The high-instantaneous neutron flux of the n_TOF beam results in a much better

signal-to-background ratio, thus making possible for the first time an accurate measurement of the capture cross-section for this isotope.

The present chapter presents the first experimental determination of the ^{151}Sm(n,γ) cross-sections. After a brief description of the scientific motivation and of the experimental apparatus employed, a discussion on the data analysis is given. The first, preliminary results on resonance analysis are presented, together with the extracted cross-sections in the unresolved resonance region. Since some aspects of the analysis, in particular the determination of the Weighting Functions and the subtraction of the background, rely on Monte Carlo simulations, systematic uncertainties may affect the results. A discussion on the estimated magnitude of these uncertainties is given at the end of the chapter.

5.1.1 Scientific motivation for the ^{151}Sm(n,γ) cross-sections

The measurement of capture cross-sections for ^{151}Sm has important implications both for Astrophysics and for ADS. The importance for ADS resides in the fact that ^{151}Sm is a fission fragment abundantly produced in nuclear reactors. Although its lifetime is relatively short compared to other, long-lived fission fragments, it would still be desirable to include this isotope in any incineration scheme. Since the transmutation of ^{151}Sm to a stable nucleus can only proceed through neutron capture (producing the stable ^{152}Sm), cross-sections for (n,γ) reactions from thermal to 1 MeV neutron energy are needed. A specific request in this sense, identified by the number 4.D.28, is included in the NEA "High Priority Nuclear Data Request List".

Together with the ADS-related aspect, the ^{151}Sm(n,γ) cross-sections results important also for the field of Nuclear Astrophysics ^{151}Sm is in fact one of the important branching isotopes. Due to its lifetime, this isotope has the possibility of undergoing a neutron capture or, alternatively, to decay by β-emission. The relative probability of the two processes (that is the branching ratio) depends on the stellar thermodynamic condition, in particular on the neutron density and on the temperature, as well as on the neutron capture cross-section. Therefore, if the cross-sections are accurately known, it is possible to obtain information on the stellar conditions in which the process occurs.

5.2 Experimental set-up

Two C_6D_6 with Carbon-fiber container, described in § 3.3, were used in the experiment (the detectors were developed specifically for the measurements at n_TOF at the Forschungzentrum Karlshrue). They were placed close tangent to the vacuum tube, perpendicular to the neutron beam direction. To minimize the background induced by in-beam γ-rays, described in § 4.4, the two detectors were shifted backwards with respect to the sample position by 9 cm, as shown in Figure 5.1. Due to the radioactivity of the measured isotope, it was not possible to mount the sample in vacuum. Therefore, a new sample changer operating in air had to be designed, specifically for the measurement of Samarium and other radioactive samples. A picture of the setup is shown in Figure 5.3. The n_TOF vacuum tube was interrupted a few centimeters before the sample changer and resumed after a few centimeters, in order to minimize the background induced from neutron scattering in air. The vacuum-air interface consisted of two Kapton windows 25 μm thick.

The gain of the photomultiplier and the range of the Flash ADC were chosen so that the full scale was slightly higher than the capture energy for the ^{151}Sm, which is 8 MeV. A hardware threshold of 150 keV was kept on the FADC. The standard sampling rate of 500 MHz (corresponding to a sample every 2 ns) was used. Combined with the 8-bit resolution of the module, and the 8 Mbyte memory, this allowed to collect data up to 16 ms following the PS trigger, equivalent to a minimum neutron energy of 0.6 eV.

The sample used in the measurement was produced in Oak Ridge (USA), by compressing 0.2064 grams of Sm_2O_3 powder into a disk of 1 cm diameter (it is not possible to produce a pure Samarium sample because the material is hygroscopic and oxides very quickly). The isotopic composition of the Samarium contained in the sample is reported in Table 5.1. The other samples used in this measurement have the same diameter of Samarium in order to intercept the same percentage of the flux and are: ^{197}Au 1 mm thick and mass of 1.4855 g necessary for flux determination, ^{nat}C 1.5 mm thick and mass of 0.2306 g and ^{nat}Pb 1 mm thick and mass of 0.9574 g for background determination. All samples were encapsulated in a Titanium can, with wall thickness of 0.2 mm and a total weight of 0.40104 g, and with an inner empty space of 1 mm, to host the samples. This arrangement avoids the dispersion of the powder in the environment and results necessary for the highly radioactive Samarium sample.

Table 5.1: Isotopic Composition of the Sm_2O_3 sample.

Isotope	^{144}Sm	^{147}Sm	^{148}Sm	^{149}Sm	^{150}Sm	^{151}Sm	^{152}Sm	^{154}Sm
Atom Fraction	0.051%	1.385%	0.222%	0.404%	3.973%	89.941%	3.356%	0.667%

5.3 Data analysis

The data reduction and analysis requires a careful consideration of many different aspects. The main steps can be summarized as follows:

Energy calibration of the detectors;

Choice of suitable cuts for electronic noise rejection and for the rejection of the neutron signals at higher energy;

Calculation of the weighting functions;

Neutron flux determination (via the Au measurement);

Estimate of the different background components and their subtraction.

It should be noted that the whole procedure has to be applied not only to the Samarium sample, but also to the analysis of the $^{197}Au(n,\gamma)$ reaction, used for absolute normalization, or to any other sample used in the measurement.

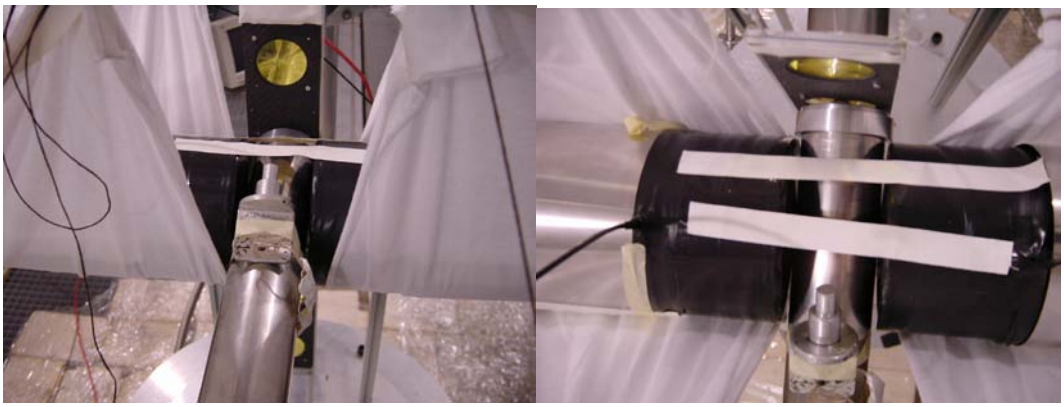

Figure 5.1: Front view on the left and top view of the C_6D_6 detectors set-up for the Samarium campaign of measurements.

The energy calibration of the detectors was performed with three γ-ray sources: ^{137}Cs γ-ray at 662 keV, ^{60}C average γ-rays at 1.250 MeV and Pu/C γ-rays at 6.130 MeV for

higher energy. For an accurate calibration, the response of the detectors was simulated for the three sources and the deposited energy was convoluted with the detector resolution. It was found that, for the new C_6D_6 used in the measurement, a good reproduction of the detector's response can be obtained with the following expression for the variance: $(\sigma/E)^2 = 3\cdot10^{-3} + 5\cdot10^{-3}/E$, where E is expressed in MeV. Figure 5.2 shows the comparison between the measured spectra for the three sources and the simulated ones. The channel corresponding to the half maximum of the Compton edge was used for the energy calibration. The corresponding energies extracted from the simulations are: 0.542 for Cs, 1.136 for Co and 6.034 for Pu/C . A first-order polynomial fits nicely the three points, implying that the detector response is linear at least up to 6 MeV and that no other saturation effects, for example on the FADC, are present. The results of the fit for the two detectors are shown in the Figure 5.2.

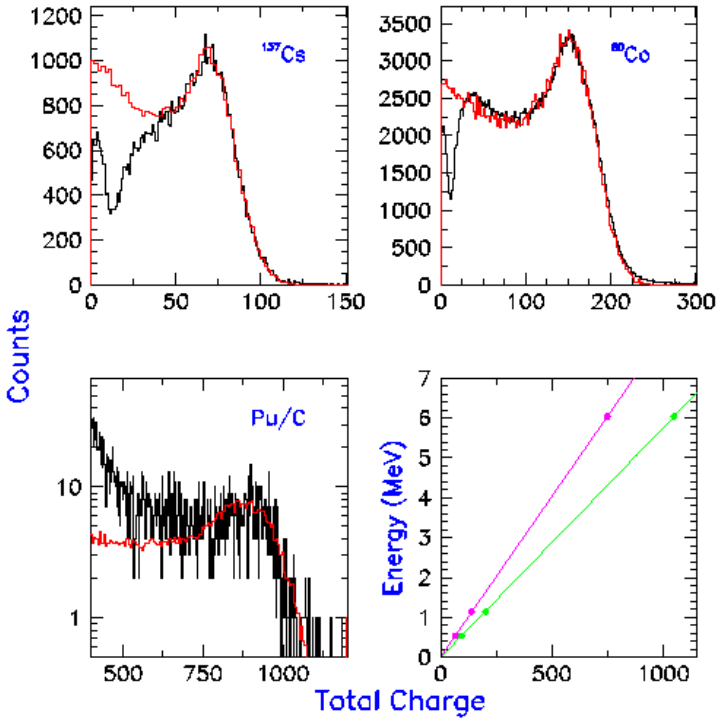

Figure 5.2: Measured (black histogram) and simulated response of one C_6D_6 to γ-rays from three different sources. The detector resolution was included in the simulations, according to the formula indicated in the text. The energy calibrations are shown in the lower-right panel; the parameters are: detector 1 (green line) -0.0129, 0.00576; detector 2 (purple line) 0.0062, 0.00812.

For an accurate determination of the capture cross-sections, it is important to apply conditions that allow to identify the capture γ-rays with a well defined threshold, which enters in the estimate of the Weighting Functions and efficiently reject spurious events, such as those generated by the electronic noise or by neutrons. Given the properties of the

liquid scintillator [52], it is natural to apply the standard method of a pulse shape analysis to reject neutrons. The method consists in selecting γ-rays by means of a 2-Dimensional gate in the spectrum of Fast versus Total integration of the signal. The Fast integration represents the charge content in the first part of the signal, and is simply obtained by summing up all samples from the start of the signal up to the peak. The Total integration, instead, is obtained over the whole duration of the signal. In both cases the integral of the baseline is subtracted from the signal integral. Figure 5.4 shows the spectrum of the Fast vs Total charge. Neutrons are clearly located outside the γ-ray region, so that they can be easily discriminated by means of a two-dimensonal gate; similar results can also be obtained by applying the cut in the Amplitude versus Charge plot.

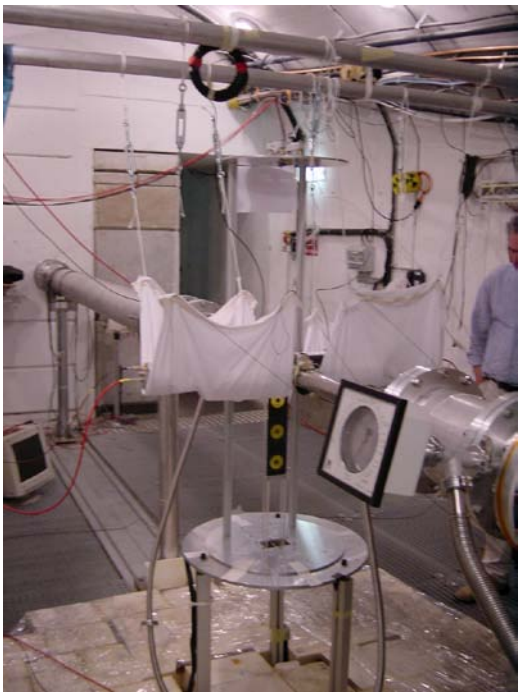

Figure 5.3: Sample changer in air with the C_6D_6 detectors installed for the Samarium measurement.

A software threshold of 200 keV, higher than the hardware threshold of 150 keV, was applied in the analysis and considered in the determination of the weighting functions. It was found that this threshold is able to completely eliminate the electronic noise, which was in some cases affecting the measurement. A more refined method, based on the fitting of the pulse shape as described in Appendix I, for the n/γ discrimination and for the resolution of pile-up events does not seem necessary and was therefore not applied in this case.

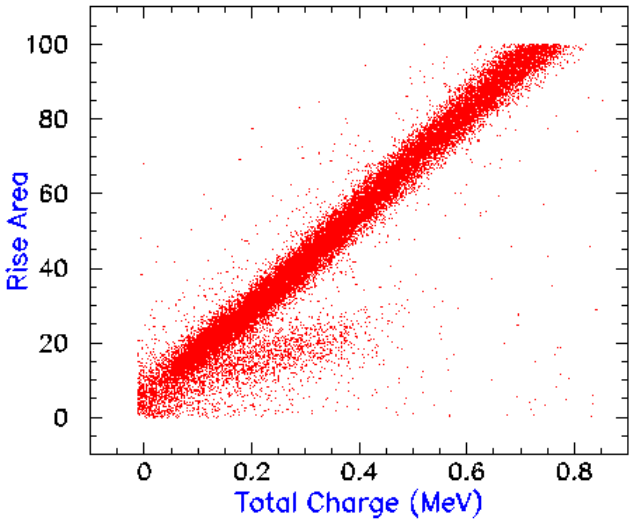

Figure 5.4: **A spectrum of the Fast versus Total Charge integrations allows to discriminate γ-rays from neutrons (on the right of the main region). A software threshold of 200 keV on the total charge allows to completely reject any electronic noise.**

5.4 Calculations of the Capture yield

As described in § 3.3, the analysis of C_6D_6 data for capture cross-section determination relies on the Pulse Height Weighting Function method. As in previous cases, the Weighting functions for all samples measured in the ^{151}Sm capture experiment, were obtained from simulations of the detector response performed with GEANT-3.21 and GEANT-4, with a realistic software replica of the experimental apparatus and including the resolution of the detector and the applied light-output threshold. The simulated apparatus, as reproduced with the drawing package of GEANT-4, is shown in Figure 5.5.

After simulating the detector response for different γ-ray energies and for all samples used in the measurements, a least-square fit method was applied to extract the weighting functions (the details of the method are described in § 3.3). The parameters of the 4th degree polynomial used as weighting function, resulting from the least-square method, are reported in Table 5.2.

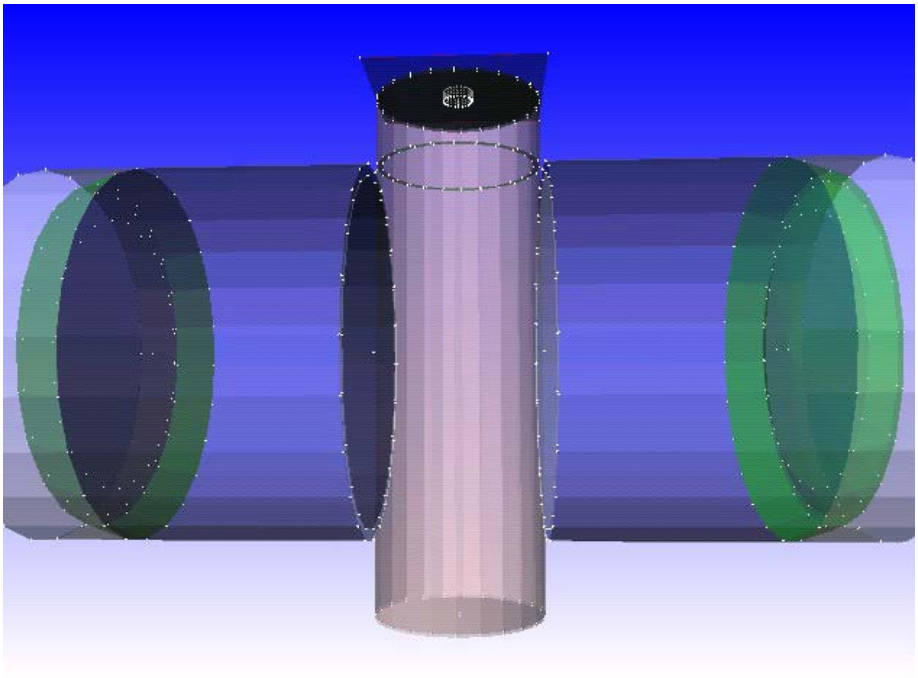

Figure 5.5: Top view of the Sm set-up implemented in GEANT-4.

To extract the capture yield, the weighted energy spectrum, normalized to the nominal proton bunch of 7×10^{12} protons, has to be divided by the isolethargic neutron flux per bunch *dN/dlnE* and by the capture energy E_c (see Equation 4.2). An accurate determination of the neutron flux, which takes in account also a sample dimension smaller than the beam profile, can (and will) be obtained from the reference measurement with the Au sample. However, as a first approximation the capture yield is obtained by dividing the weighted spectrum for the neutron flux experimentally determined with the PTB chamber during the commissioning of the facility, parameterized between 1 eV and 1 MeV, with two different 4^{th} order polynomials.

Table 5.2: Parameters and errors of the Weighting functions calculated according to the Poisson distribution (see note for more details).

Parameters / Sample	a_o	a_1	a_2	a_3	a_4
^{197}Au	7.863± 0.114	13.316± 0.258	17.128± 0.145	-2.058± 0.028	0.063±0.002
Sm_2O_3	1.536± 0.081	27.031± 0.183	8.234± 0.105	-0.201± 0.021	-0.011± 0.001

Figure 5.6 shows the capture yield measured in the experiment for the different samples. The two C_6D_6 detectors were summed together. However, a difference of ~10 % was observed between the yield extracted from the two detectors. Since all conditions in the analysis were kept the same, it was concluded that the two detectors presented a different efficiency, due to a slightly different volume of the C_6D_6 scintillator. Although the Weighting Functions were done for two detectors of the same active volume, the use of an overall normalization factor extracted from the Au sample accounts completely for the different efficiency.

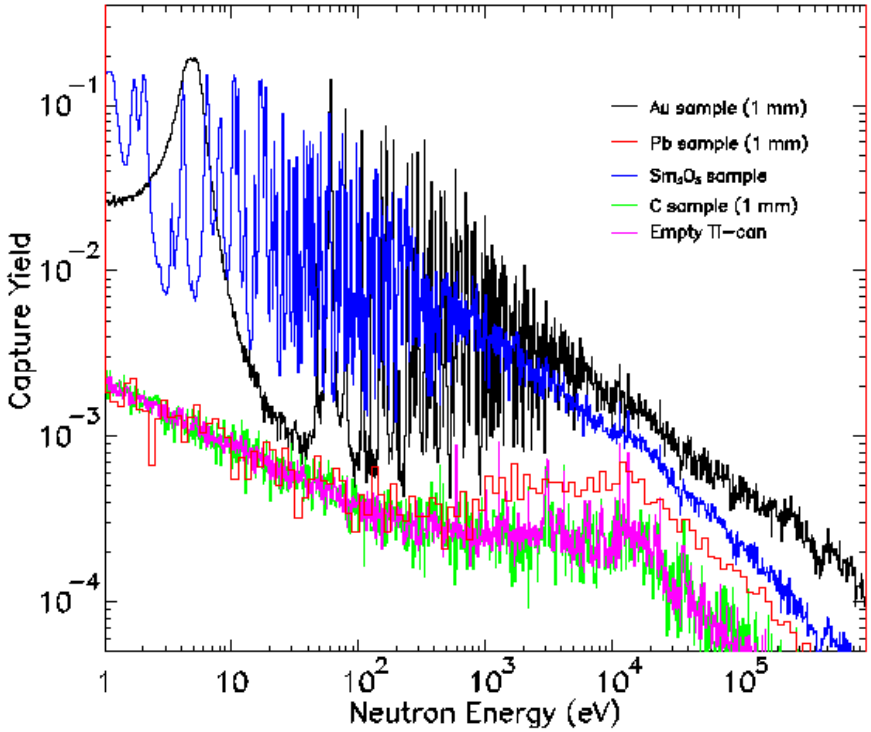

Figure 5.6: Capture yield for the different samples used in TOF-03. The spectra are obtained after application of the relative weighting functions. The spectra are made with 200 bins/decade except for the Pb (20 bins/decade) due to the poor statistics.

The normalization between different runs was performed by means of the number of protons (all bunches without proton beam information were rejected). A comparison with the counts recorded for each run in the Silicon flux Monitor indicated that the proton information was accurate for most of the runs. A few runs, amounting to about 15% of the total statistics for the Sm_2O_3 sample, were disregarded, since they showed some anomaly, probably due to a temporary misalignment of the proton beam on the spallation target.

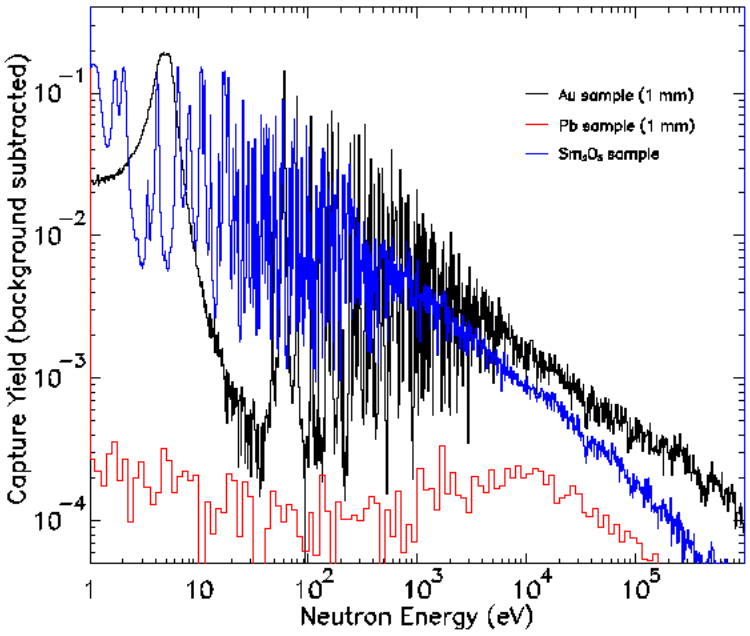

Figure 5.7: Capture yield for Au, Pb and Sm after subtraction of the empty background (weighted for the corresponding weighting functions, see text for detail). Notice the complete disappearance of the Ti resonances at 10 keV.

The empty sample shown in the figure was corrected with the weighting functions of Sm. It should be noticed that, for background subtraction, the empty spectrum should be corrected for the Weighting Functions of the sample from which it is being subtracted (for example, when subtracting the background from the Sm_2O_3 spectrum, the yield for the empty-can should be constructed with the Weighting Functions of the Sm_2O_3). The spectra for Sm_2O_3, Au and Pb samples after subtraction of the background measured with the empty Ti container are shown in Figure 5.7. The correctness of the subtraction procedure is demonstrated by the complete disappearance of the Ti resonances around 10 keV in both spectra. From Figure 5.7 it is evident that the resolved resonance region, up to 1 keV, is not affected by the empty-sample background. An analysis of the resonances for Au and Sm can therefore be performed by means of the analysis code SAMMY, without the need of further considerations. On the contrary, the region of the unresolved resonance region requires a more careful analysis of an additional background component, discussed in the next paragraph**.**

5.5 Background determination

As described in § 2.4, several sources of background affect the capture cross-section determination, with different contribution in different energy regions. Together with the ambient background (which is observed without any sample in the beam), spurious counts are generated by the Ti-can containing the Sm_2O_3 sample, by neutrons and by in-beam γ-rays scattered by the sample. For an accurate determination of the cross-section, each of these components has to be evaluated and, if necessary, subtracted from the measured spectrum. The first two components, i.e. the ambient background and the one generated by the Ti-can, were jointly estimated by means of an empty container similar to the one hosting the sample. The corresponding spectrum is shown in Figure 5.6 (purple histogram). Apart for some resonances related to the capture in Ti, the container does not seem to produce an additional background, relative to the known ambient one. A similar conclusion can be drawn for the background generated by the sample-scattered neutrons, whose effect was estimated by means of a C sample. As shown by the green histogram in Figure 5.6, no enhancement is observed with the C sample, in any region, thus demonstrating that the effect of scattered neutrons is negligible. The results for the C sample can be easily extrapolated to the Sm_2O_3 sample, as well as to the Au and Pb samples measured in the same experiment, by scaling for the relative number of atoms/barn and for the elastic cross-sections.

In the case of the Sm_2O_3 sample, the evaluated elastic cross-section is on average higher by one order of magnitude than the known elastic cross-section for C, see Figure 5.8. However the number of atoms per barns of the Sm_2O_3 sample is a factor of ten lower than for C, so that the number of scattered neutrons is estimated to be approximately the same. Similar arguments apply also to the other samples used in this measurement. Therefore, in all cases it can safely be concluded that the effect of sample-scattered neutrons is negligible.

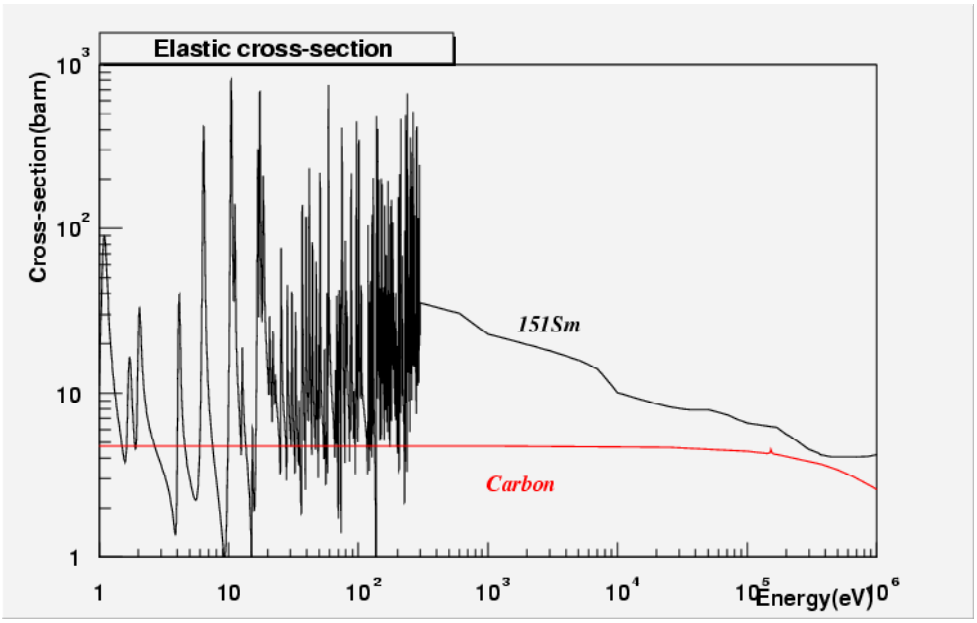

Figure 5.8: Comparison between neutron elastic cross-section of ^{151}Sm (black curve) and C (red curve).

The C sample histogram also indicates that, due to the backward angle of the detectors, scattered γ-rays from the beam do not generate additional background, for a threshold on the detector light output greater than 200 keV. This can be easily understood by considering that Compton scattering is the dominating mechanism for light elements and that the energy of the scattered γ-rays at backward angle is typically below 300 keV, independent of the original γ-ray energy. This consideration, however, does not apply to all other samples, in particular to heavy elements, since the contribution of different scattering mechanisms depends on the atomic number of the sample [45]. In fact, the measurement of a Pb sample 1 mm thick shows an enhancement of the background in the region above 1 keV, which even survives the application of the weighting functions (red histogram of figure 5.7). Such an enhancement is related to an increased contribution of pair production in γ-ray interaction, which results in a number of events in the C_6D_6 above the threshold of 200 keV.

A quantitative estimate of the in-beam photon background, for all samples measured in the experiment (that is C, Sm_2O_3, Pb and Au), was obtained by means of simulations performed with GEANT-3.21. The same, detailed software replica of the apparatus used for the weighting function determination was also employed in the background simulations. In-beam γ-rays are generated according to the expected energy distribution (see Figure 2.14). In Figure 5.9, the results for all four samples are presented. The right panel shows the energy spectrum of the γ-rays hitting the C_6D_6, while the left panel shows the deposited

energy. The simulations indicate that for the Sm_2O_3 sample, the contribution of in-beam γ-rays is at the same level of the C sample and can therefore be neglected. On the other hand, this component affects considerably the Au and Pb sample, for which a larger fraction of the deposited energy spectrum extends above the 200 keV threshold. This additional background has to be estimated and subtracted in the case of the Au sample, which is used for the determination of the neutron flux intercepting the sample. It is important to remember here that the radius of the samples is smaller than the neutron beam dimension, so that only a fraction of the total neutron flux contributes to the reaction rate. The exact fraction has therefore to be determined by means of the reference measurement with the Au sample having the same dimension of the Sm_2O_3 sample.

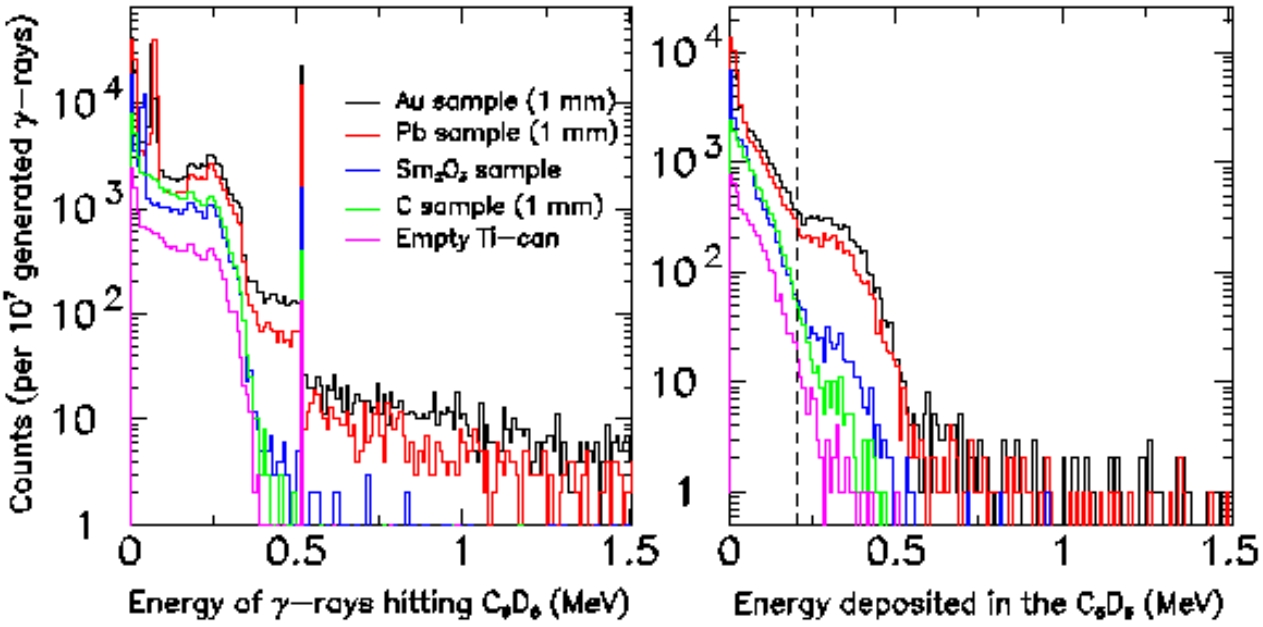

Figure 5.9: Simulations of the background induced by sample-scattered in-beam gamma rays, for the different samples used in TOF-03. The left panel shows the energy of the γ's hitting the C_6D_6 detectors, while the right panel represents the energy deposited in the detector. The threshold of 200 keV used in the analysis is indicated in the figure.

A comprehensive summary of the expected in-beam γ-background is reported in Table 5.3. As already mentioned, the background generated by the Sm_2O_3 sample is comparable to the one of C, and more than 10 times smaller than for Pb. For the Sm_2O_3 sample, therefore, it can be assumed that the overall background, to be subtracted from the measured spectrum, coincides with the empty Ti-can. This assumption, however, has been verified also by means of measurements with the resonance filters. In particular, an Al plates 29.4 mm thick inserted in the beam allows to check the overall background at 6 keV energy. A strong resonance exists in the total cross-section at that energy for Al, so that all neutrons are

removed from the beam. For this reason the Al inserted in the beam constitutes a black resonance filter. The remaining counts observed at the energy of the black resonance are obviously due only to background. In the case of Sm, as shown in the figure, this is estimated to represent … % of the total extracted cross-section, after subtraction of the empty-can contribution. On the other hand, for Au the in-beam gamma-ray background component is estimated to significantly affect the measured spectrum, being 1.5 times bigger than the one measured for Pb. Therefore it has to be correctly considered when using the Au sample for neutron flux determination.

Table 5.3: Simulated probability of in-beam γ-ray events in the two C_6D_6 detectors (total and above 200 keV), for the four samples used in TOF-03. The C and Sm_2O_3 samples present a background more than 1 order of magnitude smaller than the one of the Pb sample.

Sample	*Total detected (per incident γ)*	*Above200 keV Threshold*
Ti container	4.8×10^{-4}	8.2×10^{-6}
C (1.3 mm)	1.5×10^{-3}	2.7×10^{-5}
Sm_2O_3 (0.4 mm)	2.2×10^{-3}	5.4×10^{-5}
Au (1 mm)	6.0×10^{-3}	6.3×10^{-4}
Pb (1 mm)	5.6×10^{-3}	4.2×10^{-4}

5.6 Analysis of the resolved resonances

A fit of the resonances was performed with SAMMY, in the Reich-Moore approximation (some details on this code are given in Appendix II). The parameters of an RPI resolution function were fixed to those extracted from dedicated measurements with Au and Fe samples, performed during the neutron beam characterization. The normalization constant, the background and the resonance parameters were kept free. Figure 5.10 shows the results of the SAMMY fit for some of the resonances (in the 1-100 eV region) of the Au sample. The results for the normalization factor give a value of 0.185±0.005 for the first few resonances. In the assumption that the neutron flux used is correct, this factor represents the fraction of beam intercepted by the 1 cm diameter sample, and is consistent with the one expected from the simulation of the beam profile. It is

important to note here that, regardless of whether the assumed neutron flux is accurate, the product of the assumed flux with the normalization factor extracted from the fit of the Au resonances represents a reliable experimental value for the effective neutron flux, to be used in the determination of the Sm cross-section.

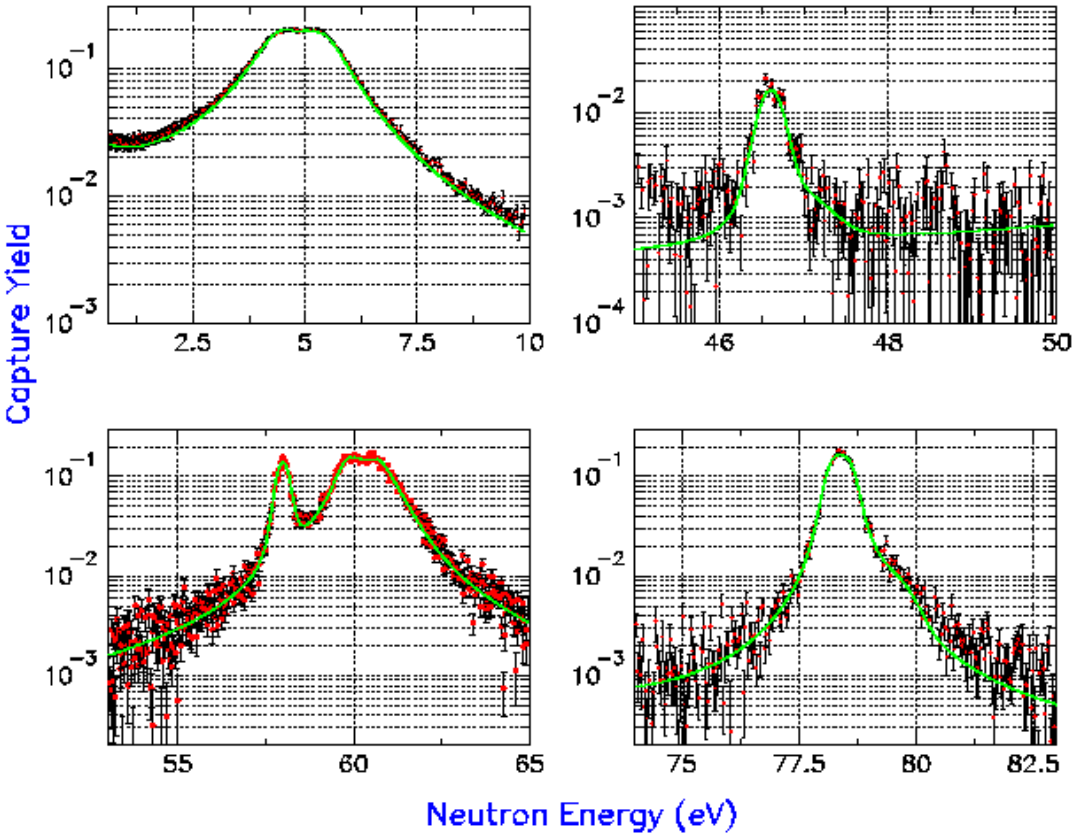

Figure 5.10: A fit of some resonances of Au performed with SAMMY (the symbols represent the experimental data, while the green curve shows the fit). The normalization of the neutron flux for all resonances is around 0.185±0.006.

A fit of the ^{151}Sm resonances was then performed. At first, the normalization factor was kept fixed to the value extracted from the Au analysis (0.185). A reasonable fit is obtained. However, a slightly smaller factor seems to give better results. From the fit of the first resonances of Sm, keeping the normalization factor free, a value 8% lower then the one obtained from Au is observed. The origin of this difference is still being investigated (it could be related to the effect of multiple scattering in Au, not considered in this analysis). Figure 5.11 shows the results of the SAMMY fit for some of the resonances of Sm. In general, the fits give a larger width for the resonances, relative to the expected ones (the only available cross-section for ^{151}Sm are the results of an evaluation, since no data on capture reactions have been reported up to now). Furthermore, it seems that at higher energy, the currently available resonance parameters are not able to reproduce the

experimental data, in particular the energy of the resonance, as shown in Figure 5.12, right panel. Multiple scattering, and other improvements in the input (sample composition, initial parameters, temperature for Doppler broadening, etc…). At the end, add a table with the extracted resonance parameters for Sm. More improvements in the normalization.

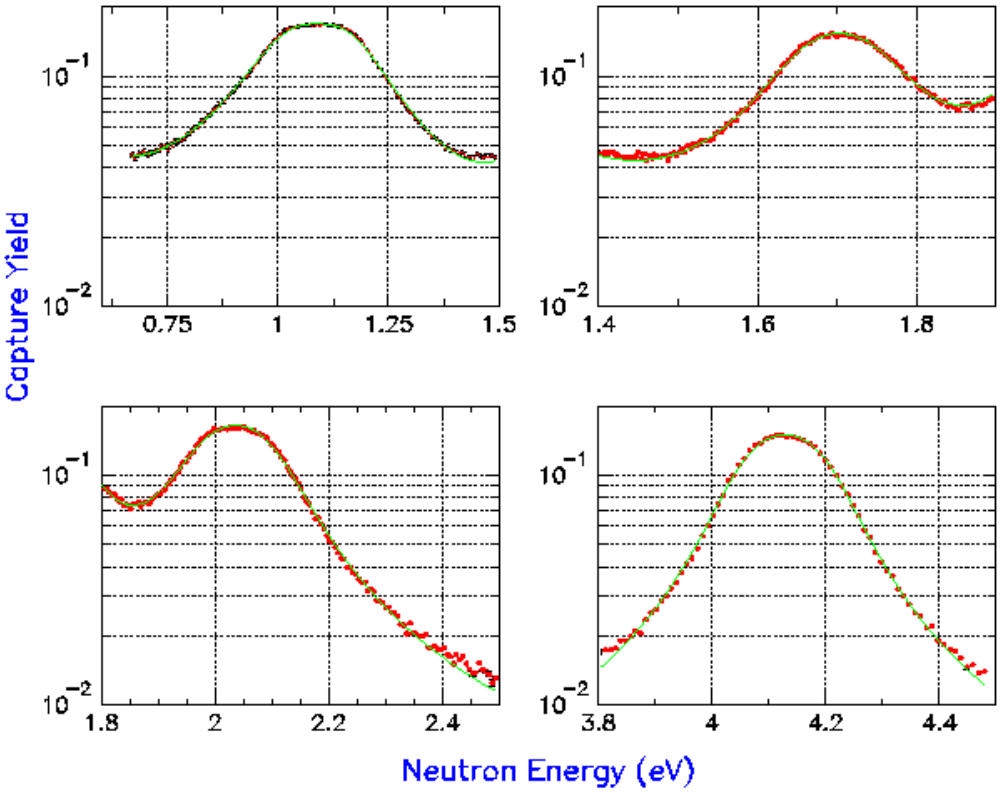

Figure 5.11: The ^{151}Sm experimental yield in the resonance region, fitted with SAMMY.

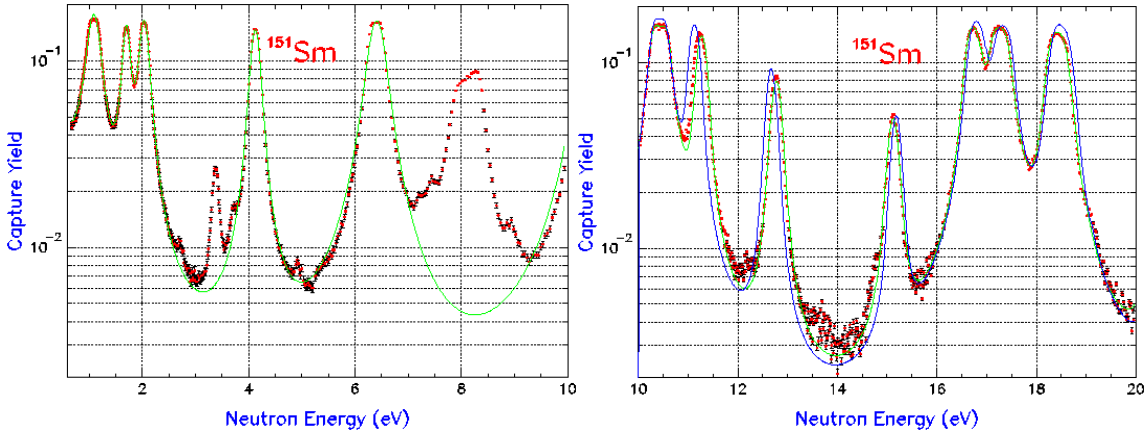

Figure 5.12: **A comprehensive view of the first resonances of ^{151}Sm with the SAMMY fit (left panel). Resonances from other isotopes are also present in the data. Right panel: higher energy resonances of Sm. The blue curve represents the yield extracted from the resonance parameters currently available in the ENDF/B-VI database. Some discrepancies in the energy of the resonances are observed.**

5.7 Analysis of the unresolved resonance region

The experimental determination of the cross-sections in the unresolved resonance region requires some additional considerations, due to the presence of a non-negligible background contribution related to in-beam γ-rays, which affects the region above 1 keV. Although a large reduction of this component was achieved by mounting the detectors at backward angle, and a further reduction results from the application of the Weighting Functions, a residual component still survives for the heavier samples (Au and Pb), as shown in a previous paragraph. While the background-free Sm_2O_3 spectrum can be simply obtained by subtracting the empty Ti-can measurement (after application of the WF), a different procedure needs to be followed for Au. The following steps have been applied in this case:

The in-beam γ-ray background in Pb was isolated by subtracting the empty Ti-can from the Pb spectrum (both corrected for the Au weighting functions);

The resulting yield distribution was scaled up by a factor of 1.55, estimated from the simulations, and added to the empty-can background. The resulting spectrum represents the overall (estimated) background for Au;

The resulting background is subtracted from the measured (and weighted) Au spectrum, to obtain a background-free Au distribution.

Figure 5.13, left panel, shows the experimentally determined yield for Au in the unresolved resonance region, between 5 keV and 1 MeV. The red curve represents the expected yield, extracted from the ENDF/B-VI database, scaled down by a factor of 0.18. This factor is obtained by fitting the ratio between experimental and predicted yield, shown in the right panel of Figure 5.13. As in the case of the low-energy region, in the assumption that the neutron flux used in the determination of the yield is accurate, the factor of 0.18 represents the fraction of the neutron beam intercepted by the samples of 1 cm diameter.

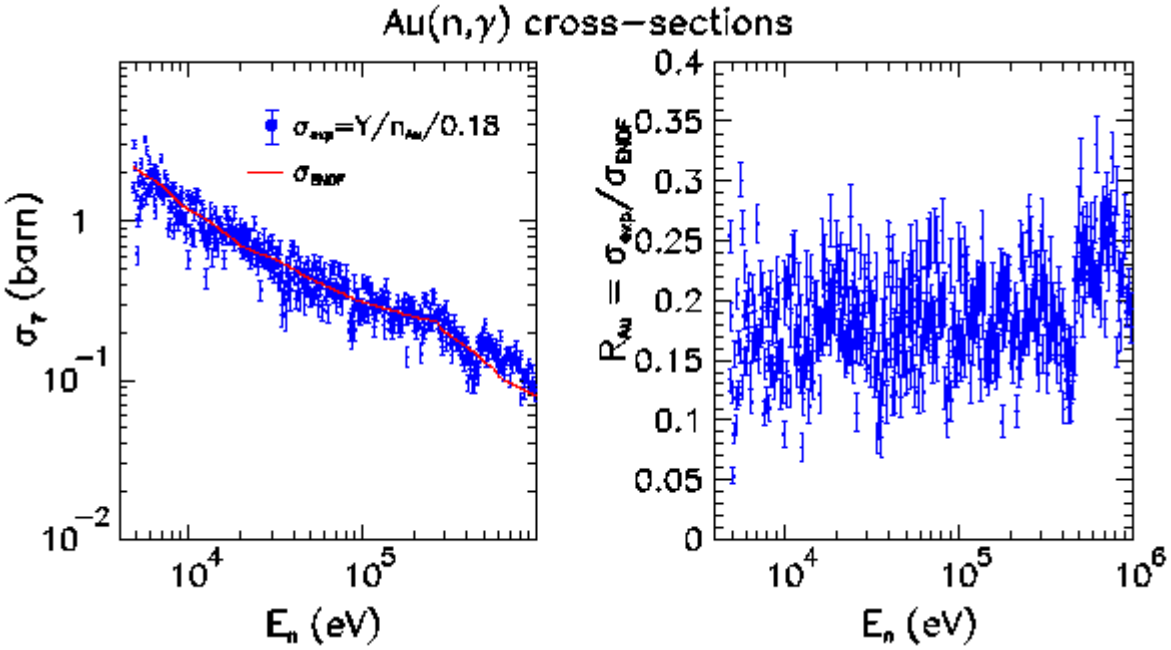

Figure 5.13: For the unresolved resonance region in Au, the extracted cross-section, after all background subtraction, is compared with the cross-section from the ENDF/B-VI database (left panel). A good match is obtained by assuming a fraction of the neutron flux of 0.18. The point-by-point ratio between measured and evaluated cross-sections is shown in the right panel. The large statistical fluctuations are associated with a poor statistics on Pb, needed to estimate the most important background component in the unresolved resonance region.

It is consistent to the one predicted from the simulations of the beam profile performed with Fluka, shown in Figure 5.14 [46], and comparable to the fraction determined from the resonance in the low-energy region (below 100 eV). It should be noticed that, to avoid the large statistical fluctuations associated with the Pb measurement, a parameterization of the corresponding background was used.

Figure 5.15 shows the extracted cross-section for the ^{151}Sm, obtained from the measured yield in the assumption of a thin sample (in this case, the cross-section is simply obtained by dividing the yield by the number of atoms/barn). In the left panel, the measured spectrum between 5 keV and 1 MeV is corrected for the constant factor of 0.18. The effect of some dips in the neutron flux is however still present in this case. For this reason, it is more accurate to employ an energy-dependent normalization factor extracted directly from the Au measurement. The right panel in Figure 5.15 shows the cross-sections obtained by dividing for the flux ratio obtained from the Au measurement (right panel of figure 5.13). Although the error bars are bigger in this case, due to the statistical uncertainty associated with the Au measurement, no more dips are observed, due to the point-wise estimate of the neutron flux. It should be stressed that the cross-sections extracted from the Au ratio are completely independent on the neutron flux, and therefore should not be affected by

systematic uncertainties related to the beam intensity and profile, nor to their energy dependence.

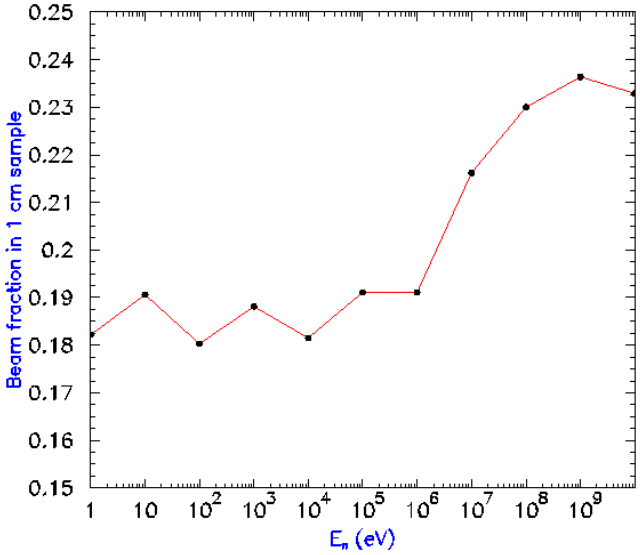

Figure 5.14: Fraction of the neutron flux intercepted by a circular sample of 1 cm diameter. These results are obtained from the simulation of the beam profile from Fluka (V. Vlachoudis, private communication).

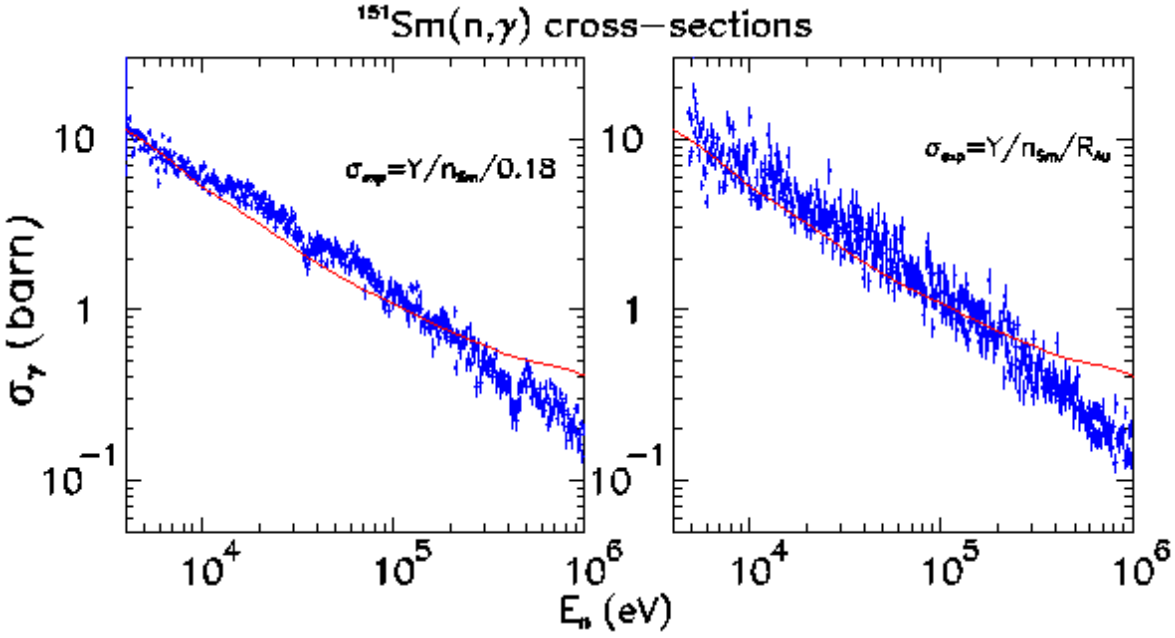

Figure 5.15: Left panel: extracted cross-section in the unresolved resonance region for ^{151}Sm, assuming the PTB neutron flux scaled down by a fixed factor of 0.18 (related to the sample dimension smaller than the beam profile). Right panel: the cross-sections are extracted by dividing the yield for the fraction extracted from Au, shown in the right panel of figure 8. In both panels, the red curves represent the cross-sections from the ENDF/B-VI database.

A comparison with the cross-sections tabulated in the ENDF/B-VI file for ^{151}Sm is shown in the figure. The experimental results are slightly higher than predicted, up to 100

keV, and lower than expected above this energy. As a cautionary note, it is still possible that a background component may still be present in the region of 10-100 keV. However, on the basis of the simulations, it can be safely concluded that the in-beam γ-background can be neglected for the Sm_2O_3 sample. A careful check, based on the measurements with the filters, leads to the conclusion that …

5.8 Conclusions

Preliminary results for the cross-sections of ^{151}Sm have been obtained both in the resolved and unresolved resonance region. A combination of measurements and Monte Carlo simulations, demonstrate that the background affecting the Sm_2O_3 sample is purely the one measured with the empty Ti-can. By subtracting the relative spectra, both weighted for the Sm_2O_3 weighting functions, the background-free ^{151}Sm spectrum has been obtained.

The neutron flux crossing the sample has been extracted from the Au sample, after subtraction of the estimated relative background (a non-negligible contribution of the in-beam gamma-background exists for this sample). In the resolved resonance region, the neutron flux has been estimated from a fit of the capture yield performed with SAMMY. The analysis of a saturated resonance in ^{151}Sm gives the neutron flux consistent (although slightly lower) with the one extracted from the fit of the Au resonances, confirming the accuracy of the flux determination.

In the unresolved resonance region, the neutron flux has been extracted from the ratio of the experimental Au yield, to the ones predicted from the ENDF-B/VI file. A careful analysis of the in-beam γ-background has to be performed in this region. In the present measurement, a Pb measurement has been used to subtract the additional component.

The results at low energy indicate that some corrections to the tabulated resonance width and energy (above 10 eV) are needed. In the unresolved resonance region, the cross-sections show a different behavior than expected, with differences up to 30%.

Appendix I

1.1 Pulse Shape Analysis of the liquid scintillators

Liquid scintillator detectors are widely employed in studies with fast neutrons and γ-rays [48]. Several properties make such detectors very appealing: the relatively high light-output, a reasonably good efficiency for fast neutrons and the fast decay time of the light output. The last feature is particularly useful in those studies where timing information is required as well as in measurements characterized by high-count rates. Furthermore, an additional slow component, which depends on the energy loss density, makes common liquid scintillators suited for neutron/γ discrimination. Several methods can be used for this purpose. In one of them, information on the particle type is obtained from the zero-crossing time of the suitably shaped signal [49]. Alternatively, double charge integration can be used, with the two integration gates chosen so as to extract the relative contribution of the slow component versus the total light output [50]. The performances of the two methods have been extensively analyzed and compared, even in the presence of pile-up, while a new pattern recognition method has also recently been proposed [51].

For n_TOF, a different solution has been investigated. It relies on the acquisition of the complete waveform of the liquid scintillator signals by mean of a Flash-ADC (FADC). The recorded waveforms can later be analyzed to extract particle type and energy, to obtain timing information and to resolve overlapping signals.

Figure A.1 shows a typical signal produced in the NE213 by the ^{60}Co source, as recorded with the FADC, at 1 GSample/sec sampling rate (solid symbols). For timing information, the start of the signal was defined, consistent with the operation of Constant Fraction Discriminators (CFD), as the time when the signal reaches a fixed fraction of its maximum, in this case 20%. This definition seems appropriate also in fitting procedure described later. As shown in Knoll [52], the signal shape from scintillation detectors can be obtained by convoluting the exponential decay spectrum of the scintillator with the response function of the photomultiplier tube and readout system. For the case of a single decay time, this results in the difference between two exponential terms, one of which

related to the equivalent *RC* time constant of the anode, connecting cable and input stage of the FADC, and the other to the decay constant of the scintillator light output. In the case of liquid scintillators, however, a fit with only two exponential terms does not give satisfactory results, especially at times greater than 50 ns, as shown by the dashed curve in the figure. This is not unexpected because of the characteristic slow decay component of liquid scintillators. It is therefore necessary to add a second exponential decay, convoluted with the response function of the system, to account for the longer tail in the signal. A more accurate reproduction of the pulse shape can be obtained with the functional form:

$$L = A\left(e^{-\vartheta(t-t_0)} - e^{-\lambda_s(t-t_0)}\right) + B\left(e^{-\vartheta(t-t_0)} - e^{-\lambda_l(t-t_0)}\right). \qquad \text{(A.1)}$$

The use of the additional free parameter t_0 is necessary for time reference. A fit according to Equation A.1 with six free parameters (A, B, t_0, ϑ, λ_s, λ_l) is CPU time consuming and does not always easily converge to the best solution. To simplify and stabilize the fitting procedure, it would be desirable to reduce the number of free parameters by identifying their single best values or finding relations among them. For this purpose, the following procedure can be used:

1) a significant number of events are fitted with Equation (A.1) keeping all six parameters free;
2) the distribution of the three exponential decay constants is determined and an average value is extracted for these parameters;
3) keeping the three exponential decay constants fixed events, the events are fitted again searching only for the time reference t_0 and the normalization parameters: A and B;
4) an average value is chosen for t_0 and a relation between A and B is found, so that all events can be fitted with only one normalization constant.

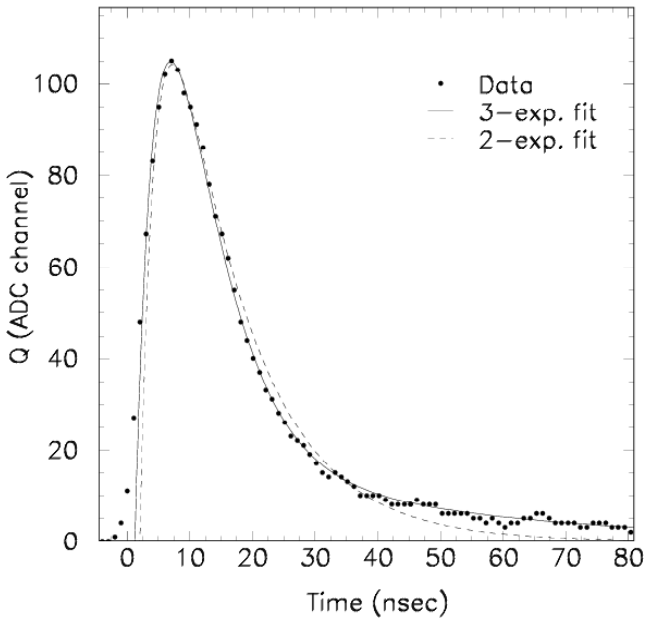

Figure A.1: Signal emitted by a ^{60}Co source recorded by NE213 coupled to a FADC. The solid line depicts the result of the fitting with a three exponential while the dashed line indicates the two-exponential terms in Equation A.1.

As a result of the application of this procedure, one free normalization parameter remains and Equation (A.1) for γ-rays can now be written as:

$$L = A\left(e^{-(t-0.31)/5.578} - e^{-(t-0.31)/4.887} + 0.0166e^{-(t-0.31)/34.276}\right)$$

This approach is also used to fit the signal described in the C_6D_6 detector. The values of the exponential decay times found for the scintillator are: $1/\vartheta$=4.264 nsec $1/\lambda_s$=3.886 nsec and $1/\lambda_l$=50.73 ns; they do not differ from the known physical properties of the C_6D_6 and are comparable to the values of the NE213 detector. A larger difference is observed for the tail content, being the value of the normalization constant B/A=1.472×10^{-3}, nearly a factor ten lower.

The procedure followed for γ-rays can be repeated for neutrons in order to find the best shape parameters for this type of signals. In principle, one may find different values for all 5 fixed parameters (the three decay constants, t_0 and the contribution of the slow component). It was verified, however, that the procedure applied to neutrons leads to essentially the same three exponentials as for γ-rays, while a significant change is observed only for the contribution of the third term. Since the decay constants of the scintillator do not depend on the particle type, the only expected difference between γ-rays and neutron-induced signals is due to the relative contributions of the fast and slow components. For the Am/Be source, the first step of the procedure can be skipped by assuming the same decay

constants as for the ^{60}Co source. The 3-parameter fit reveals two branches in the *A*-*B* plane or equivalently the projection of *B/A* ratio shows two peaks in the distribution (Figure A.2). The first peak corresponds to the distribution obtained from the ^{60}Co source and related to γ-rays, the second peak corresponds to the neutron events, the average ratio for neutrons are $B/A=4.151\times10^{-2}$ compared to 1.658×10^{-2} of the γ-source, a factor 2.5 lower.

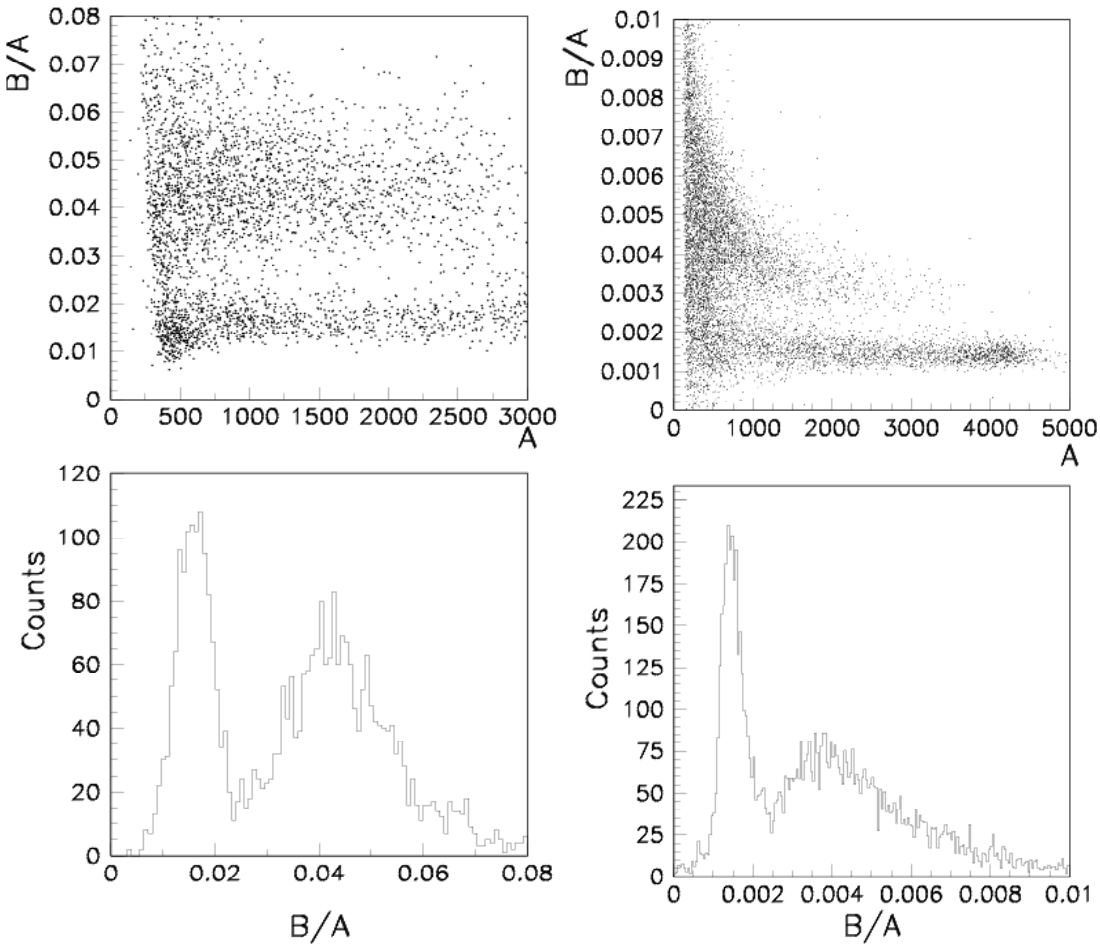

Figure A.2: Correlation between the normalization constants *A* and *B* for events from the Am/Be source detected in NE213 (left graphs) and C_6D_6 (right graphs). Upper branch in B vs A graph corresponds to neutron, lower branch represents the γ-rays. In bottom panel equivalently, first peak corresponds to the neutron while second peak is referred to the γ-ray.

The n/γ discrimination is based on a comparison of the χ^2 values obtained with parameters found for neutrons and γ-rays signals. For each event, two fits are performed with the shape function of γ-rays and neutrons respectively. The difference $D = \chi_n^2 - \chi_\gamma^2$ of the corresponding normalized χ^2 values is expected to be negative in a case of a γ-ray and positive for a neutron. Figure A.3 shows the difference for events recorded in NE213

scintillator from the Am/Be source; the shaded area represents the same difference for the ^{60}Co source.

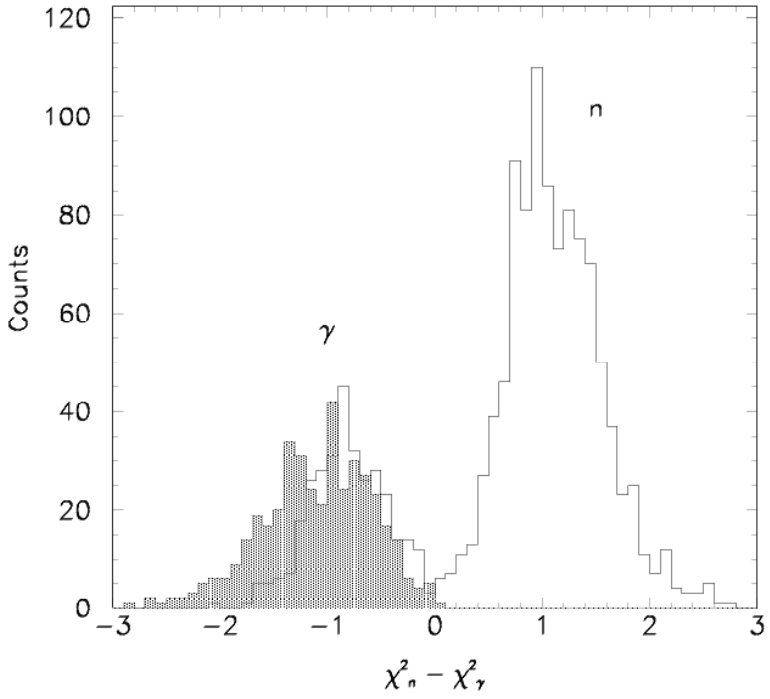

Figure A.3: Difference between the normalized χ^2 obtained by fitting the signals from the NE213 detector with the shape functions corresponding to the neutrons and to the γ-rays. The dashed area represents the n/γ-ray pattern for a ^{60}Co source.

The main advantage of using FADC for acquisition of signals from liquid scintillators resides in the possibility to identify and to reconstruct pile-up events. Contrary to other hardware-based methods, the analysis of the entire pulse waveform in the presence of the pile-up should in principle allow to disentangle the two overlapping signals and to provide reliable information on type and energy of both particles. The method consists in fitting the first signal up to the start of the second one; the analytical function extracted from the fit is subtracted isolating the second signal, which can then be separately analyzed. The reconstruction of pile-up events depends primarily on the time separation between the two signals, i.e. on the range in which the fit of the first signal can be performed. In order to check the accuracy of the method for pile-up reconstruction, a large number of pile-up events were generated starting from individual signals recorded with the ^{60}Co source. Pairs of single events were randomly chosen and added together with a time separation varying between 20 and 100 ns in steps of 20 ns (the two individual signals were also separately kept for comparison). First, a pile-up event is identified and the time separation between the signals determined. The adopted criterion requires that two maxima are detectable within 250 ns after the start of the first signal (after this period the first signal has decayed to a

negligible level, so that the occurrence of a second signal does not constitute a pile-up event). After determining the position t_2 of the second maximum, a fit of the first signal is performed up to the start of the second one. The resulting analytical function is then subtracted from the original event, so that a fit of the remaining signal can be performed. Figure A.4 (left panel) shows the result of this procedure for signals separated by 20 and 60 ns, respectively. The accuracy of the pile-up identification and separation can be inferred, as before, by comparing the analytical integral of the fitting function L_f with the numerical integral of the two original signals L_0 (Figure A.4 right panel), Obviously, the uncertainty of the reconstruction is particularly large for small time differences, since the second signal is strongly affected by the tail of the first one. However, a separation of 40 ns seems to be sufficient to ensure the reliable analysis of both signals. Although a more detailed analysis should take into account, together with the time separation between signals, their relative amplitude, the results here shown provide some indications on the capability of the method to reconstruct pile-up events.

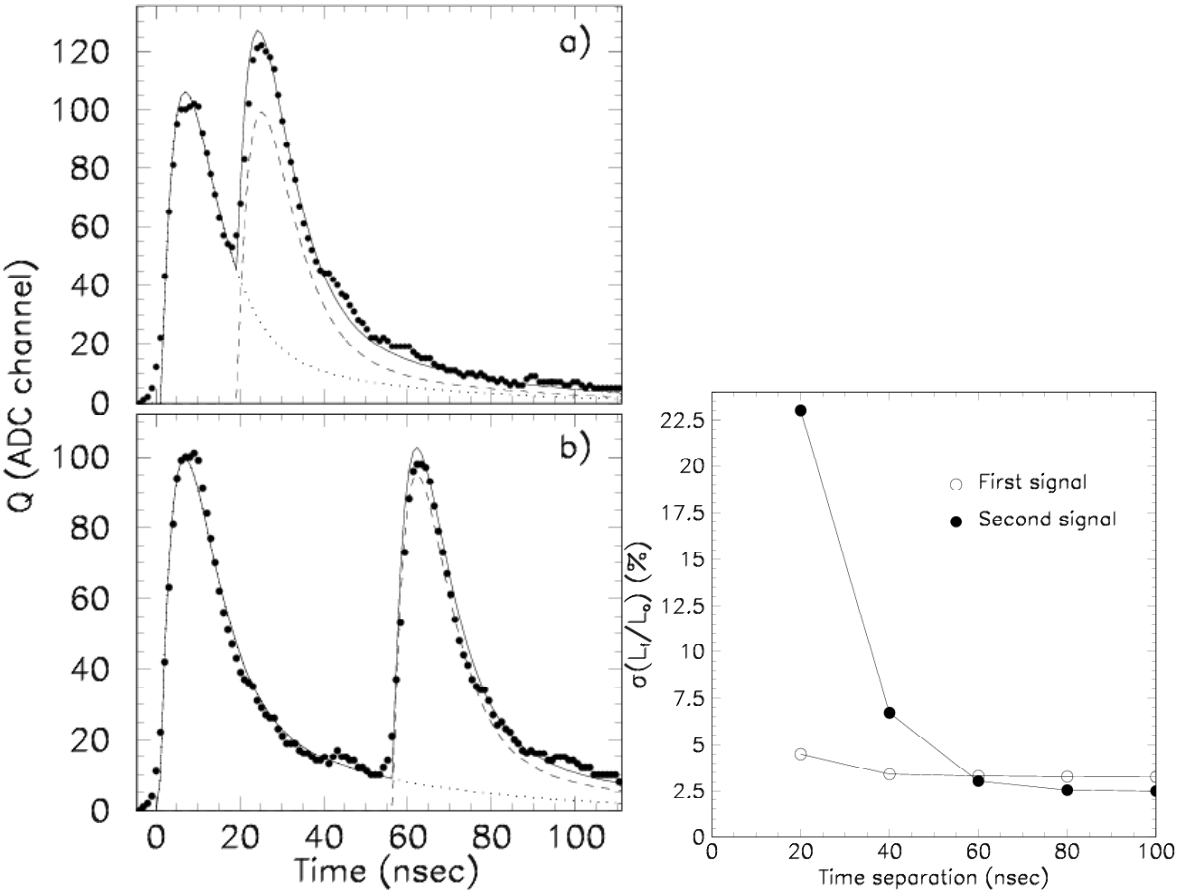

Figure A.4: On the left, software generated pile-up events for signal separations of 20 and 60 ns. Solid line represents reconstructed pile-up pulse, dotted and dashed lines represent the first and the second pulse. In the right panel, the standard deviation of the ratio between the total charge of the reconstructed signal and of the original signal for the first and second pulse.

1.2 Heavy Inorganic Scintillators

In this section the pulse shape method is applied to analyze the signals produced in two inorganic scintillators: BaF_2 and CeF_3. Heavy inorganic scintillators have completely different properties relative to the liquid organic scintillators. They are sensible to the γ-rays and have relatively low cross sections for neutron capture. The typical design used for this detector is a "soccer-ball" array highly segmented and subtending the whole solid angle. In that way, all photons of the cascade produced in neutron capture reaction can be detected. Some experiments of nuclear physics at CERN and LANL are planning to use 4π calorimeter for their measurements, for further details see § 3.7.

Table A.1: Properties of scintillator materials.

Scintillator(g/cm^3)	***Component***	***Decay Time***	***Wavelength***	***Photons/MeV***
CeF_3 (6.16)	Fast	3 ns	300 nm	200
	Slow	27 ns	340 nm	4,300
BaF_2 (4.88)	Fast	0.6 ns	180 nm	1,800
	Slow	630 ns	310 nm	10,000

The characteristics and properties of scintillation light in BaF_2 and CeF_3 are well known since many years and are briefly listed in Table A.1. Because of a very fast response and high efficiency, the BaF_2 is used in γ-ray spectroscopy. Furthermore, the high light-output and the relative simplicity of manufacturing large crystals make this scintillator very convenient for the calorimeter construction. The CeF_3 instead has a lower light yield and it is difficult to grow in long crystals (1000 cm^3 or more) but has the advantage of the short tail (the slow component is 27 nanoseconds decay time) while BaF_2 presents a much longer tail (slow component of 600 nanoseconds decay time). The characteristic signals recorded by a FADC are indicated in Figure A.5.

The procedure applied to reconstruct this signal is the same as in liquid organic scintillator case, but obviously a different analytic function has to be used in this case. The function applied for BaF_2 is a pure exponential and needs to interpolate only the one-tail exponential of the BaF_2 signal while in CeF_3 case the function is a two-tail exponential as:

$$L = \alpha_s \, exp(-t/\tau_s) + \alpha_R \, exp(-t/\vartheta);$$

where τ_s is the time constant, ϑ is the inverse of *RC* constant and α_s, α_R are the relative normalization constants. The values of parameters extracted for two scintillators are reported in Table A.2. In CeF_3 case, the signals are recorded with and without the

application of a Timing Filter Amplifier (TFA) module (Figure A.5), the parameters extracted refers to these two signals.

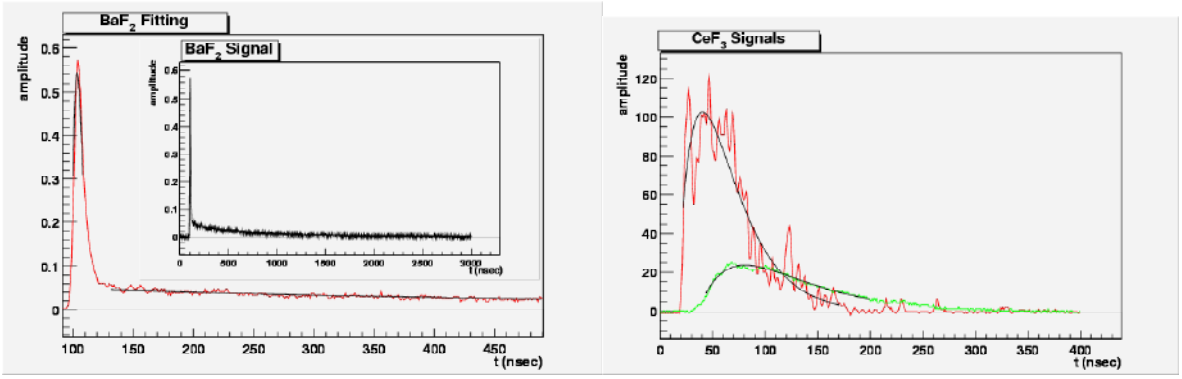

Figure A.5: Typical BaF_2 signal is represented on left panel; the tail is fitted with one-exponential while the peak with a three-exponential. The CeF_3 is shown on right panel; red curve represents the signal acquired without Timing Filter Amplifier (TFA), green curve is the signal recorded with TFA in electronic chain.

Table A.2: Parameters extracted from the fitting functions.

Function	ϑ (ns)	α_s	τ_s(ns)
BaF_2 (1)			638. ± 33.25
CeF_3 (2.1) no TFA	21.4 ± 1.37	7926 ± 164	20.57 ± 1.06
CeF_3 (2.1) with TFA	50.12 ± 3.32	107. ± 10.1	23.65 ± 3.

Inorganic scintillators are not able to discriminate in a direct way neutron from γ-rays particles; neutrons are detected mainly though capture and consequent emission of γ-ray in the crystal. The background in this detector is discriminated analyzing the energy deposition of the γ-cascade in the whole calorimeter.

As for liquid scintillator, pile-up events are investigated following the same procedure as before. Two signals, arbitrarily chosen, are summed channel by channel (Figure A.6). The sum is performed with different time separations; in this way it is possible to verify what is the minimum distance necessary for a correct resolution of the two pulses as in Figure A.4. Figure A.7 shows the ratio between the areas of the reconstructed second pulse evaluated numerically to the original one. The results indicate clearly that the longer the time interval between the peaks, the better the resolution of the two pulses. The plot illustrates the good performances of the pulse shape method also for inorganic scintillators. The fitting method allows to resolve a pile-up for time separations larger than 500 ns.

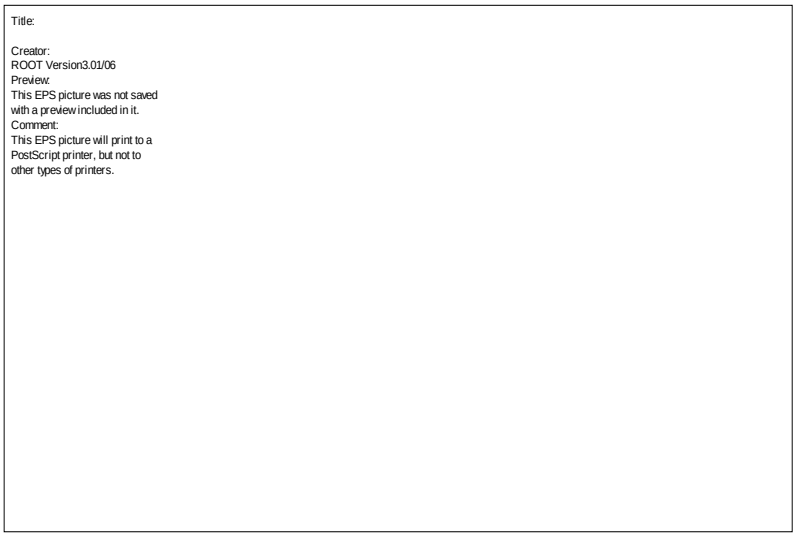

Figure A.6: Pile-up event in BaF_2 crystal.

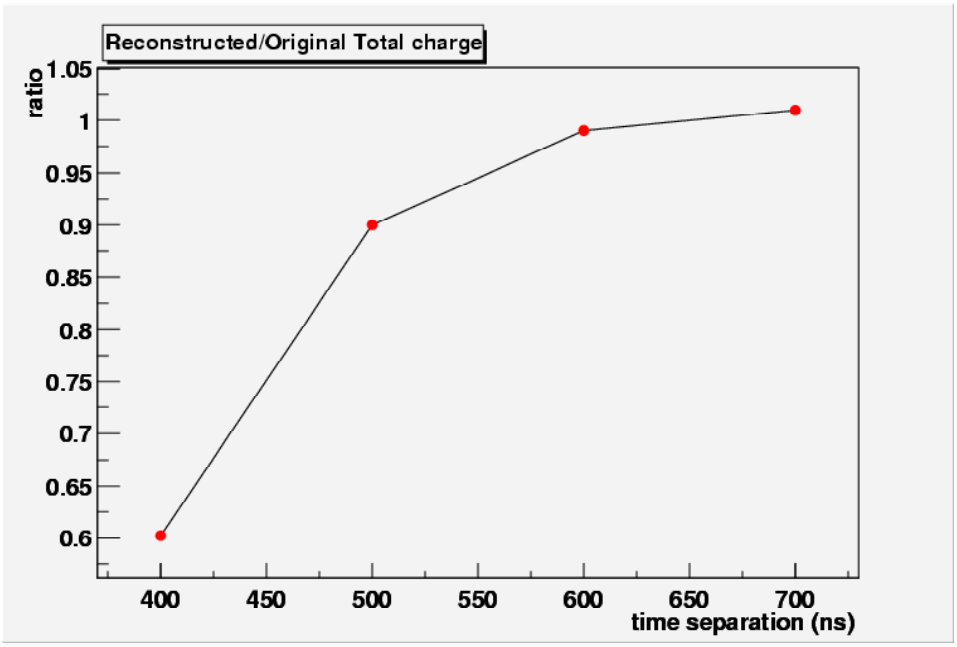

Figure A.7: The ratio as function of the time separation represents the area of fitted signal to the area of the original one; the pulse is recorded in BaF_2 crystal and for pile-up events. It is evident that the fitting procedure allows to resolve correctly two pulses for time separations larger than 500 ns.

Appendix II

2.1 Overview

The software program SAMMY (written in Fortran) is a multilevel and multichannel *R*-matrix code originally used for the analysis of the neutron reaction data at Oak Ridge Electron Linear Accelerator (ORELA). The first version was released in 1980 [53] on the basis of a previous code named MULTI developed by G. Auchampaugh [54]. The code allows to fit the data in order to extract the cross-sections in unresolved resonance region and/or the resonance parameters in the resolved resonance region.

SAMMY can analyze a wide spectrum of nuclear reactions having:

i. *Incident Particles:* protons, neutrons and α-particles;
ii. *Target:* single and multiple isotopes, chemical compounds and contaminants;
iii. *Types of data:* Total, elastic, capture, fission, inelastic cross-sections, integral data and angular distributions for elastic cross-sections.

There are many codes that allow to fit the resonances and to determine the cross sections as MULTI, REFIT etc. SAMMY results more reliable relative to similar codes because several features are included:

1) SAMMY uses Bayes' method for fitting procedure while other codes use least-squares method;
2) The Reich-Moore formalism is used and is extended to include an optional logarithmic parameterization of the external *R*-matrix, for which any or all parameters may be varied;
3) The possibility to vary sample thickness, effective temperature, matching radius has been incorporated;
4) Several types of corrections for experimental effects are included as: three versions of Doppler broadening, four resolution neutron beam functions, self-shielding, multiple scattering and finally normalization constant;
5) To avoid loss of information (i.e., computer round-off errors) between runs, the "covariance file" includes precise values for all variables;
6) Unused but correlated variables may be included in the analysis.

In next sections, we briefly describe the implementation of the Bayesian method and the Reich Moore approximation. Finally we describe the resolution broadening necessary to include the experimental effects induced by the facility.

2.2 Bayes' method

Bayes' theorem can be written in the form:

$$p(P/DX) = p(P/X) \cdot p(D/PX),$$

where P represents the parameter vector of the theory, D the experimental data and X is the prior knowledge of the parameters that we want to determine (P) while $p(P/X)$ is prior probability density function for parameters, $p(D/PX)$ is the probability density function for observing data D and $p(P/DX)$ is the posterior probability density function. The three basic assumptions made in order to solve the Bayes' equation are [55]:

a) Prior joint probability density function is a joint normal;
b) Likelihood function is a joint normal;
c) True value is a linear function of the parameters.

The final form of the equation in the NPV inversion scheme is:

$$P' - \overline{P} = MG'(N+V)^{-1}(D - \overline{T}),$$

where $T(P)$ is the joint normal distributions of the parameters P with corresponding expectation value $\overline{T}$ and the covariance matrix V; G is the matrix of the partial derivatives of T respect with P while $\overline{P}$ and M are respectively the expectation value and the covariance matrix of the prior joint probability density function, N is defined as: $N = GMG'$, P' represents the solution for the parameters vector G' the value of the matrix calculated in P'. More algebraic details on this derivation are illustrated in reference [55]. Because the linearity condition c) may be only approximately correct it is necessary to iterate the procedure in order to find more accurate solution. We have also to note that this is not the only possible derivation of Bayes' equation but it is the iterative form, which is implemented in SAMMY.

2.3 Reich-Moore's approximation

The angle integrated cross-sections from entrance channel c to c' exit channel with total angular momentum J is represented by $\sigma_{cc'}^{J}$ which in turn is given in terms of scattering matrix $U_{cc'}^{J}$ as:

$$\sigma_{cc'}^{J} = \frac{\pi}{k_c^2} g_c \left| \delta_{cc'} - U_{cc'}^{J} \right|,$$

where k_c is the wave number associated with the incident channel and g_c is the spin statistical factor. From this formula is possible to derive the expressions for total, elastic, reaction and capture cross-section as function of U-matrix. The scattering matrix can be written in terms of the W matrix as [56]:

$$U_{cc'}^{J} = \Omega_l W_{cc'}^{J} \Omega_{l'},$$

where l represents the orbital angular momentum and $\Omega_l = e^{-i\varphi_l}$; φ_l expresses the potential scattering phase shift. The final expression for the scattering matrix is:

$$U_{cc'} = \Omega_l \left[\delta_{cc'} + i \sum_{\mu\lambda} \Gamma_{\mu c}^{1/2} A_{\mu\lambda} \Gamma_{\mu c'}^{1/2} \right] \Omega_{l'},$$

being A the level matrix defined as:

$$A_{\mu\lambda}^{-1} = \left(E_\lambda - E\right)\delta_{\mu\lambda} - \sum_c \gamma_{\mu c} L_{0c} \gamma_{\lambda c},$$

where $\gamma_{\lambda c}$ is the reduced width amplitude while $L = \left(S - B\right) + iP$ is defined as the shift factor S minus boundary condition B plus the penetrability P in the imaginary part of the complex plane. The level matrix is linked to the reaction R-matrix by the following expression:

$$\left[\left(I - RL_0\right)^{-1} R \right]_{cc'} = \sum_{\mu\lambda} \left(\gamma_{\mu c} \gamma_{\mu c'}\right) A_{\mu\lambda}$$

The Reich-Moore approximation consists in set to zero the off-diagonal contributions of photon channels ($c \in \gamma$) or in formula:

$$\sum_{c\in\gamma} \gamma_{\mu c} L_{0c} \gamma_{\lambda c} = \delta_{\mu\lambda} \sum_{c\in\gamma} \gamma_{\mu c} L_{0c} \gamma_{\lambda c} = \frac{i}{2} \delta_{\mu\lambda} \Gamma_\lambda^\gamma,$$

Substituting this expression in U scattering matrix, the reaction matrix R becomes:

$$R_{cc'}^{J} = \sum_\lambda \frac{\gamma_{\lambda c} \gamma_{\lambda c'}}{E_\lambda - E - i\Gamma_\lambda^\gamma / 2},$$

where the sum is performed on all levels with total spin J. The final formula for the capture cross-section in terms of the resonance parameter is:

$$\sigma^{capture} = \frac{\pi}{k^2}\sum_J g_J \sum_{\text{incident channel}} \left(Im\left(X^J_{cc}\right) - \sum_{\text{all channel}} \left|X^J_{cc'}\right|^2 \right),$$

where X is defined by:

$$X = P^{1/2} L^{-1}\left(L^{-1} - R\right)^{-1} R P^{1/2}.$$

This is the capture cross-section formula implemented in SAMMY for the fitting of neutron capture data.

2.4 Other experimental effects

The Reich-Moore Approximation together with the Bayesian theory constitutes the fundamental ingredient in SAMMY's fitting procedure. Nevertheless there are several experimental effects that largely contribute to the determination of the resonance parameters and merit to be mentioned.

The most important ones are surely Doppler broadening and neutron beam resolution broadening. The Doppler broadening depends on the nuclei motion within the sample; they are not placed in a fix position but exhibit a random thermal motion. This thermal motion is described in SAMMY through two theoretical models: Crystal lattice and Free Gas model [57]. The latter one is the most used and works in most physical situations even for heavy nuclei.

The second effect is the resolution function of the facility. It is a very delicate aspect connected to the characteristics of the neutron beam and of detectors and necessitates of a careful study. The main components contributing to this kind of broadening are: the width of the primary beam (proton in n_TOF case), the moderator, the neutron detector and the time-of-flight channel width. In SAMMY, three resolution functions are implemented. The gaussian resolution is the most common and simple. The second one is ORELA resolution function that is implemented according to the characteristic of the ORELA facility [58]. The last one is the RPI resolution function that is adapted to the characteristic of the Rensselaer Polytechnic Institute [59]. Those functions result inadequate to reproduce the characteristics of the n_TOF neutron beam and therefore a new function will be implemented in the code in order to correct these effects in the final evaluation of the cross-sections and of the resonance parameters.

References

[1] E. M. Burbidge, G.M. Burbidge, W.A. Fowler, F. Hoyle Review of Modern Physics, Vol. 29 num. 4.

[2] C. Rubbia et al., CERN/AT/95-53 (ET);

[3] R.V.Wagoner, Astrophysical Journal 179, 343;

[4] F. Käppeler, Proceeding of the CEA-EC-GEDEON-NEA/OECD Workshop 21-22 September, CERN, Geneva;

[5] Iben and Renzini, Annual Review Astron. Astrophys. 21, 271;

[6] D.D. Clayton, "Principles of stellar evolution and nuclesoynthesis", McGraw-Hill, NewYork;

[7] A.G. Cameron, Chalk-River Report, CRL-41, 1957;

[8] Truran et Cameron, Astrophysical Journal 216, 797;

[9] NEA Annual Report 2001, see on website www.nea.fr;

[10] Ads review

[11] S.F. Maughbghab, M. Divadeenam and N.E. Holden, Neutron Cross sections V.1 Part A, Zz 1-60 Academic Press Inc., 1981;

[12] "The NEA High priority Nuclear Data Request List", Status in May 1998, OECD-NEA Nuclear Science Committee;

[13] M.B. Chadwick et al., Rad. Protection Dosimetry, Vol. 70 (1997), p1;

[14] G.A. Miller, B.M. Nefkes and I. Slaus, Phys. Report 194 (1990), 1;

[15] T. Goldman et al., Few Body Systems, 1992;

[16] A. Bondar et al., Phys. Lett. B(356) (1995);

[17] H. Feschbach, "Theoretical Nuclear Physics, Nuclear Reactions", ed. Wiley 1992, New York;

[18] M. Strutinsky, Nuclear Physics A95 (1967), 420;

[19] S. Kopecki et al., Physical Review Letter 66, (1991), 1015;

[20] V.E. Krohn and R.G. Ringo, Physical Review D 8 (1973), 1305;

[21] R.M. Thaler, Physical Review 114 (1959) 827;

[22] Technical Design Report; The Muon Project,m CERN/LHCC/97-32, CMS TDR3 (15 December 1997);

[23] Hilscher

[24] P.W. Lisowski, C.D. Bowman, S.A. Wender, and G.J. Russell, Nucl. Sci. Eng. **106** (1990) 208;

[25] Oak Ridge National Laboratory Review (Vol. 26, No. 1),;

[26] K.H. Bockoff, Proceeding of an Advisory Group Meeting on Properties of Neutron Sources, Leningrad, USSR, 9-15 1986 Published IAEA Tecdoc 410, 1987;

[27] S. Andramonje et al., "Feasibility study of a Neutron TOF Facility at the CERN-PS, CERN/PS 98-065 (CA), Geneva 5 November 1998;

[28] TARC Collaboration, CERN-SL-2001-033 EET;

[29] A. Fassò, A. Ferrari, J. Ranft, P.R. Sala, G.R. Stevenson, J.M. Zazula: Proceedings of the 1st workshop on Simulating Accelerator Radiation Environment (SARE 1) Santa Fe, New Mexico, Los Alamos Report LA-12835-C, 1994;

[30] F. Carminati et al., "TARC General purpose MonteCarlo", CERN Internal Report CERN/LHC/EET 96-011, Geneva, 17 April 1996;

[31] C. Borcea et al, "The Neutron Time of flight facility at CERN", Proceedings 8th International Seminar on Interaction of Neutron with Nuclei, Dubna Russia, 17-20 May 2000;

[32] Proposal for a Neutron Time of flight Facility, CERN-SPSC 99-8, SPSC/P 310, 17 March 1999;

[33] V. Vlachoudis et al., SL-Note-2000-029 EET;

[34] J. Pancin private communication 2002;

[35] For Evaluated Neutron Data File see website www.nndc.bnl.gov;

[36] J.L. Tain et al., "Accuracy of the Pulse Height Weighting Technique for Capture Cross section Measurements", Proceedings of the Conference "Nuclear Data for Science and Technology", October 7-21, 2001 Tsukuba (Japan);

[37] F. Corvi et al., Nuclear Science and Engineering: 107, 272-283 (1991);

[38] N. Yamamuro et al., NIM A 133 (1976) 531-536;

[39] Manual of Sammy code version 6 beta ORNL N.M. Larson;

[40] n_TOF Collaboration: "Study of the Background in the measuring station at the n-TOF facility at CERN: Sources and Solutions"; CERN-INTC 2001-038, 6 December 2001;

[41] A. Ferrari et al., "A comprehensive study of the n-TOF background", SL-EET note 2001-036;

[42] For further details see website www.canberra.com;

[43] H.G. Hughes et al., MCNPX –The LAHET/MCNP code Merger, X-Division Research Note XTM-RN(U) 97-012, LA-UR-97-4891, Los Alamos National Laboratory (April 1997);

[44] SL/ECT, n_TOF neutron fluence with the PTB fission chamber, Internal Note SL/ECT 2002

[45] S. Andriamonje et al., Neutron TOF Facility, Technical Design Report, CERN/INTC/2000-004

[46] V. Vlachoudis private communications;

[47] N. Colonna et al., "In-beam photons as a source of background in capture measurements with C_6D_6 at the n_TOF facility", *Internal note, Ba/02/01, Bari, Jan 7th, 2002*

[48] H. Laurent et al. NIM A326 (1993) 517;

[49] P. Sperr et al. NIM A 116 (1974) 55;

[50] J.A. Adms, G. White, NIM A 156 (1978) 459;

[51] K. Kamanda et al., NIM A 426 (1999) 497;

[52] G. Knoll, Radiation Detection and Measurements, 3rd edition Ed. Wiley, New York, 2000.

[53] N. M. Larson and F. G. Perey, User's Guide for SAMMY: A Computer Model for Multilevel R-matrix Fits to Neutron Data Using Bayes' Equations, ORNL/TM-7485, ENDF-297, Oak Ridge National Laboratory, November 1980.

[54] George F. Auchampaugh, MULTI, A FORTRAN Code for Least-Squares Shape Fitting of Neutron Cross-Section Data Using the Reich-Moore Multilevel Formalism, LA-5473-MS, Los Alamos Scientific Laboratory, 1974;

[55] N. M. Larson, User's Guide for BAYES: A General-Purpose Computer Code for Fitting a Functional Form to Experimental Data, ORNLiTM-8185, ENDF-323, Oak Ridge National Laboratory, August 1982.

[56] F.H. Foderaro, "The Elements of Neutron Interaction Theory", MIT Press Cambridge MA and London (1971);

[57] N.M. Larson, M. C. Moxon, L. C. Leal, and H. Derrien, Doppler Broadening Revisited, ORNL/TM-13525, Oak Ridge National Laboratory,. 1998.

[58] D. C. Larson, N. M. Larson, and J. A. Harvey, ORELA Flight Path I: Determinations ofhs Effective Length vs Energy, Experimental Energies, and Energy Resolution Function and Their Uncertainties, ORNLiTM-8880, Oak Ridge National Laboratory, June 1984.

[59] Brian E Moretti, Molybdenum Neutron Transmission Measurements and the Development of an Enhanced Resolution Neutron Target, Ph.D. Thesis in Nucl. Engineering & Science, Rensselaer Polytechnic Institute, Troy NY, August 1996.

[60] D.B. Gayther, “International Intercomparison of Fast Neutron Flux-Rate Measurements Using Fission Chamber Transfer Instruments”, Metrologia 27, 221-231 (1990);

[61] Y. Kadi “Lectures at the Workshop of Nuclear Data for Science and Technology” ICTP, Trieste 18 Settembre 2001;

[62] C. Stephan, L. Ferrant, B. Berthier, S. David, L. Tassan-Got, C.O. Bacri, F. Rejmund, C. Moreau and the n_TOF Collaboration; Neutron induced fission cross section measurements; contribution to the ND2001conference, Tsukuba, Japan;

[63] R.L. Macklin et al, NIM A Vol. 96 (1971) 509-513.

Aknowledgments

I wish to thank a long list of people, which, in these three years, have helped me or worked with me in the research activity illustrated in this thesis.

My first thinking is addressed to the two tutors of my Ph.D. course in Bari University: Prof. R. DeLeo and Dr. N. Colonna. They have constantly encouraged my work, suggested my steps and corrected my faults. Without them, my comprehension of the physics processes and experimental techniques should be poor and confuse.

The second thinking is to three mentors that I knew in the laboratory visited in those years: Prof. F. Käppeler at FZK in Karlsruhe (Germany), Dr. R.C: Haight at LANL in Los Alamos (USA) and Dr. P. Cennini at CERN in Geneve (Switzerland). They have followed and supported my activity in their laboratory where I performed an important part of my research and continue patiently to correct my errors.

Particular thanks are directed to Dr. G. Tagliente and to Dr. A. Mengoni. Dr. Tagliente, in fact, has improved my knowledge in the hardware systems and in the software codes while Dr. Mengoni has clarified fundamental aspects of Nuclear Physics and the possibilities of application to the nuclear technologies.

A thank is to the Coordinator of PhD. Course Prof. M.T. Muciaccia and to two co-relators of this work: Prof. G. Maggi and Prof. G. Bellia for their useful suggestions and for the constant support to my initiatives.

Finally I wish to thank all people that in those years have the patience to work with me and to hear my foolishnesses: Carlos, Cesar, Christos, Cristophe, Daniel, Dimitri, Eric, Frank, Gaelle, Laure, Laurent, Livio, Luc, Julien, Michael, Paolo, Pierfrancesco, Ralf, Renè, Roberto, Shawn, Thomas e Vladimir.